Models of Complex Adaptive Systems with Underlying Network Structure

Sehyo Charley Choe
Wadham College
University of Oxford

A thesis submitted for the degree of
Doctor of Philosophy

Hilary 2007

To my parents, to whom I owe everything

Acknowledgements

First and foremost I would like to thank Neil Johnson for his guidance, support and inspiration. Without him this work would not have been possible.

My grateful thanks to my collaborators Pak–Ming Hui, Mark Rondeau, Alexandra Olaya-Castro, Chiu Fan Lee, Tomas Alarcón, Kagan Tumer, Kurt Mittman, and Sean Gourley, for the fruitful and always invaluable discussions and insights.

I must thank all my friends. In particular I thank Franz Josef Saar, Stuart Sanders, Tim Jarrett, David Smith and Alexandra Olaya-Castro for their friendship. They made this time that much more enjoyable.

Most importantly, I wish to express my most heartfelt gratitude to my parents and my sisters, Youngmin and Jeanie, for always being there for me. Without my family's love and support I would have undoubtedly lacked the strength, courage and character to see this time of my life through to the end.

Models of Complex Adaptive Systems with Underlying Network Structure

Sehyo Charley Choe, Wadham College

Thesis submitted for the degree of *Doctor of Philosophy*, Hilary Term 2007

Abstract

This thesis explores the effect of different types of underlying network structure on the dynamical behaviour of a competitive population – a situation encountered in many real–world complex systems. In the first part of the thesis, I focus on generic, but abstract, multi–agent systems. I start by presenting analytic and numerical results for a population of heterogeneous, decision–making agents competing for some limited global resource, in which connections arise unintentionally between agents as a by–product of their strategy choices. I show that accounting for the resulting groups of strongly–correlated agents – in particular, the crowds and so-called 'anticrowds' – yields an accurate analytic description of the systems dynamics. I then introduce a local communication network between the agents, enabling them to intentionally share information among themselves. Such an interaction network leads to highly non–trivial dynamics, forcing a trade-off between individual and global success. Introducing corruption into the information being exchanged between agents, gives rise to a novel phase transition. I then provide a quantitative analytic theory of these various numerical results by generalizing the *Crowd-Anticrowd* formalism to include such local interactions.

In the second part of the thesis, I consider a real-world system which also features competitive populations and networks - a cancer tumour, which contains cancerous cells competing for space and nutrients in the presence of an underlying vasculature structure. To simplify the analysis and comparison to real clinical data, the model chosen is far simpler than that discussed in the first part of the thesis – however despite its simplicity, the model is shown to yield remarkably good agreement with empirical findings. In addition, the model shows how different treatment methods can lead to a wide variety of unexpected re-growth behaviours of the tumour.

Contents

List of Figures v

1 Introduction **1**

List of Publications 10

Bibliography 12

I B–A–R (Binary Agent Resource) System **17**

2 Toward a Theory of Collective Dynamics in Multi–Agent Complex Systems **18**

2.1 Introduction 18

2.2 B–A–R (Binary Agent Resource) systems 20

2.3 Crowd–Anticrowd formalism 23

2.4 Implementation of Crowd–Anticrowd formalism 30

2.5 Application of Crowd–Anticrowd formalism to a generalized B–A–R system 32

2.5.1 Numerical results of multiple–memory population 34

2.5.2 Crowd–Anticrowd formalism of multiple–memory population . 41

2.6 Summary and Discussions 45

Bibliography 48

3 Effects of Local Connectivity in Multi–Agent Complex Systems **50**

3.1 Introduction 50

3.2 B–A–R system with a physical network (i.e. B–A–R–N) 51

3.3 Numerical Results for B–A–R–N 51

3.4 Crowd–Anticrowd formalism incorporating a physical network 53

3.5 Summary 59
Bibliography 60

4 Error–driven Global Transition in a Network–based Multi–Agent Complex System **62**
4.1 Introduction 62
4.2 B–A–R–N model with erroneous information 63
4.3 Crowd–Anticrowd formalism of B–A–R–N with erroneous information 67
4.4 Comparison to numerical results 69
4.4.1 Corrections to theory 70
4.5 Summary 72
Bibliography 73

II Cancer:
A Real–World Network–Based Complex System **75**

5 A Brief Overview of Existing Avascular Cancer Models **76**
5.1 Introduction 76
5.2 Cancer properties 77
5.3 Avascular tumour models 80
5.4 Continuum models 82
5.5 Discrete models 84
5.5.1 Cellular automaton models 85
5.5.1.1 Early models 85
5.5.1.2 Recent models 87
5.5.2 Agent–based model 89
5.5.3 Hybrid models 89
5.6 Summary 92
Bibliography 95

6 A Tumour Model Based on an Evolving Competitive Population Coupled to an Underlying Network **104**
6.1 Introduction 104

6.2 A new multi–scale model coupling the tumour and vasculature systems 106
6.3 Discussion of results from the model 111
6.4 Predicted tumour re–growth following different treatment types . . . 115
6.5 Summary 118
Bibliography 121

7 Conclusion **124**

List of Figures

2.1 Schematic representation of B–A–R (Binary Agent Resource) system 20

2.2 Strategy Space for $m = 2$ 22

2.3 Schematic representation of the strategy allocation matrix Ψ in the Reduced Strategy Space (RSS) with $m = 2$ and $S = 2$ 30

2.4 Crowd–Anticrowd formalism vs. numerical simulation results for σ in the *Minority Game* 33

2.5 W for a multiple–memory and mixed–ability population 35

2.6 W for a multiple–memory population with $s = 16$ and $s = 3$ 37

2.7 W for multiple–memory populations with $s = 3$ and $s = 16$ 39

2.8 σ for multiple–memory populations with $s = 16$ and $s = 8$ 41

3.1 Modest resource B–A–R–N results. 52

3.2 Crowd–Anticrowd vs. numerical B–A–R–N results 54

3.3 High resource B–A–R–N results 56

3.4 High resource B–A–R–N results for varying m 58

4.1 σ_D as a function of q and p in the corrupted B–A–R–N model 64

4.2 σ_D for individual runs zoomed in around $q = 0.5$ 65

4.3 Contour map of Fig. 4.1 66

5.1 Layers of a tumour spheroid 79

6.1 Schematic diagram of the cancer model system. 107

6.2 Schematic diagram of model's temporal update within each timestep. 108

6.3 Standard results verification for model tumour 112

6.4 Growth pattern comparison of model vs. real. 114
6.5 Single treatment results 116
6.6 Multiple treatment results 119

Chapter 1

Introduction

The underlying assumptions of traditional statistical physics such as macroscopic ergodicity, self-averaging, and history independence, tend to be valid when the system in question comprises large numbers of inanimate, identical bodies which move and interact according to the known laws of physics, such as Newton's Laws of Motion. However, many real–world systems of current interest do not satisfy such assumptions, either macroscopically or microscopically. As a result, their dynamical behaviour is typically very rich and requires a more generalized theoretical analysis than that currently available in statistical physics [1]. Such 'Complex Systems' are therefore of great interest to the new generation of condensed matter theorists in the physics community.

The term 'Complex Systems' and 'Complexity' has been adopted in subtlety different ways by different academic communities. For example, computer scientists tend to take a formal, algorithmic approach to the definition of these words. In this thesis, I will take the more practical approach which has been adopted in the physics community [1], whereby 'complex system' refers to systems which display characteristic types of macroscopic behaviour, and have a distinctive type of microscopic composition. In particular, I will consider many–body systems consisting of interacting particles, which may have time–dependent and spatially–dependent interactions.

These particles, or 'agents', typically have some primitive ability to evolve, think and even learn, and hence require the capacities to process and store local and/or global information – this in turn implies memory, and adaptation to feedback, which in turn determines each agent's actions in time. These distinguishing features between different particles, in turn injects a high level of heterogeneity into the system.

Complex systems are generally open systems, and are hence influenced by exogenous factors in addition to their own internal dynamics. Furthermore, they are typically far from equilibrium, and hence evolve in a highly non–trivial way – which is in turn the key to unexpected, emergent behaviour. Specifically, the collective behaviour resulting from the interactions between agents who are typically competing for some limited nutrient (or resource), and are subject to local and/or global information, can lead to highly non–trivial, emergent behaviour on a macroscopic scale. Possible examples include the emergence of traffic jams from a population of autonomous cars competing for space on a road, or crashes in a stock–market containing a population of traders competing for the best trade, or a tumour in a body containing populations of cells competing for space and nutrients. The emergence is typically self–organized, since there is no overall system controller overseeing and dictating the actions of all agents. This self–organization can make the system arguably more efficient (e.g. the efficient market hypothesis) but can be also detrimental in the long run due to the possibility of extreme, and potentially catastrophic, events [2]. Hence, complex system studies not only promise an understanding of the system, but could possibly lead to better means of prediction and/or control.

The behaviour of complex systems presents a common 'hard' problem across the biological, life and social sciences [3]. To add to the level of complexity, many, if not most, complex systems are influenced by some underlying network structure [4].

Whilst early research on networks made great strives into understanding the study of static, equilibrium networks with Poissonian distributions of connections, it is only recently that the study of 'complex networks' has been a major research area within the physics community. In fact, an explosion of research within the physics literature has led to the realization that this network structure can be similar across a wide range of biological and social systems [4, 5, 6, 7, 8]. The theoretical work to date has been rather abstract, and in the explicit case of complex system networks, has focussed on the macroscopic structural properties of networks [9, 10]. Hence, a multitude of measures have been developed, distinguishing and characterizing the various different types of complex networks: random [11, 12], small–world [13] or scale–free networks [14].

Unfortunately, these studies offer little insight into the functional properties of the networks associated with real–world complex systems. In particular, for networks associated with a population of interacting objects, it is how this network structure affects the dynamical behaviour of the population, and how the population's behaviour then feeds back on this network, which is of importance. For example, from a biological perspective, knowing that a given complex system network is scale–free is not per se that interesting. Instead it is the implications of that structure on the function of the complex system itself, which is important. In short, how do the interactions between agents, and the evolution of the population's behaviour, change depending on the structure of the network? Unfortunately, the precise nature of the interplay between function and structure in complex network–based systems remains largely a mystery. These shortcomings in the current state of understanding of the functional properties of complex systems and networks provide the motivation for the research presented in this thesis.

The two key features of the systems in this thesis - and of real–world complex systems in general – are (1) a multi-agent population of semi–autonomous objects, and (2) an underlying network which is either real (i.e. through some form of physical connection) or virtual (i.e. via common strategy use or common access to some particular information). Most, if not all, real–world systems can be seen as a combination of these two elements. The research in this thesis distinguishes itself from previous works on complex systems in that it focuses on the *interplay* between a competitive population and some underlying network. In terms of the complex network literature, which has seen an explosion in the past few years, the novel feature is that the network properties are driven by the actions of the underlying competitive population. I refer to Refs. [4, 5, 6, 7, 8, 9, 10, 11, 12, 13, 14, 15, 16, 17, 18, 19] for a list of works which, while interesting, are confined to dealing with the network itself without any underlying population. In a similar way, the novel feature in terms of the multi–agent literature is the fact that the behaviour of the population is guided by the network properties, such that this network can be seen as 'feeding' the agents in some way – either with information or real nutrients. I refer to Refs. [20, 21, 22, 23, 24, 25, 26, 27, 28, 29, 30, 31, 32, 33, 34, 35] for a list of works which, while again interesting, are confined to dealing with a multi–agent population without any underlying network. Putting elements (1) and (2) together, as I do in this thesis – and then going on to obtain accurate analytic expressions to accompany many of the resulting numerical simulations – makes the results in this thesis rather unique within the complex systems research field.

This thesis is split into two parts. I begin the first part by exploring a generic, yet reasonably abstract, example of a competitive population with underlying interactions (i.e. underlying network). In particular, I look at the theoretical game proposed

by Brian Arthur [20, 21]. The so-called *El Farol bar problem* was conceived to possess many, if not most, of the features needed to mimic a real complex system, and captures many types of emergent phenomena. It is a simple generic complex system which can be adapted to describe a wide range of financial, social, medical and technological scenarios [20, 21, 22, 23, 24]. In its most simple form, the *El Farol bar problem* concerns the collective decision–making of a group of heterogeneous bar–goers who repeatedly try to predict whether they should attend a potentially overcrowded bar on a given night each week. As is the case in many complex systems, the information these bar–goers possess is limited. They have no information about the others' predictions. The only information available to each agent is global, comprising a string of outcomes ('overcrowded' or 'undercrowded') for a limited number of previous occasions. Hence, they end up having to predict the predictions of others, based on what they think is the best action given the global information. No 'typical' agent exists, since all agents are in possession of different strategies, implying that they can behave differently when faced with the same source of information. The physics literature has focused on a simplified binary form of the *El Farol bar problem* called the *Minority Game* (MG) as introduced by Challet and Zhang [24].

In chapter 2, I introduce a crowd–based theory - referred to as the *Crowd–Anticrowd* formalism - for describing the collective behaviour in complex systems comprising a multi–agent population which competes for a limited resource, as in the *El Farol bar problem.* In particular, I introduce and focus on a binary version which I refer to as *B–A–R* (Binary Agent Resource) system. The *Minority Game* is a special limiting case of the *B–A–R* system, and is obtained by setting the *B–A–R* resource level to be just less than half the number of agents. The dynamical evolution is determined by the aggregate action of the heterogeneous, adaptive agent population.

An agent's action is determined by the finite set of strategies available to him, and the same source of global information is available to all agents. Hence, agents will involuntarily form groups – or crowds – determined by their strategy set. I show that accounting for the strong correlations between agents' strategies, yields an accurate analytic description of the system's dynamics.

In chapter 3, I develop this model further by examining the effect of network connections (i.e. an interaction network) on the behaviour of this frustrated system of heterogeneous, adaptive agents. In particular, I examine how a random communication network influences the cooperative behaviour of the population. I extend the *Crowd–Anticrowd* formalism to account for the communication, and local information sharing, between agents in the B–A–R system. In so doing, I uncover a rich spectrum of non-ergodic dynamics in the resulting model results. Whether the network connections turn out to be beneficial or detrimental is found to depend quite dramatically on the global resource level.

Up to this point, the thesis assumes that any information shared between agents is always perfectly accurate. However, real–world complex systems do not operate at such levels of perfection. Furthermore, informational networks might be used by agents to spy and mislead rather than to benefit others. This raises the following question: What is the effect of networks within a competitive population, where the information transmitted is corrupted? In chapter 4, I show, both analytically and numerically, that erroneous data transmission generates a global transition within a competitive population playing the *Minority Game* [24] containing a physical network. (Recall that the *Minority Game* is a special case of the B–A–R system). This transition, which resembles a phase transition, is driven by a temporal symmetry breaking in the global outcome series. I show that the phase boundary, which is a

function of the network connectivity p and the error probability q, can be described quantitatively by the *Crowd–Anticrowd* formalism.

In the second part of the thesis, I turn to an important real–world example of a complex system – cancer. Cancer is an ideal candidate for a complex system characterized by its dynamic and adaptive network–population interplay. Cancer and normal cells form a population of non–trivial, interacting heterogeneous objects which compete for some limited global resource, such as space and nutrients. Furthermore, there is a built–in memory effect and hence path dependence – in particular, the cell population can change the nutrient supply (vasculature) in response to local micro–environmental changes, which in return then influence the nutrient supply and hence the subsequent growth of the population. In other words, there is an underlying network with a complex topology (i.e. nutrient network) which determines the behaviour of the cancer cell population growth, and in return, the growing cancer cell population induces changes to the network structure through mechanisms such as angiogenesis and vessel regression. Hence there is feedback between the population of objects (i.e. agents) and the network, and vice versa. Finally, and most importantly, there is the emergence of a macroscopic phenomenon such as the tumour itself, or angiogenesis, or metastasis. All these factors, together with increasingly accurate clinical data, make cancer an ideal complex system for study [36].

In chapter 5, I give a brief overview of recent models of tumours that exhibit no new tumour–induced vessel growth (i.e. angiogenesis). These tumours present the simplest system to model and in which to understand the principles driving tumour growth, at the same time as sharing many of the phenomena exhibited by later stage tumours. There is significant interest in cancer growth modelling from the physics as well as mathematics communities. Much progress has been made to understand the

microscopic and macroscopic behaviour of cancer [37, 38, 39, 40, 41, 42, 43, 44, 45, 46, 47, 48, 49, 50, 51, 52, 53, 54, 55, 56, 57]. Existing models can broadly be divided into two categories. First, cellular automaton (CA) based models account for the inherently discrete nature of the system. They attempt to describe the cell–cell and cell–environment interactions by defining a set of CA rules and conditions. However such CA models are arguably only suitable for early tumour growth only, since they become computationally expensive for long term behaviour. On the other hand, they have the advantage of being able to look at individual cell behaviour, emphasizing the heterogeneity of the system which is most important in the early growth phase of tumoral evolution. At the other end of the spectrum are differential–equation–based models, which treat the cell populations as continuous density functions whilst coupling them to reaction–diffusion equations in order to account for the various chemical species involved. By contrast to CA models, continuum models typically describe long term, average behaviour and discount important factors such as fluctuations. However, they can provide a good description of growth behaviour in regimes where the early–stage discrete models have reached their limits. These two types of models are not exclusive, but rather complementary to each other.

Hence with these previous models in mind, chapter 6 presents a simple discrete model of cancer growth in the presence of an underlying nutrient network. The key element of this model is that it captures the dynamic interplay between the cancer growth and the vascular adaptation. Clinical results strongly emphasize the dependence of cancer growth behaviour on the supply of, and competition for, limited nutrients [58]. In addition, the complex blood vasculature network structure responsible for delivering the nutrients is highly adaptive, responding to chemical signal imbalances in the micro–environment caused by the growing tumour [59]. I have

therefore developed, and present, a simple coarse–grained, multi–scale model which captures the complex dynamic interplay between the nutrient supply network and the tumour's growth, whilst capturing the competition for space and nutrients by cancer cells without explicitly accounting for all individual cell–cell interactions. This allows for heterogeneity, yet length scales reaching beyond the avascular phase of tumour growth. The tumour model which I develop is far simpler than those discussed in Part 1 – however, I show that it can reproduce known clinical data with remarkable accuracy. Since the key to any such research is the need for a strong interaction between practitioners and modellers, the model aims to combine modelling with actual clinical (i.e. patient) images. The model is capable of being seeded with an initial vascular structure extracted from images, and is easily scaled to adapt to the image length–scale resolution. Despite the simplicity of the model, the theoretical growth curves show very good agreement with growth data gathered in nude mice. I then proceed to present results on various treatment methods in a model tumour. These results suggest that the intensity and method of intervention can lead to distinctly different re–growth behaviours of the tumour.

The thesis finishes in Chapter 7 with concluding remarks, and a brief discussion of the future directions that this research opens up.

List of Publications

Various chapters presented in this thesis have either been published, or are currently under consideration for publication. These publications are listed below:

Chapter 2

- ♢ N.F. Johnson, S.C. Choe, S. Gourley, T. Jarrett, P.M. Hui, *Advances in Solid State Physics*, **44**, pp. 427–438, Springer Verlag (2004).

- ♢ K.E. Mitman, S.C. Choe, N.F. Johnson, *Proceedings of SPIE: Noise and Fluctuations in Econophysics and Finance*, **5848**, pp. 225-232 (2005).

- ♢ N.F. Johnson, S.C. Choe, S. Gourley, T. Jarrett, P.M. Hui, *Non-Linear Dynamics and Heterogeneous Interacting Agents*, **550**, pp. 55–70, Springer Verlag Berlin Heidelberg (2005).

Chapter 3

- ♢ S. Gourley, S.C. Choe, P.M. Hui, N. F. Johnson, *Europhysics Letters*, **67** (6), pp. 867–873 (2004).

- ♢ S.C. Choe, S. Gourley, N.F. Johnson, P.M. Hui, in *The Complex Networks of Economic Interactions*, **567**, pp. 251–264, A. Namatame, T. Kaizouji, Y. Aruka (Eds.), Springer Verlag (2006).

Chapter 4

- ♢ S.C. Choe, N.F. Johnson, P.M. Hui, *Physical Review E*, **70**, 055101(R) (2004); Also selected for the November 15, 2004 issue of *Virtual Journal of Biological Physics.*

Chapter 6

♢ S.C. Choe, A. Olaya–Castro, M. Rondeau, N.F. Johnson, submitted (2007).

Bibliography

[1] Boccara, N. *Modelling Complex Systems.* Springer Verlag (2004).

[2] *Collectives and the Design of Complex Systems.* K. Tumer and D. Wolpert (editors). Springer, New York, (2004).

[3] Casti, J.L. *Would–be Worlds.* Wiley, New York, (1997).

[4] Strogatz, S. *Nature* **410**, 268 (2001).

[5] Callaway D. S., Newman M. E. J., Strogatz S. H. and Watts D. J. *Phys. Rev. Lett.* **85**, 5468 (2000).

[6] Albert, R. and Barabási A. L. *Phys. Rev. Lett.* **85**, 5234 (2000).

[7] Newman, M. E. J., Moore C. and Watts D. J. *Phys. Rev. Lett.* **84**, 3201 (2000).

[8] Albert, R. and Barabasi A. L. *Rev. Mod. Phys.* **74**, 47 (2002).

[9] Dorogovtsev, S.N. and Mendes, J.F.F. *Evolution of Networks From Biological Nets to the Internet and WWW.* Oxford University Press, Oxford, (2003).

[10] Newman, M.E.J. *SIAM Review* **45**, 167 (2003).

[11] P. Erdös and A. Rényi, *Publ. Math. Debrecen* **6**, 290 (1959).

[12] P. Erdös and A. Rényi, *Publ. Math. Inst. Hungar. Acad. Sci.* **5**, 17 (1960).

[13] Watts, D.J. and Strogatz, S.H. *Nature* **393**, 440 (1998).

[14] Albert, R., Jeong, H. and Barabási, A.L. *Nature* **406**, 378 (2000).

[15] Costa, L.d.F., Rodrigues, F.A., Travieso, G., Villas Boas, P.R. cond–mat/0505185 (2005).

[16] Boccaletti, S., Latora, V., Moreno, Y., Chavez, M., Hwang, D.-U. *Physics Reports* **424**, pp. 175–308 (2006)

[17] Evans, T.S. cond-mat/0405123 (2004).

[18] Krapivsky, P.L., Redner, S., Leyvraz, F. *Phys Rev. Lett.* **85**, 4629 (2000).

[19] Vázquez, A., Oliveira, J. G., Barabási, A.-L., *Phys. Rev. E* **71**, 025103 (2005).

[20] Arthur, B. *Amer. Econ. Rev.* **84**, 406 (1994).

[21] Arthur, B. *Science* **284**, 107 (1999).

[22] Jefferies, P., Hart, M., Johnson, N.F. and Hui, P.M. *J. Phys. A: Math. Gen.* **33**, L409 (2000).

[23] Jefferies, P., Hart, M., Johnson, N.F. *Phys. Rev. E* **65**, 016105 (2002).

[24] Challet, D. and Zhang, Y.C. *Physica A* **246**, 407 (1997).

[25] Axtell, R.L. Working paper 99–03–019, Santa Fe Institute: Santa Fe, New Mexico (1999).

[26] Bieniawski, S., Kroo, I.M., AIAA Paper 2003–1941 (2003).

[27] Bonabeau, E., Dorigo, M., Theraulaz, G. *Swarm Intelligence: From Natural to Artificial Systems* Oxford University Press, (1999).

[28] Buhl, J., Sumpter, D.J.T., Couzin, I.D., Hale, J., Despland, E., Miller, E., Simpson, S.J. *Science* **312**, pp. 1402–1406 (2006).

[29] Couzin, I.D., Franks, N.R. *Proceedings of the Royal Society of London* **270**, pp. 39–146 (2002).

[30] Couzin, I.D., James, R., Croft, D.P., Krause, J. *Social organization and information transfer in schooling fish Fish Cognition and Behaviour* (eds.) Brown C., Laland, K.N., Krause, J (2006).

[31] D'Hulst, R., Rodgers, G.J. *Eur. Phys. J. B* **20**, 619 (2001).

[32] Schweitzer, F. *Brownian Agents and Active Particles. On the Emergence of Complex Behavior in the Natural and Social Sciences.* Springer (2003).

[33] Axelrod, R. *The Complexity of Cooperation: Agent–based Models of Competition and Collaboration.* Princeton University Press, NJ (1997).

[34] Helbing, D., Treiber, M. *Science* **282**, pp. 200–201 (1998).

[35] Helbing, D., Treiber, M. *Phys. Rev. Lett.* **81**, 3042 (1998).

[36] Gatenby, R.A., Maini, P.K. *Nature* **421**, 321 (2003).

[37] Araujo, R.P., McElwain, D.L.S.*Bull. Math. Biol.*, **66**, pp. 1039–1091 (2004).

[38] Byrne, H.M., Alarcón, T., Owen, M.R., Webb, S.D., Maini, P.K. *Phil. Trans. R. Soc. A* **364**, pp. 1563–1578 (2006).

[39] Roose, T., Chapman, S.J., Maini, P.K. unpublished. (2006).

[40] McElwain, D. L. S., Morris, L. E. *Math. Biosci.* **39**, pp. 147–157 (1978).

[41] Casciari, J.J., Sotirchos, S.V., Sutherland, R.M. *Cell. Prolif.* **25**, pp. 1–22 (1992).

[42] Gatenby, R.A., Gawlinski, E.T. *Cacner Res.* **56**, pp. 5745–5753 (1996).

[43] Ward, J.P., King, J.R. *IMA J. Math. Appl. Med. Biol.* **14**, pp. 36–69 (1997)

[44] Byrne, H. M., Chaplain, M. A. J. *J. Theor. Med.* **1**, pp. 223–236 (1998).

[45] Sherratt, J.A., Chaplain, M.A.J. *J. Math. Biol.* **43**, pp. 291–312 (2001).

[46] Alarcón, T., Byrne, H.M., Maini, P.K. *J. Theor. Biol.* **225**, pp. 257–274 (2003).

[47] Alarcón, T., Byrne, H.M., Maini, P.K. *J. Theor. Biol* **229**, pp. 395–411 (2004).

[48] Alarcón, T., Byrne, H.M., Maini, P.K. *Multiscale Model Simul.* **3**, pp. 440–475 (2005).

[49] Smallbone, K., Gavaghan, D.J., Gatenby, R.A., Maini, P.K. *J.Theor.Biol.* **235**, pp. 476–484 (2005).

[50] Maini, P.K., Gatenby, R.A. in *Cancer Bioinformatics: From Therapy Design to Treatment*, S. Nagl (ed), John Wiley & Sons, Ltd, pp. 95–107 (2006).

[51] Alarcón, T., Owen, M.R., Byrne, H.M., Maini, P.K. *Computational and Mathematical Methods in Medicine* **7**, pp. 85–119 (2006).

[52] Scalerandi, M., Romano, A., Pescarmona, G.P., Delsanto, P.P, Condat, C.A. *Phys. Rev. E* **59**, pp. 2206–2217 (1999).

[53] Delsanto, P.P., Romano, A., Scalerandi, M., Pescarmona, G.P. *Phys. Rev. E* **62**, pp. 2547–2554 (2000).

[54] Kansal, A.R., Torquato, S., Harsh IV, G.R., Chiocca, E.A., Deisboeck, T.S. *J. Theor. Biol.* **203**, pp. 367–382 (2000).

[55] Anderson, A.R.A, Chaplain, M.A.J. *Bull. Math. Biol.* **60**, pp. 857–899 (1998).

[56] Mansury, Y., Deisboeck T.S. *Physica A* **331**, pp. 219–232 (2004).

[57] Patel, A.A., Gawlinsky, E.T., Lemieux, S.K., Gatenby, R.A. *J. Theor. Biol.* **213**, pp. 315–331 (2001).

[58] Eskey, C.J., Koretsky, A.P., Domach, M.M., Jain, R.K. *Proc. Natl. Acad. Sci. USA* **90**, 2646 (1993).

[59] Holash, J., et al. *Science* **284**, 1994 (1999).

Part I

B–A–R (Binary Agent Resource) System

Chapter 2

Toward a Theory of Collective Dynamics in Multi–Agent Complex Systems

2.1 Introduction

Complex Systems, together with their dynamical behaviour, are thought to pervade much of the natural, informational, sociological, and economic world [1, 2]. Complex systems are probably best defined in terms of a list of common features which distinguish them from 'simple' systems, and from systems which are just 'complicated' as opposed to being complex. A list of complex system 'stylized facts' should include: feedback and adaptation at the macroscopic and/or microscopic level, many (but not too many) interacting parts, non–stationarity, evolution, coupling with the environment, and observed dynamics which depend upon the particular realization of the system.

Casti has argued that [1] ".... a decent mathematical formalism to describe and analyze the [so-called] *El Farol bar problem* (EFBP) would go a long way toward the creation of a viable theory of complex, adaptive systems". The rationale behind this statement is that the *El Farol bar problem*, which was originally proposed by Brian Arthur [3] to demonstrate the essence of Complexity in financial markets in-

volving many interacting agents, incorporates the key features of a complex system in an everyday setting. Very briefly, the *El Farol bar problem* concerns the collective decision–making of a group of potential bar–goers (i.e. agents) who repeatedly try to predict whether they should attend a potentially overcrowded bar on a given night each week. They have no information about the others' predictions. Indeed the only information available to each agent is global, comprising a string of outcomes ('overcrowded' or 'undercrowded') for a limited number of previous occasions. Hence, they end up having to predict the predictions of others. No 'typical' agent exists, since all such typical agents would then make the same decision, hence rendering their common prediction scheme useless. With the exception of Ref. [4], the physics literature has focused on a simplified binary form of the *El Farol bar problem* called the *Minority Game* (MG) as introduced by Challet and Zhang [5, 6].

In this chapter, we present a theoretical framework for describing a class of complex systems comprising competitive multi-agent populations, which we refer to as B-A-R (Binary Agent Resource) systems. The success of the resulting theory lies in correctly accounting for the strong correlations in agents' actions, which are brought about by groups of agents momentarily using the same strategies. In particular, the population behaves like clusters of agents having a strong positive correlation within a given cluster (i.e. within a crowd) and a strong negative correlation between clusters (i.e. between a crowd and an anticrowd). We therefore refer to the theory as the *Crowd-Anticrowd* formalism. In this chapter, we focus on MG-like games in order to demonstrate the accuracy of the approach. However, we emphasize that the *B–A–R* system is a more general framework than the *Minority Game*, and hence the *Crowd–Anticrowd* formalism presented in this chapter is not limited to MG–like games only. Since the theory only makes fairly modest assumptions about a specific games dy-

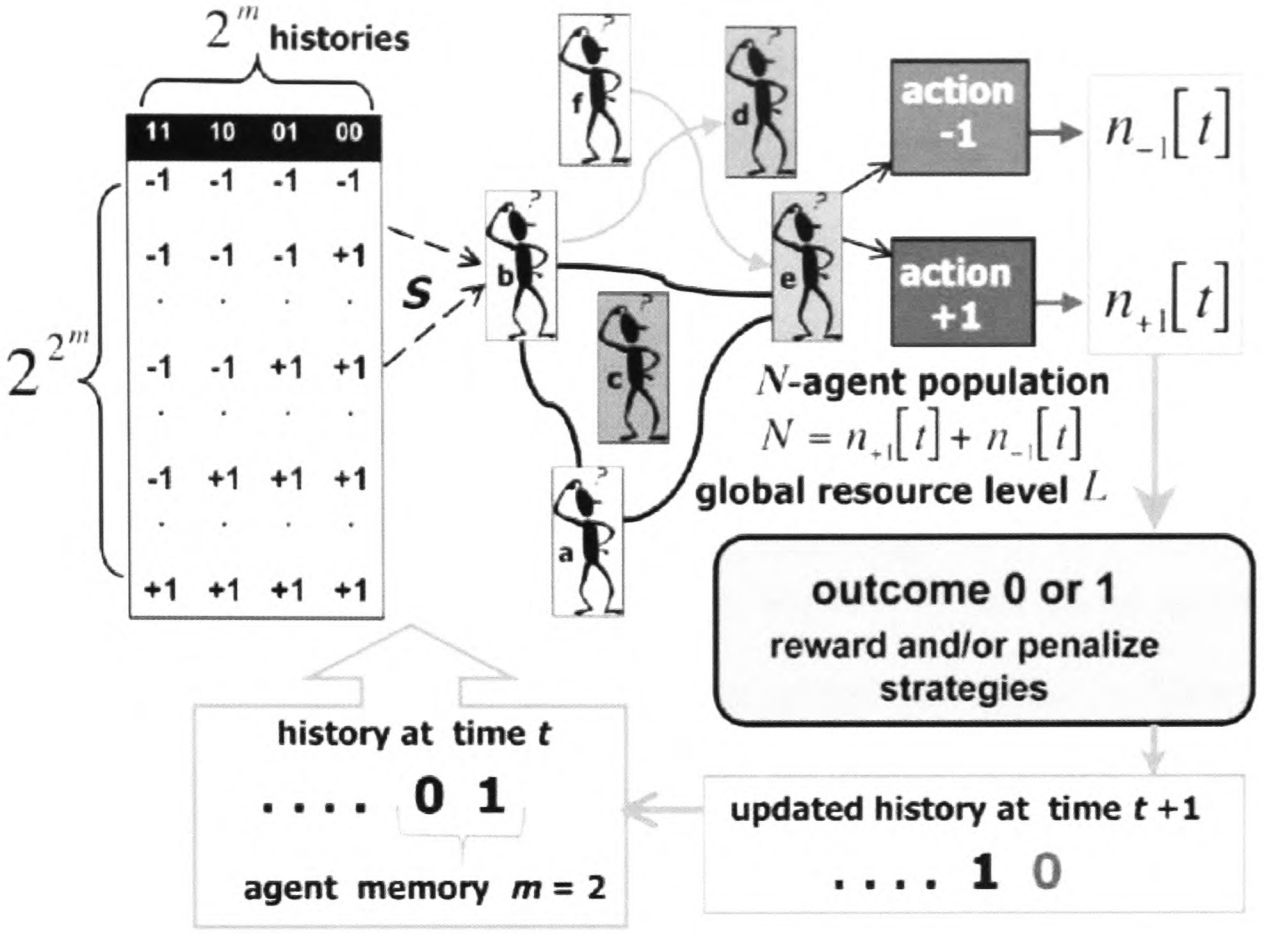

Figure 2.1: Schematic representation of B–A–R (Binary Agent Resource) system. At timestep t, each agent decides between action -1 and action $+1$ based on the predictions of the S strategies that he possesses. A total of $n_{-1}[t]$ agents choose -1, and $n_{+1}[t]$ choose $+1$. Agents may be subject to some underlying network structure which may be static or evolving, and ordered or disordered (see Refs. [7, 8]). The agents' actions are aggregated, and a global outcome 0 or 1 is assigned. Strategies are rewarded/penalized one virtual point according to whether their predicted action would have been a winning/losing action.

namical behaviour, it could be used to describe the dynamics in a wide variety of systems comprising competitive populations [7].

2.2 B–A–R (Binary Agent Resource) systems

Figure 2.1 summarizes the generic form of the B–A–R (Binary Agent Resource) system under consideration. At timestep t, each agent (e.g. a bar customer, a commuter, or a market agent) decides between action -1 (e.g. go home, take route B, or sell) and action $+1$ (e.g. attend the bar, take route A, or buy) based on the predictions of the

S strategies that he possesses. A total of $n_{-1}[t]$ agents choose -1, and $n_{+1}[t]$ choose $+1$. Agents may be subject to some underlying network structure which may be static or evolving, and ordered or disordered (see Refs. [7, 8]). The agents' actions are aggregated, and a global outcome 0 or 1 is assigned. Strategies are rewarded/penalized one virtual point according to whether their predicted action would have been a winning/losing action. The global information available to the agents is a common memory of the most recent m outcomes, which are represented as either 0 (e.g. bar attendance below seating capacity L) or 1 (e.g. bar attendance above seating capacity L). Note, by setting resource $L = \frac{N-1}{2}$ we retrive the *Minority Game*. Hence, this outcome history is represented by a binary bit–string of length m. For general m, there will be $P = 2^m$ possible history bit–strings. These history bit–strings can alternatively be represented in decimal form: $\mu = \{0, 1, ..., P-1\}$. For $m = 2$, for example, $\mu = 0$ corresponds to 00, $\mu = 1$ corresponds to 01 etc. A strategy consists of a predicted action, -1 or $+1$, for each possible history bit–string. Hence, there are $2^{P=2^m}$ possible strategies.

Figure 2.2 shows the $m = 2$ strategy space from Fig. 2.1. A strategy is a set of instructions to describe what action an agent should take, given any particular history μ. The strategy space is the set of strategies from which agents are allocated their strategies. The strategy space shown is known as the Full Strategy Space (FSS) and contains all possible permutations of the actions -1 and $+1$ for each history. As such there are 2^{2^m} strategies in this space. One can choose a subset of $2 \cdot 2^m$ strategies, called a Reduced Strategy Space (RSS), such that any pair within this subset has one of the following two characteristics: (i) *Anti–correlated.* For example, any two agents using the $(m = 2)$ strategies $(-1, -1, +1, +1)$ and $(+1, +1, -1, -1)$ respectively, would take the opposite action irrespective of the sequence of previous

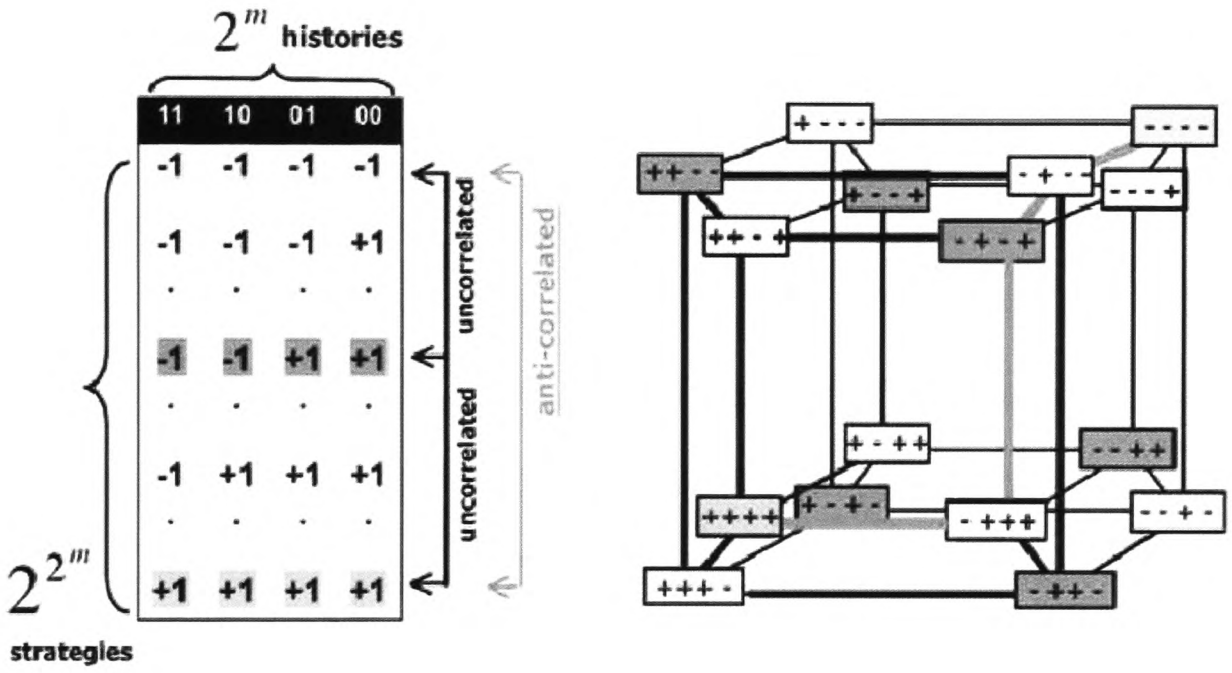

Figure 2.2: Strategy Space for $m = 2$, together with some example strategies (left). The strategy space shown is known as the Full Strategy Space (FSS) and contains all possible permutations of the actions -1 and $+1$ for each history. There are 2^{2^m} strategies in the FSS. The 2^m dimensional hypercube (right) shows all 2^{2^m} strategies in the FSS at its vertices. The shaded strategies form a Reduced Strategy Space RSS. There are $2 \cdot 2^m = 2P$ strategies in the RSS. The grey shaded line connects two strategies with a Hamming distance separation of 4.

outcomes and hence the history. Their net effect on the excess demand, $D[t]$, defined as $D[t] = n_{+1}[t] - n_{-1}[t]$ (which is an important quantity in a socio–economic setting such as a financial market), therefore cancels out at each timestep, regardless of the history. Hence, they will not contribute to fluctuations in $D[t]$. (ii) *Uncorrelated.* For example, any two agents using the strategies $(-1,-1,-1,-1)$ and $(-1,-1,+1,+1)$ respectively, would take the opposite action for two of the four histories, and the same action for the remaining two histories. If the histories occur equally often, the actions of the two agents will be uncorrelated on average. Note that the strategies in the RSS can be labelled by $R = \{1, 2, ..., 2P = 2 \cdot 2^m\}$.

The strategy allocation among agents can be described in terms of a tensor Ω describing the distribution of strategies among the N individual agents. This strategy allocation is typically fixed from the beginning of the game, hence acting as a quenched disorder in the system. The rank of the tensor Ω is given by the number of strategies S that each agent holds. We note that a single Ω 'macrostate' corresponds to many possible 'microstates' describing the specific partitions of strategies among the agents. Hence, the present *Crowd–Anticrowd* theory retained at the level of a given Ω, describes the set of all games which belong to that same Ω macrostate. We also note that although Ω is not symmetric, it can be made so since the agents do not distinguish between the order in which the two strategies are picked. Given this, we will henceforth focus on $S = 2$ and consider the symmetrised version of the strategy allocation matrix given by $\Psi = \frac{1}{2}(\Omega + \Omega^T)$.

2.3 Crowd–Anticrowd formalism

Consider an arbitrary timestep t during a run of the game. We will focus on evaluating the 'excess demand' $D[t] \equiv D\left[\underline{S}\,[t]\,, \mu\,[t]\right] = n_{+1}[t] - n_{-1}[t]$, although any other

function of $n_{+1}[t]$ and $n_{-1}[t]$ can be evaluated in a similar way. Here, $\underline{S}[t]$ is the $2P$–dimensional score–vector whose R'th component is the virtual point score for strategy R. As previously mentioned, strategies gain/lose one virtual point at each timestep, according to whether their predicted action would have been a winning/losing action. The current history is $\mu[t]$. The standard deviation of $D[t]$ for this given run, corresponds to a time–average for a given realization of Ψ and a given set of initial conditions. Summing over the RSS, we have: $D\Big[\underline{S}[t], \mu\,[t]\Big] = \sum_{R=1}^{2P} a_R^{\mu[t]} n_R^{\underline{S}[t]}$. The quantity $a_R^{\mu[t]} = \pm 1$ is the action predicted by strategy R in response to the history bit–string μ at time t. The quantity $n_R^{\underline{S}[t]}$ is the number of agents using strategy R at time t. We use the notation $\langle X[t] \rangle_t$ to denote a time–average over the variable $X[t]$ for a given Ψ. Hence,

$$\Big\langle D\Big[\underline{S}[t], \mu\,[t]\Big]\Big\rangle_t = \sum_{R=1}^{2P} \Big\langle a_R^{\mu[t]} n_R^{\underline{S}[t]} \Big\rangle_t = \sum_{R=1}^{2P} \Big\langle a_R^{\mu[t]} \Big\rangle_t \Big\langle n_R^{\underline{S}[t]} \Big\rangle_t$$

where we have used the property that $a_R^{\mu[t]}$ and $n_R^{\underline{S}[t]}$ are uncorrelated. We now consider the special case in which all histories are visited equally on average: even if this situation does not hold for a specific Ψ, it may indeed hold once the averaging over Ψ has also been taken. For example, in the *Minority Game* (i.e., when $L = \frac{(N-1)}{2}$) all histories are visited equally at small m and a given Ψ. If we take the additional average over all Ψ, then the same is also true for large m. Under the property of equal histories:

$$\begin{aligned} \Big\langle D\Big[\underline{S}[t], \mu\,[t]\Big]\Big\rangle_t &= \sum_{R=1}^{2P} \left(\frac{1}{P} \sum_{\mu=0}^{P-1} a_R^{\mu[t]} \right) \Big\langle n_R^{\underline{S}[t]} \Big\rangle_t \\ &= \sum_{R=1}^{P} \left(\frac{1}{P} \sum_{\mu=0}^{P-1} a_R^{\mu[t]} + a_{\overline{R}}^{\mu[t]} \right) \Big\langle n_R^{\underline{S}[t]} \Big\rangle_t = \sum_{R=1}^{P} 0 \cdot \Big\langle n_R^{\underline{S}[t]} \Big\rangle_t \\ &= 0 \end{aligned} \tag{2.1}$$

where we have used the exact result that $a_R^{\mu[t]} = -a_{\overline{R}}^{\mu[t]}$ for all $\mu[t]$, and the approximation $\left\langle n_R^{\underline{S}[t]} \right\rangle_t = \left\langle n_{\overline{R}}^{\underline{S}[t]} \right\rangle_t$. This approximation is reasonable for a competitive game since there is typically no a priori best strategy: if the strategies are distributed fairly evenly among the agents, this then implies that the average number playing each strategy is approximately equal and hence $\left\langle n_R^{\underline{S}[t]} \right\rangle_t = \left\langle n_{\overline{R}}^{\underline{S}[t]} \right\rangle_t$. In the event that all histories are not equally visited over time, even after averaging over all Ψ, it may still happen that the system's dynamics is restricted to equal visits to some *subset* of histories. In this case one can then carry out the averaging in Eqn. (2.1) over this subspace of histories. More generally, the averagings in this formalism can be carried out with appropriate frequency weightings for each history. In fact, any non–ergodic dynamics can be incorporated if one knows the appropriate history path [8].

The variance of the excess demand $D[t]$ is given by

$$\sigma_\Psi^2 = \left\langle D\Big[\underline{S}[t], \mu\,[t]\Big]^2 \right\rangle_t - \left\langle D\Big[\underline{S}[t], \mu\,[t]\Big] \right\rangle_t^2 . \tag{2.2}$$

For simplicity, we will here assume the game output is unbiased and hence $\left\langle D\Big[\underline{S}[t], \mu\,[t]\,\Big] \right\rangle_t = 0$. Therefore,

$$\sigma_\Psi^2 = \left\langle D\Big[\underline{S}[t], \mu\,[t]\Big]^2 \right\rangle_t = \sum_{R,R'=1}^{2P} \left\langle a_R^{\mu[t]} n_R^{\underline{S}[t]} a_{R'}^{\mu[t]} n_{R'}^{\underline{S}[t]} \right\rangle_t .$$

Using the identities $\underline{a_R}.\underline{a_{R'}} = P$ (fully correlated), $\underline{a_R}.\underline{a_{R'}} = -P$ (fully anti-correlated), and $\underline{a_R}.\underline{a_{R'}} = 0$ (fully uncorrelated) where $\underline{a_R}$ is a vector of dimension P with components $a_R^{\mu[t]}$ for $\mu[t] = 1, 2, ..., P$, we obtain

$$\begin{aligned} \sigma_\Psi^2 &= \sum_{R=1}^{2P} \left\langle \left(n_R^{\underline{S}[t]}\right)^2 - n_R^{\underline{S}[t]} n_{\overline{R}}^{\underline{S}[t]} \right\rangle_t + \sum_{R \neq R' \neq \overline{R}}^{2P} \left\langle a_R^{\mu[t]} a_{R'}^{\mu[t]} \right\rangle_t \left\langle n_R^{\underline{S}[t]} n_{R'}^{\underline{S}[t]} \right\rangle_t \\ &= \sum_{R=1}^{2P} \left\langle \left(n_R^{\underline{S}[t]}\right)^2 - n_R^{\underline{S}[t]} n_{\overline{R}}^{\underline{S}[t]} \right\rangle_t . \end{aligned} \tag{2.3}$$

The sum over $2P$ terms can be written equivalently as a sum over P terms,

$$\begin{aligned}\sigma_{\Psi}^2 &= \sum_{R=1}^{P}\left\langle \left(n_R^{\underline{S}[t]}\right)^2 - n_R^{\underline{S}[t]} n_{\overline{R}}^{\underline{S}[t]} + \left(n_{\overline{R}}^{\underline{S}[t]}\right)^2 - n_{\overline{R}}^{\underline{S}[t]} n_R^{\underline{S}[t]} \right\rangle_t \\ &= \sum_{R=1}^{P}\left\langle \left(n_R^{\underline{S}[t]} - n_{\overline{R}}^{\underline{S}[t]}\right)^2 \right\rangle_t \equiv \left\langle \sum_{R=1}^{P}\left(n_R^{\underline{S}[t]} - n_{\overline{R}}^{\underline{S}[t]}\right)^2 \right\rangle_t .\end{aligned}$$

The values of $n_R^{\underline{S}[t]}$ and $n_{\overline{R}}^{\underline{S}[t]}$ for each R will depend on the precise form of Ψ. The ensemble–average over all possible realizations of the strategy allocation matrix Ψ is denoted by $\langle ... \rangle_{\Psi}$. Using the notation $\langle \sigma_{\Psi}^2 \rangle_{\Psi} = \sigma^2$, yields

$$\sigma^2 = \left\langle \left\langle \sum_{R=1}^{P}\left(n_R^{\underline{S}[t]} - n_{\overline{R}}^{\underline{S}[t]}\right)^2 \right\rangle_t \right\rangle_{\Psi} . \tag{2.4}$$

It is straightforward to obtain analogous expressions for the variances in $n_{+1}[t]$ and $n_{-1}[t]$. Equation (2.4) provides us with an expression for the time–averaged fluctuations. Some form of approximation must be introduced in order to reduce Eqn. (2.4) to explicit analytic expressions. It turns out that Eqn. (2.4) can be manipulated in a variety of ways, depending on the level of approximation that one is prepared to make. The precise form of any resulting analytic expression will depend on the details of the approximations made. Adopting one such approach which is well–suited to the low m regime, we start by relabelling the strategies. Specifically, the sum in Eqn. (2.4) is rewritten to be over a *virtual–point ranking* K as opposed to R. Consider the variation in points for a given strategy, as a function of time for a given realization of Ψ. The ranking (i.e. label) of a given strategy in terms of virtual–points score will typically change in time since the individual strategies have a variation in virtual–points which also varies in time. For the *Minority Game*, this variation is quite rapid in the low m regime of interest, since there are many more agents than available strategies – hence, any strategy emerging as the instantaneously

highest–scoring, will immediately get played by many agents and therefore be likely to lose on the next time–step. More general games involving competition within a multi–agent population, will typically generate a similar ecology of strategy–scores with no all–time winner. This implies that the specific identity of the 'K'th highest-scoring strategy' changes frequently in time. It also implies that $n_R^{S[t]}$ varies considerably in time. Therefore, in order to proceed, we shift the focus onto the time–evolution of the highest–scoring strategy, second highest–scoring strategy etc. This should have a much smoother time–evolution than the time–evolution for a given strategy. In the case that the strategies all start off with zero points, the anticorrelated strategies appear as the mirror–image, i.e. $S_K[t] = -S_{\overline{K}}[t]$. The label K is used to denote the rank in terms of strategy score, i.e. $K = 1$ is the highest scoring strategy position, $K = 2$ is the second highest–scoring strategy position etc. with

$$S_{K=1} > S_{K=2} > S_{K=3} > S_{K=4} > ... \tag{2.5}$$

assuming no strategy ties. Given that $S_R = -S_{\overline{R}}$ (i.e. all strategy scores start off at zero), then we know that $S_K = -S_{\overline{K}}$. Equation (2.4) can hence be rewritten exactly as

$$\sigma^2 = \left\langle \left\langle \sum_{K=1}^{P} \left(n_K^{S[t]} - n_{\overline{K}}^{S[t]} \right)^2 \right\rangle_t \right\rangle_\Psi . \tag{2.6}$$

Since in the systems of interest the agents are typically playing their highest–scoring strategies, then the relevant quantity in determining how many agents will instantaneously play a given strategy, is a knowledge of its relative ranking – not the actual value of its virtual points score. This suggests that the quantities $n_K^{S[t]}$ and $n_{\overline{K}}^{S[t]}$ will fluctuate relatively little in time, and that we should now develop the problem in terms of time–averaged values. We can rewrite the number of agents playing the

strategy in position K at any timestep t, in terms of some constant value n_K plus a fluctuating term $n_K^{S[t]} = n_K + \varepsilon_K[t]$. We assume that one can choose a suitable constant n_K such that the fluctuation $\varepsilon_K[t]$ represents a small noise term. Hence,

$$\begin{aligned} \sigma^2 &= \left\langle \sum_{K=1}^{P} \left\langle [n_K + \varepsilon_K[t] - n_{\overline{K}} - \varepsilon_{\overline{K}}[t]]^2 \right\rangle_t \right\rangle_\Psi \\ &\approx \left\langle \sum_{K=1}^{P} \left\langle [n_K - n_{\overline{K}}]^2 \right\rangle_t \right\rangle_\Psi = \left\langle \sum_{K=1}^{P} [n_K - n_{\overline{K}}]^2 \right\rangle_\Psi , \end{aligned} \tag{2.7}$$

assuming the noise terms have averaged out to be small. The averaging over Ψ can now be taken inside the sum. Each term can then be rewritten exactly using the joint probability distribution for n_K and $n_{\overline{K}}$, which we shall call $P(n_K, n_{\overline{K}})$. Hence

$$\sigma^2 = \sum_{K=1}^{P} \left\langle [n_K - n_{\overline{K}}]^2 \right\rangle_\Psi = \sum_{K=1}^{P} \sum_{n_K=0}^{N} \sum_{n_{\overline{K}}=0}^{N} [n_K - n_{\overline{K}}]^2 \, P(n_K, n_{\overline{K}}). \tag{2.8}$$

We now look at Eqn. (2.8) in the limiting case where the averaging over the quenched disorder matrix is dominated by matrices Ψ which are nearly flat. This will be a good approximation in the 'crowded' limit of small m in which there are many more agents than available strategies, since the standard deviation of an element in Ψ (i.e. the standard deviation in bin–size) is then much smaller than the mean bin–size. The probability distribution $P(n_K, n_{\overline{K}})$ will then be sharply peaked around the n_K and $n_{\overline{K}}$ values given by the mean values for a flat quenched–disorder matrix Ψ. We label these mean values as $\overline{n_K}$ and $\overline{n_{\overline{K}}}$. Hence, $P(n_K, n_{\overline{K}}) = \delta_{n_K,\overline{n_K}} \delta_{n_{\overline{K}},\overline{n_{\overline{K}}}}$ and so,

$$\sigma^2 = \sum_{K=1}^{P} [\overline{n_K} - \overline{n_{\overline{K}}}]^2 . \tag{2.9}$$

There is a very simple interpretation of Eqn. (2.9). It represents the sum of the variances for each crowd–anticrowd pair. For a given strategy K there is an anticorrelated strategy $\overline{K}$. The $\overline{n_K}$ agents using strategy K are doing the *opposite*

of the $\overline{n_{\overline{K}}}$ agents using strategy $\overline{K}$ *irrespective* of the history bit–string. Hence, the effective group–size for each crowd–anticrowd pair is $n_K^{eff} = \overline{n_K} - \overline{n_{\overline{K}}}$: this represents the net step–size d of the crowd–anticrowd pair in a random walk contribution to the total variance. Hence, the net contribution by this crowd–anticrowd pair to the variance is given by

$$[\sigma^2]_{K\overline{K}} = 4pqd^2 = 4 \cdot \frac{1}{2} \cdot \frac{1}{2}[n_K^{eff}]^2 = [\overline{n_K} - \overline{n_{\overline{K}}}]^2 \tag{2.10}$$

where $p = q = \frac{1}{2}$ for a random walk. Since all the strong correlations have been included (i.e. anti–correlations), it can therefore be assumed that the separate crowd–anticrowd pairs execute random walks which are *uncorrelated* with respect to each other. [Recall the properties of the RSS - all the remaining strategies are uncorrelated.] Hence, the total variance is given by the sum of the individual variances,

$$\sigma^2 = \sum_{K=1}^{P} [\sigma^2]_{K\overline{K}} = \sum_{K=1}^{P} [\overline{n_K} - \overline{n_{\overline{K}}}]^2 , \tag{2.11}$$

which corresponds exactly to Eqn. (2.9). If strategy–ties occur frequently, then one has to be more careful about evaluating $\overline{n_K}$ since its value may be affected by the tie–breaking rule. We will show elsewhere that this becomes quite important in the case of very small m in the presence of network connections [8] – this is because very small m naturally leads to crowding in strategy space and hence mean–reverting virtual scores for strategies. This mean–reversion is amplified further by the presence of network connections which increases the crowding, thereby increasing the chance of strategy ties.

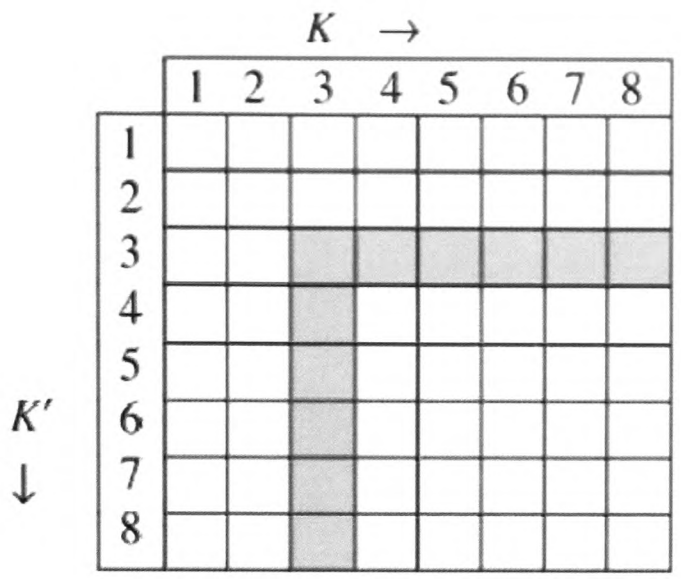

Figure 2.3: Schematic representation of the strategy allocation matrix Ψ with $m = 2$ and $S = 2$, in the RSS. The strategies are ranked according to strategy score, and are labelled by the rank K. In the limit that Ψ is essentially flat, then the number of agents playing the K'th highest-scoring strategy, is just proportional to the number of shaded bins at that K.

2.4 Implementation of Crowd–Anticrowd formalism

Here we evaluate the Crowd–Anticrowd expressions, in the important limiting case of small m. Since there are many more agents than available strategies, crowding effects will be important. Each element of Ψ has a mean of $\frac{N}{(2P)^S}$ agents per 'bin'. In the case of small m and hence densely–filled Ψ, the fluctuations in the number of agents per bin will be small compared to this mean value – hence, the matrix Ψ looks uniform or 'flat' in terms of the occupation numbers in each bin. Figure 2.3 provides a schematic representation of Ψ with $m = 2$, $S = 2$, in the RSS. If the matrix Ψ is indeed flat, then any re–ordering due to changes in the strategy ranking has no effect on the form of the matrix. Therefore, the number of agents playing the K'th highest–scoring strategy, will always be proportional to the number of shaded bins at that K (see Fig. 2.3 for $K = 3$). For general m and S, one finds

$$
\begin{aligned}
\overline{n_K} &= \frac{N}{(2P)^S}[S(2P-K)^{S-1} + \frac{S(S-1)}{2}(2P-K)^{S-2} + ... + 1] \qquad (2.12)\\
&= \frac{N}{(2P)^S}\sum_{r=0}^{S-1}\frac{S!}{(S-r)!r!}[2P-K]^r \\
&= \frac{N}{(2P)^S}([2P-K+1]^S - [2P-K]^S) \\
&= N\cdot\left(\left[1-\frac{(K-1)}{2P}\right]^S - \left[1-\frac{K}{2P}\right]^S\right),
\end{aligned}
$$

with $P \equiv 2^m$. In the case where each agent holds two strategies, $S = 2$, $\overline{n_K}$ can be simplified to

$$
\overline{n_K} = N\cdot\left(\left[1-\frac{(K-1)}{2P}\right]^2 - \left[1-\frac{K}{2P}\right]^2\right) = \frac{(2^{m+2}-2K+1)}{2^{2(m+1)}}N\ . \qquad (2.13)
$$

Hence,

$$
\begin{aligned}
\sigma^2 &= \sum_{K=1}^{P}\left[\frac{(2^{m+2}-2K+1)}{2^{2(m+1)}}N - \frac{(2K-1)}{2^{2(m+1)}}N\right]^2 \qquad (2.14)\\
&= \frac{N^2}{2^{2(2m+1)}}\sum_{K=1}^{P}[2^{m+1}-2K+1]^2 = \frac{N^2}{3\cdot 2^m}(1-2^{-2(m+1)})\ .
\end{aligned}
$$

This derivation has assumed that there are no strategy ties – more precisely, we have assumed that the game rules governing strategy ties do not upset the identical forms of the rankings in terms of highest virtual points and popularity. Hence, we have overestimated the size of the crowds using high–ranking strategies, and underestimated the size of the anticrowds using low–ranking strategies. Therefore, the analytic form for σ will overestimate the numerical value, as is indeed seen in Fig. 2.4. Notwithstanding this overestimation, there is remarkably good agreement between the numerical results and our analytic theory. In a similar way to the above calculation, the *Crowd–Anticrowd* theory can be extended to deal with the important

complementary regimes of (i) non–flat quenched disorder matrix Ψ, at small m, and (ii) non–flat quenched disorder matrix Ψ, at large m. As shown in Fig. 2.4, the agreement for these regimes is also excellent [2, 7].

The *Crowd–Anticrowd* theory has also been applied successfully to various generalizations of the *Minority Game*. For example, excellent agreement between the resulting analytic expressions and numerical simulations has been demonstrated for (i) Alloy Minority Game [9], (ii) Thermal Minority Game (TMG) [10, 11], and (iii) Thermal Alloy Minority Game [12].

2.5 Application of Crowd–Anticrowd formalism to a generalized B–A–R system

Here, we examine the effects of multiple–memory strategies in a multi–agent population. In particular, we consider the situation where the strategy set of an individual agent contains strategies with different memory–lengths m. Our results suggest that multiple–memory agents have a better chance of identifying price patterns of unknown length and hence will typically have higher winnings. In other words, agents who are capable of looking for patterns in past outcomes over several timescales, will do better on average.

We start with the B–A–R (Binary Agent Resource) system, but for similar reasons as before, again consider the special case of $L = \frac{N-1}{2}$, i.e. the *Minority Game*. However now, we consider our N–agent population to possess strategies drawn from a strategy pool which corresponds to memory lengths m_1 and m_2. Agents who possess multiple strategies of different memory lengths will therefore use different information when deciding which action to take at the next time step. Using information from different history lengths can be interpreted as somewhat analogous to the techniques of "chartists" for making forecasts in financial markets. Indeed, it is well known that

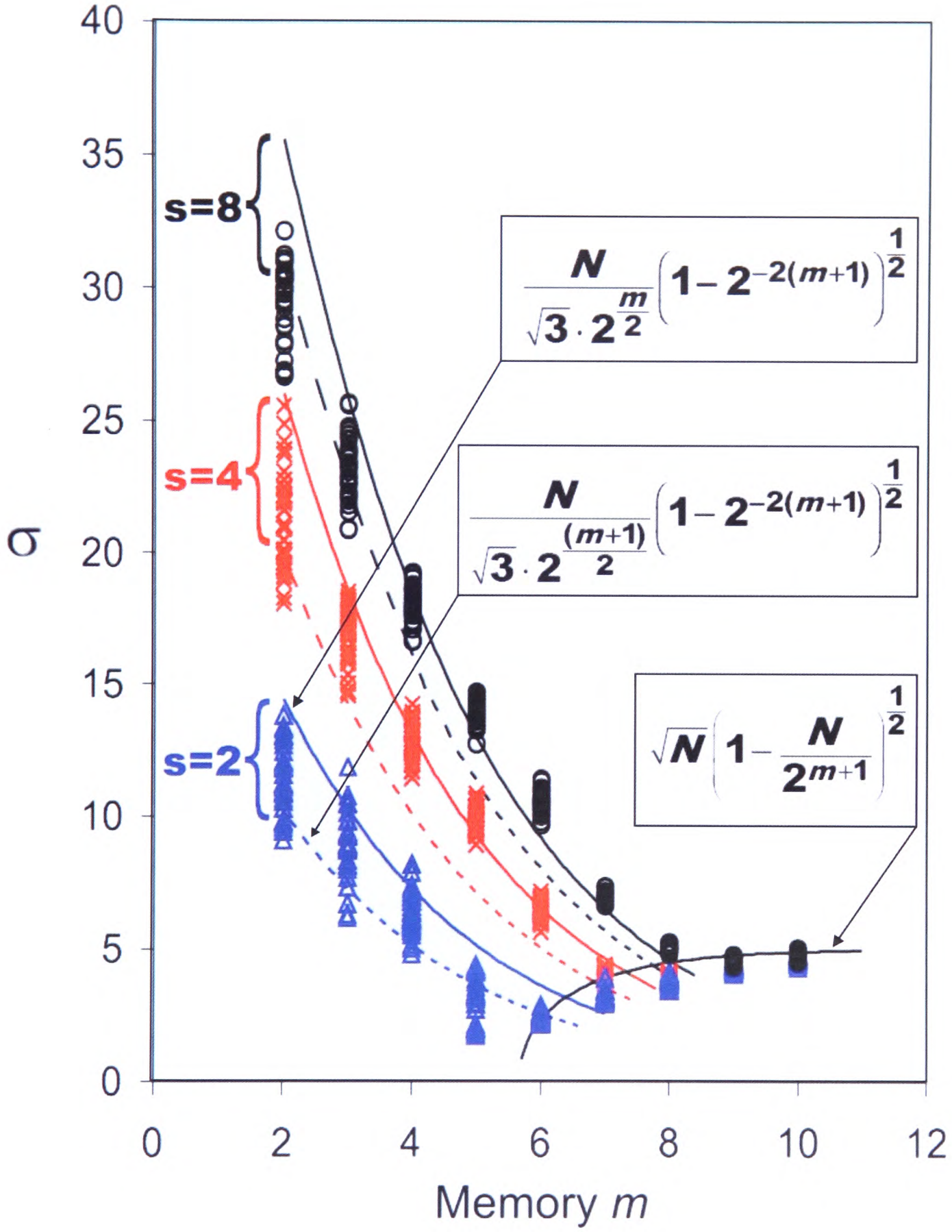

Figure 2.4: Crowd–Anticrowd formalism vs. numerical simulation results for σ in the *Minority Game* as a function of memory size m, for $N = 101$ agents, at $S = 2$, 4 and 8. At each S value, analytic forms of σ (i.e. standard deviation in excess demand $D[t]$) are shown. The numerical values were obtained from different simulation runs (triangles, crosses and circles). Figure adapted from Ref. [2].

in practice a financial trader's computer screen displays past price movements over several different timescales (e.g. hours, days, weeks). At the beginning of the game the agents are randomly assigned s strategies, of which s_1 strategies are of memory length m_1 and s_2 strategies are of memory length m_2 with repetitions allowed. The total number of strategies for each agent is the same, i.e. $s = s_1 + s_2$. We refer to this type of population as "multiple–memory" population. For comparison to previous work on mixed memory populations, we refer to a second type of population as "mixed–ability" population, in which N_{m_1} agents possess s strategies with memory length m_1, and $N_{m_2} = N - N_{m_1}$ agents possess s strategies with memory length m_2. All other rules remain as before in the B–A–R system, with $L = \frac{N-1}{2}$.

2.5.1 Numerical results of multiple–memory population

Figure 2.5 shows the average winnings per agent per turn, W, for two multiple–memory populations (circles) and a mixed–ability population (crosses). In the mixed–ability population, N_{m_1} agents hold strategies of memory–length $m_1 = 3$, while $N - N_{m_1}$ agents hold strategies of memory–length $m_2 = 6$. In the multiple–memory populations, each agent holds s_1 strategies of memory-length $m_1 = 3$ and s_2 strategies of memory–length $m_2 = 6$. All three populations correspond to $N = 101$ agents and $s = 16$ strategies per agent. The curves are plotted against x, the average proportion of agents playing an m_2 strategy on each turn. For the mixed–ability population, the average proportion of agents playing an m_2 strategy is simply $\frac{(N-N_{m_1})}{N}$. For the multiple–memory populations, we determined numerically the average number of agents playing an m_2 strategy at each turn, and divided that number by N. Each data point represents an average over 25 runs. The results for the multiple–memory population are averaged over both W and x, since in the multiple–memory population s_1 and s_2 are exogenously determined whereas x is endogenous (see Fig. 2.6). For

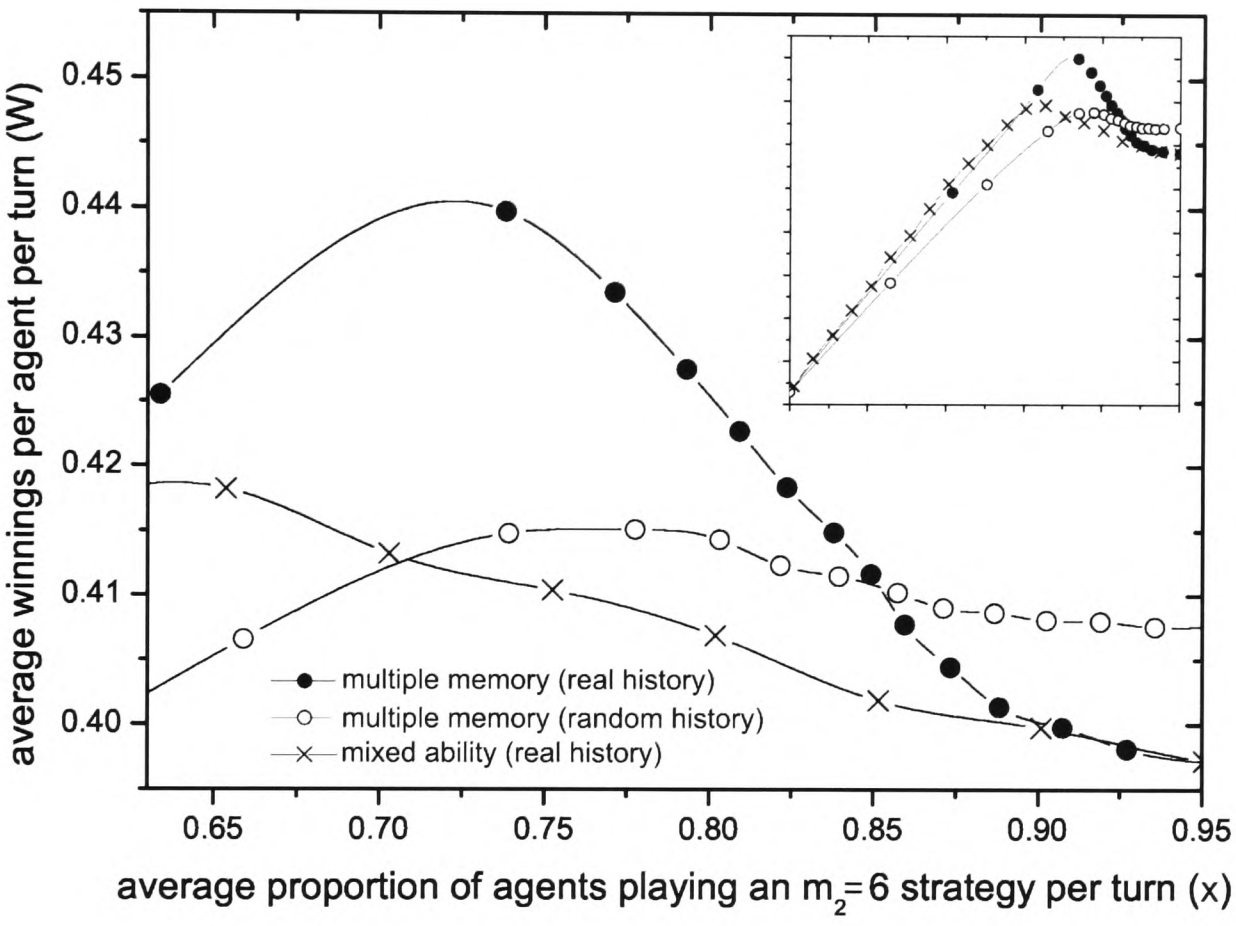

Figure 2.5: Average winnings per agent per turn, W, for multiple–memory populations and a mixed–ability population with $N = 101$, $m_1 = 3$ and $m_2 = 6$, as obtained numerically. Each agent has $s = 16$ strategies. Each data point corresponds to an average over 25 simulations. The connecting curves are a guide to the eye. The inset shows W over the full range of x, where x is the average proportion of agents playing an $m_2 = 6$ strategy per turn. See the text for an explanation of 'real history' and 'random history'.

clarity we have not shown the error bars for each data point – however the range of values in both W and x is sufficiently small that our results, discussions and conclusions are not affected by numerical artifacts. Agents are supplied with the m_1 (and/or m_2) most recent winning actions of the artificial market in the real history results (solid circles for the multiple–memory population). For the random history results (open cirles for the multiple–memory population) agents are given a random m_1 (and/or m_2) length bit–string every time step instead of the actual bit–string of winning market actions [9]. The real history multiple–memory population exhibits a maximum in W at a finite value of $x \sim 0.72$. We find that as s increases the value of x that maximizes W asymptotically approaches ~ 0.76 (we have investigated cases up to $s = 100$). The total number of points awarded per turn can therefore exceed either a pure $m_1 = 3$ or pure $m_2 = 6$ population of agents. The random history multiple–memory population also exhibits a maximum at a finite value of x. However, the magnitude of the difference between $W_{\max}$ and W when $x = 1$ (i.e. a pure m_2=6 population) is only ~ 0.007, which is within the standard deviation of the values of W. Hence, the random history multiple–memory population does not significantly outperform a pure $m_2 = 6$ population. Therefore, history has a significant affect on the ability of a multiple–memory population to outperform a pure population. In other words, a multiple–memory population can collectively profit from the real patterns which arise in past outcomes – most importantly, this added benefit of multiple–memory does *not* arise simply from a reduction in crowding in the strategy space. For all values of x, the average winnings per agent per turn of the real history multiple–memory population, is greater than or equal to the average winnings per agent per turn for the mixed–ability population. This result is not duplicated if the multiple–memory population is presented with a random history string. Multiple–

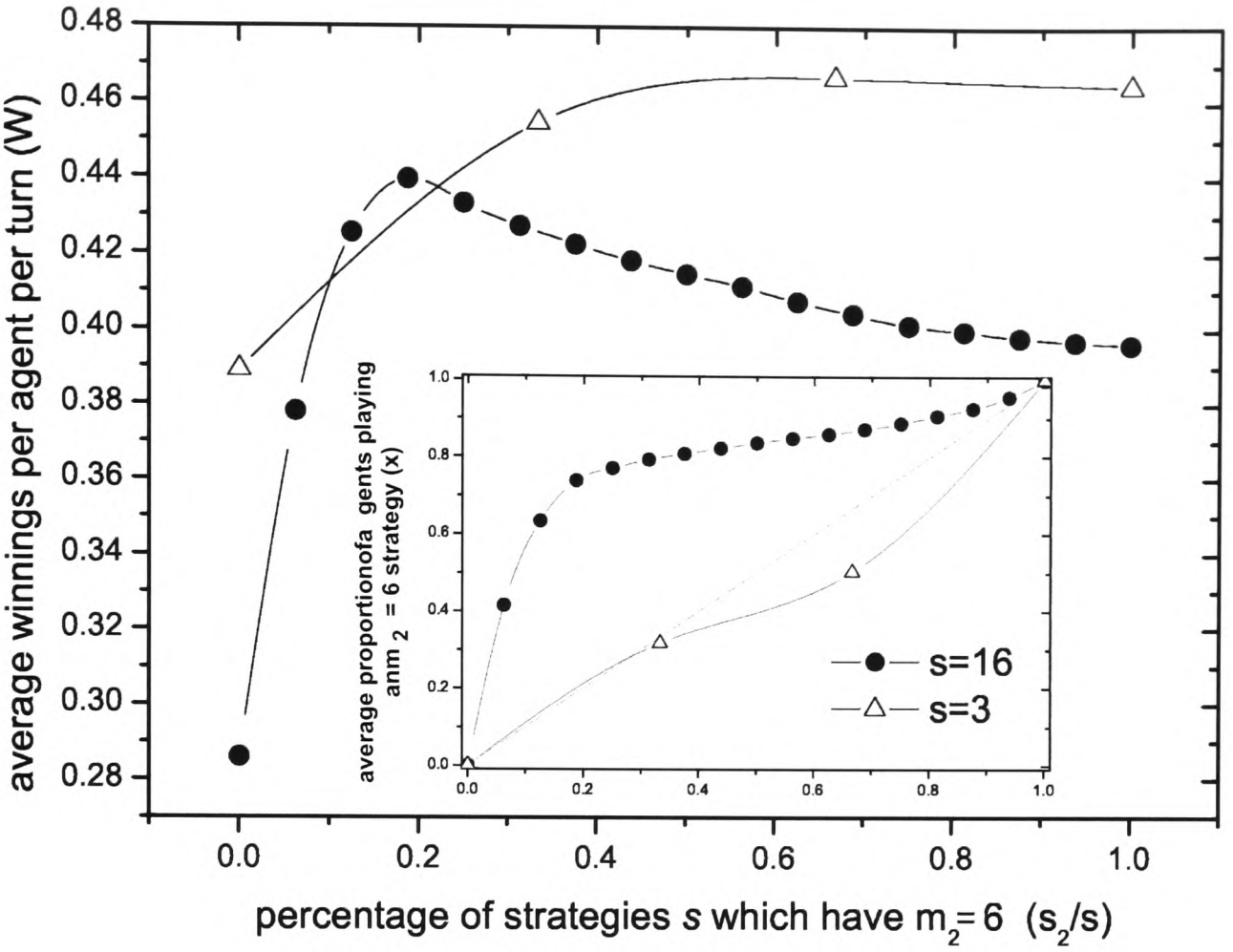

Figure 2.6: Average winnings per agent per turn, W, for multiple–memory populations with $s = 16$ and $s = 3$. $N = 101$, $m_1 = 3$ and $m_2 = 6$. The inset shows the average proportion x of agents playing an m_2 strategy for the same two populations. The dotted line in the inset represents the line $x = s_2/s$.

memory agents that are presented with the real history of winning actions from the artificial market can therefore outperform both pure populations of agents holding strategies of memory length m_1 or m_2 *and* simultaneously outperform a mixed–ability population consisting of sub–populations of agents with m_1 or m_2 strategies.

Figure 2.6 shows the average winnings per agent per turn W for two multiple–memory populations. Both populations are given the real history bit–string. One population has $s = 16$ (solid circles) as above, while the other population has $s = 3$ (triangles). All other relevant parameters are the same as in Fig. 2.5, however we now plot W against the exogenously controlled proportion of m_2 strategies (i.e. $\frac{s_2}{s}$).

Both $s = 16$ and $s = 3$ multiple–memory populations exhibit a maximum in W at finite $\frac{s_2}{s}$, again showing that the multiple–memory populations can outperform pure populations. As s increases, the value of $\frac{s_2}{s}$ which maximizes W tends towards 0. In the inset of Fig. 2.6, we plot the average proportion of agents who play an $m_2 = 6$ strategy per turn (i.e. x) versus $\frac{s_2}{s}$. The circles and triangles represent the same multiple–memory populations as described above, and the straight dashed line corresponds to $x = \frac{s_2}{s}$. Neglecting the endpoints, x for the $s = 16$ multiple–memory population always lies above the dashed line. Agents are therefore playing their m_2 strategies at a higher rate than if they were choosing a strategy at random each turn. This result is not too surprising, since we expect the m_2 strategies to outperform the m_1 strategies – after all, a pure m_2 population will have a higher W than the corresponding pure m_1 population. However, when $s = 3$ (or $s = 2$), and neglecting the endpoints, x lies below the dashed line. Therefore, in a multiple–memory population with low s, agents play m_1 strategies more frequently than the proportion of m_1 strategies that they hold. This result is remarkable since a pure $m_2 = 6$, $s = 3$ population is shown to outperform pure $m_1 = 3$, $s = 3$ populations (Fig. 2.6). The agents who play m_1 strategies more than half the time (i.e. agents with $x < 0.5$) have higher average winnings per turn than agents who play m_2 strategies more than half the time. This is illustrated in Fig. 2.7.

In Fig. 2.7(a), we plot the average winnings per turn for 2525 agents (25 runs, $N = 101$ each run) versus the proportion of turns in which an agent played an m_2 strategy. Each agent has $s = 3$ strategies, with $s_1 = 1$, $m_1 = 3$, $s_2 = 2$ and $m_2 = 6$. Agents who consistently play an m_1 or m_2 strategy have, on average, higher average winnings than agents who play a combination of m_1 and m_2 strategies. In a pure population, agents who play a combination of their strategies also tend to incur an

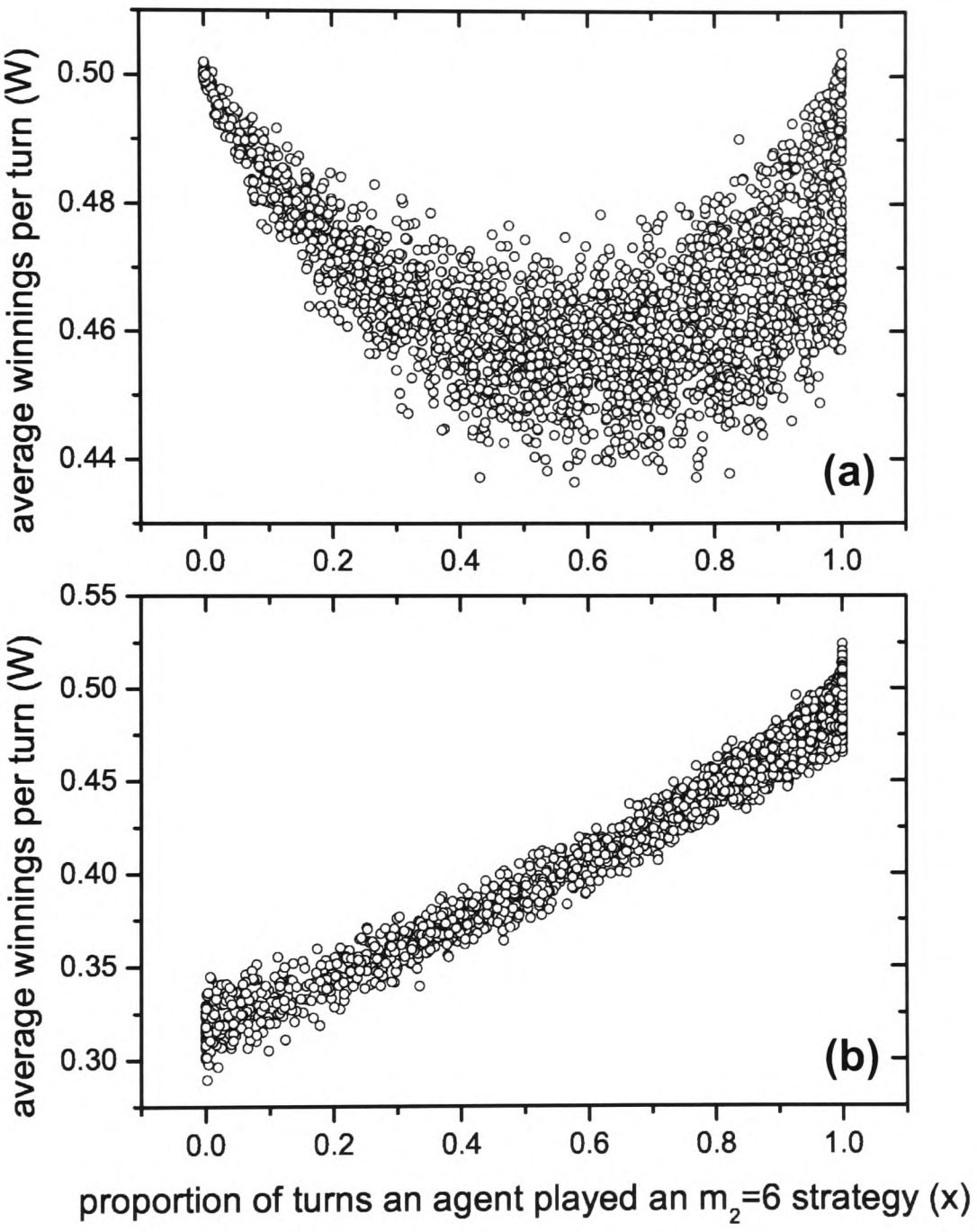

Figure 2.7: Average winnings per turn, W, for multiple memory populations with (a) $s = 3$ and (b) $s = 16$. Each data–point represents a single agent. $N = 101$, $m_1 = 3$ and $m_2 = 6$.

effective penalty. However, we find that the penalty for switching between strategies of different memory lengths is greater and more certain, i.e. W is on average lower and the spread of W values is also smaller. In Fig. 2.7(b), we plot the average winnings per turn for 2525 agents versus the proportion of turns in which an agent played an m_2 strategy. All parameters are the same as for Fig. 2.7(a), except now we have set $s = 16$, with $s_1 = 13$ and $s_2 = 3$. With increasing s it is clear that there is an effective penalty for playing an m_1 strategy. Agents who consistently play m_2 strategies achieve winning percentages higher than 0.5, or that which could be achieved by an external player using a random coin toss to predict the winning market decision. The average winnings per turn for agents who always play m_2 strategies is ~ 0.5.

Figure 2.8 shows the standard deviation in the excess demand, defined previously as $D[t] = n_{+1}[t] - n_{-1}[t]$, for a multiple–memory population (solid circles) as a function of the percentage of strategies which have $m_2 = 6$. The parameters for the populations are the same as for the $s = 16$ multiple–memory population discussed above. The excess demand for our artificial market is the difference between the number of agents who choose to 'buy' ($n_{+1}[t]$) and 'sell' ($n_{-1}[t]$) at each time step. The closer the excess demand is to zero, the higher the number of total points which are awarded each turn. The standard deviation in the excess demand can serve as a proxy for the wastage in the system. The more the standard deviation of excess demand fluctuates each turn, the smaller the total number of points that can be awarded to agents. The population exhibits a minimum in the standard deviation of excess demand at finite $\frac{s_2}{s}$, and at exactly the same value of $\frac{s_2}{s}$ which maximizes the average winnings per agent per turn (see Fig. 2.6). The empty circles represent the standard deviation of the excess demand as predicted by the *Crowd–Anticrowd* theory, which is discussed

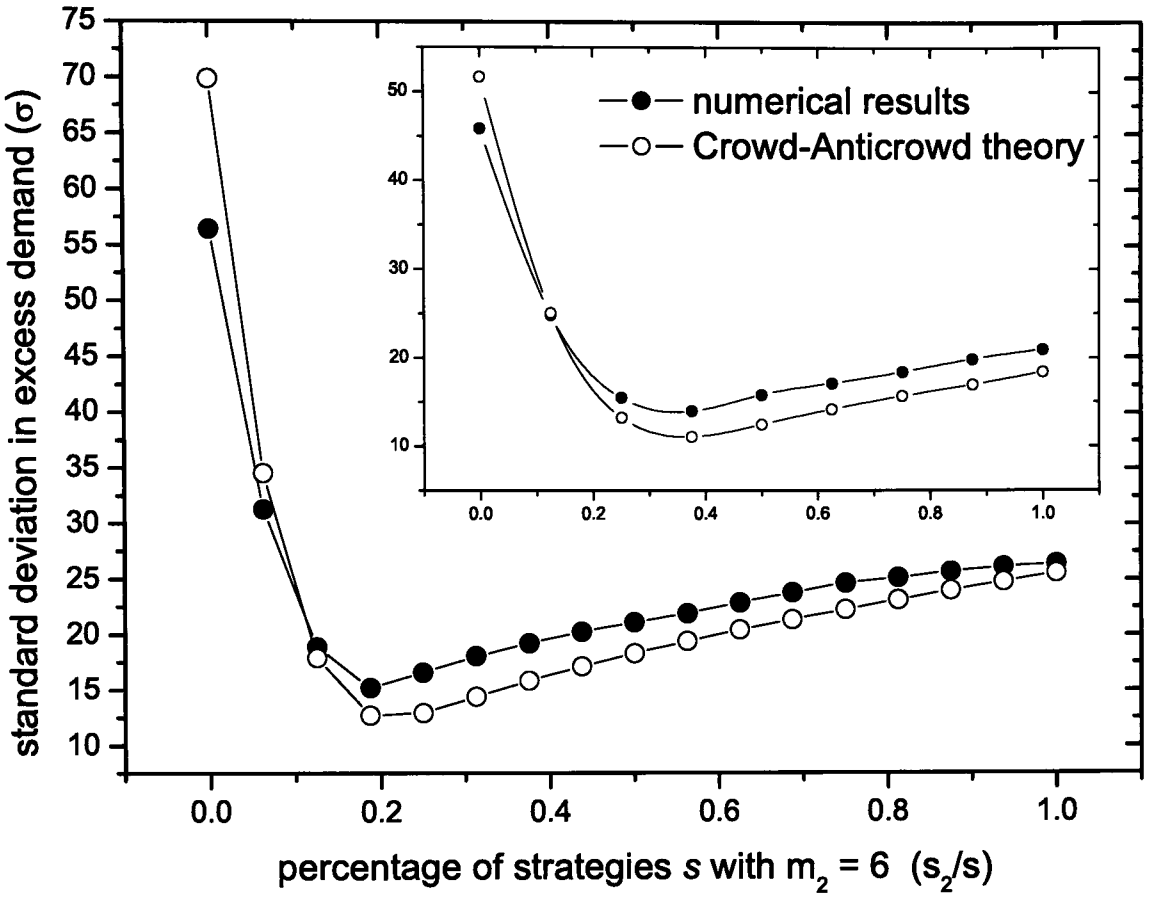

Figure 2.8: Standard deviation in the excess demand σ for multiple–memory populations with $s = 16$ and $s = 8$ (inset) obtained numerically (solid circles) and as predicted by the *Crowd–Anticrowd* theory (empty circles). $N = 101$, $m_1 = 3$ and $m_2 = 6$. See text for an explanation of excess demand and *Crowd–Anticrowd* theory.

in the following section. In the inset we plot the standard deviation in excess demand for an $s = 8$ multiple–memory population, with all other parameters being the same as in the main figure.

2.5.2 Crowd–Anticrowd formalism of multiple–memory population

Our numerical results demonstrate that populations of agents with multiple–memory strategies can outperform both pure populations of agents and mixed–ability populations. This comparative advantage can be explained through the framework of the *Crowd–Anticrowd* theory. As a first approximation, we treat the two groups of agents

playing m_1 and m_2 strategies on a given turn as independent, as per the mixed–ability population [9]. Thus, we examine the *Crowd–Anticrowd* theory as applied to a mixed–ability population. Considering the action of different sub–populations of agents as uncorrelated, the variance in the excess demand for a mixed–ability population goes as $\sigma^2 = \sigma_1^2 + \sigma_2^2$. Here σ_1^2 (σ_2^2) is the variance due to the population of m_1 (m_2) agents, where $\sigma_1^2 = C^2(m_1, s_1)(1-x)^2N^2$ and $\sigma_2^2 = C^2(m_2, s_2)(1-x)^2N^2$. The pre–factor $C^2(m_i, s_i)$ is a constant of proportionality, and x is the proportion of agents playing an m_2 strategy. The standard deviation in excess demand can thus be calculated as:

$$\sigma = N[C^2(m_1, s_1)(1-x)^2 + C^2(m_2, s_2)x^2]^{1/2}. \tag{2.15}$$

For mixed–ability populations x is exogenously determined. However, in the multiple–memory population, x is determined by the relative success of strategies with different memory–lengths. Therefore, we must develop an expression for how agents choose to segregate themselves between playing the m_1 and m_2 strategies.

In order to understand how agents will choose between m_1 and m_2 strategies, we must consider how the strategy spaces are related. Every strategy in the m_1 space maps uniquely to a strategy in the m_2 space. For example, take $m_1 = 3$, $m_2 = 6$ and the m_1 strategy 01101000. This strategy is equivalent to the m_2 strategy 01101000110100001101000011010000110100001101000011010000 [1].

In the *Crowd–Anticrowd* theory, we assume that on each time step the ranking

[1] representing the mapping $\{000000 \rightarrow 0, 000001 \rightarrow 1, 000010 \rightarrow 1, 000011 \rightarrow 0, 000100 \rightarrow 1, 000101 \rightarrow 0, 000110 \rightarrow 0, 000111 \rightarrow 0, 001000 \rightarrow 0, 001001 \rightarrow 1, 001010 \rightarrow 1, 001011 \rightarrow 0, 001100 \rightarrow 1, 001101 \rightarrow 0, 001110 \rightarrow 0, 001111 \rightarrow 0, 010000 \rightarrow 0, 010001 \rightarrow 1, 010010 \rightarrow 1, 010011 \rightarrow 0, 010100 \rightarrow 1, 010101 \rightarrow 0, 010110 \rightarrow 0, 010111 \rightarrow 0, 011000 \rightarrow 0, 011001 \rightarrow 1, 011010 \rightarrow 1, 011011 \rightarrow 0, 011100 \rightarrow 1, 011101 \rightarrow 0, 011110 \rightarrow 0, 011111 \rightarrow 0, 100000 \rightarrow 0, 100001 \rightarrow 1, 100010 \rightarrow 1, 100011 \rightarrow 0, 100100 \rightarrow 1, 100101 \rightarrow 0, 100110 \rightarrow 0, 100111 \rightarrow 0, 101000 \rightarrow 0, 101001 \rightarrow 1, 101010 \rightarrow 1, 101011 \rightarrow 0, 101100 \rightarrow 1, 101101 \rightarrow 0, 101110 \rightarrow 0, 101111 \rightarrow 0, 110000 \rightarrow 0, 110001 \rightarrow 1, 110010 \rightarrow 1, 110011 \rightarrow 0, 110100 \rightarrow 1, 110101 \rightarrow 0, 110110 \rightarrow 0, 110111 \rightarrow 0, 111000 \rightarrow 0, 111001 \rightarrow 1, 111010 \rightarrow 1, 111011 \rightarrow 0, 111100 \rightarrow 1, 111101 \rightarrow 0, 111110 \rightarrow 0, 111111 \rightarrow 0\}$.

of strategies according to success rate and popularity are equivalent. As there is a one–to–one mapping from m_1 strategy space to m_2 strategy space, we will assume that the relative rankings are also preserved in the mapping from m_1 space to m_2 space, (i.e. if strategy A_{m_1} is more popular than B_{m_1}, then we assume that A_{m_2} is more popular than B_{m_2}). Next we assume that an m_2 strategy will, with probability p, have a higher ranking than an agent's best m_1 strategy. Therefore, the agent will play an m_2 strategy with probability

$$x = 1 - (1 - p)^{(s - s_1)}, \tag{2.16}$$

where s is the total number of strategies an agent possesses, and s_1 is the number of m_1 strategies that the agent possesses. In order to determine the value for p, we must first calculate the expected value of the ranking K for the agent's highest–ranked m_1 strategy as a function of s_1 and m_1:

$$E[K_{\max}|s_1] = 2P_1(1 - \frac{s_1}{s_1 + 1}) \tag{2.17}$$

where $P_1 = 2^{m_1}$. If we analyze the strategies in terms of the RSS, the m_1 strategies ranked from 1 to P_1 must map to m_2 strategies in the ranked set $1...P_2$. This is a consequence of the fact that every strategy in the RSS is either anticorrelated or uncorrelated to every other strategy in the RSS. If both strategy spaces are in the crowded regime (i.e. $Ns_1 \gg 2P_1$ and $Ns_2 \gg 2P_2$) and the m_2 strategy space is significantly larger than the m_1 strategy space (i.e. $P_2/P_1 \gg 1$), then the mapping of the ranking of m_1 strategies will fall into the middle range of strategy–rankings of m_2 space. (This assumption should hold if $Ns_1/2P_1 \gg Ns_2/2P_2$). For example, since ordering is preserved, the strategy with $K = 1$ in the m_1 RSS maps to $K = P_2 - P_1 + 1$ in m_2 RSS. Thus, the probability that an m_2 strategy is better than the current most popular m_1 strategy, is $1 - [(P_2 - P_1 + 1)/2P_2] = (P_2 + P_1 - 1)/2P_2$. More generally,

the best m_1 strategy that an agent possesses is the $K_{\max}$th most popular one, given by Eqn. (2.17). The general expression for p then becomes

$$p = \frac{P_2 + P_1(1 - s_1/(s_1+1)) - 1}{2P_2}. \tag{2.18}$$

Our theoretical predictions for the standard deviation of the excess demand are plotted in Fig. 2.8. The agreement with the numerical results is very good. We also note that this agreement actually *improves* with increasing s, a feature that would be very hard to reproduce in comparable spin–glass based theories.

One of the limitations of our theory as outlined so far, is the assumption that the actions of the agents playing an m_1 strategy is uncorrelated to the actions of agents playing an m_2 strategy. As discussed above, the m_2 RSS covers the m_1 RSS – therefore we need to modify Eqn. (2.15) by adding a covariance term. For now, we just comment on the fact, since there is likely to be additional crowding that is unaccounted for, this covariance should be positive and will decrease with increasing x and m_2. We also expect that our expression for x will be an overestimation, since we have assumed that the most popular m_1 strategy is ranked as low as it possibly can be in the m_2 RSS. We believe that these two factors explain why our theoretical predictions for the standard deviation in the excess demand slightly underestimate the numerical results for the multiple–memory populations. We can therefore conclude that multiple–memory populations gain their comparative advantage by behaving as mixed–ability populations with fewer strategies. Additional strategies in the multiple–memory populations will cause the standard deviation in the excess demand to approach the random limit. However, the rate is far slower than in the case of either pure populations or mixed–ability populations.

In game realizations where both the m_1 RSS and m_2 RSS are not crowded (e.g. as

in the $s = 3$ multiple–memory populations in Figs. 2.6 and 2.7) our simple theory for x does not hold. In cases where one of the RSS is not crowded, the highest ranked m_1 strategy can map to a higher–ranked m_2 strategy than we had assumed above. This causes the value for p to be reduced, and could in certain cases cause x to fall below $\frac{s_2}{s}$ as in the $s = 3$ case above. We suspect that this effect is related to the information in the history string. If the m_1 agents can fully access the information in the m_1 length bit–string, but there are insufficient m_2 strategies to access the additional information in the m_2 length bit–strings, it may be more advantageous to play an m_1 strategy. This conjecture is reinforced by the importance of memory in the multiple–memory populations, which we believe is related to the different time scales being tracked by the system. When neither of the RSS are crowded, we expect $x \sim \frac{s_2}{s}$. (This result has been confirmed in numerical simulations with $m_1 = 10$ and $m_2 = 13$).

2.6 Summary and Discussions

We have given an overview of the *Crowd–Anticrowd* theory for a class of competitive multi–agent systems, in particular those based on an underlying binary structure. Explicit analytic expressions can be evaluated at various levels of approximation, yielding very good agreement with numerical simulations. We note that the crucial element of this *Crowd–Anticrowd* theory – i.e. properly accounting for the dominant inter–agent correlations – is not limited to one specific game. Given its success in describing a number of generalized *B–A–R* systems, we believe that the *Crowd–Anticrowd* formalism could provide a powerful approach to describing a wide class of complex systems which mimic competitive multi–agent games. This would be a welcome development, given the lack of general theoretical concepts in the field of complex systems as a whole. It is also pleasing from the point of view of physics methodology, since the

basic underlying philosophy of accounting correctly for 'inter–particle' correlations is already known to be successful in more conventional areas of many–body physics. Of course, some properties of complex systems cannot be described using time– and configuration–averaged expressions as discussed here. In particular, an observation of a real-world complex system which is thought to resemble a multi–agent game, may correspond to a *single* run which evolves from a specific initial configuration of agents' strategies. This implies a particular Ψ, and hence the time–averagings within the *Crowd–Anticrowd* theory must be carried out for that particular choice of Ψ. However, this problem can still be cast in terms of the crowd–anticrowd approach, since the averagings are then just carried out over some subset of paths in history space, which is conditional on the path along which the complex system is already heading.

We have been discussing a complex system based on multi–agent dynamics, in which both deterministic and stochastic processes co–exist, and are indeed intertwined. Depending on the particular rules of the game, the stochastic element may be associated with any of five areas: (i) disorder associated with the strategy allocation and hence with the heterogeneity in the population, (ii) disorder in an underlying network. Both (i) and (ii) might typically be fixed from the outset (i.e., quenched disorder) hence, it is interesting to see the interplay of (i) and (ii) in terms of the overall performance of the system [8]. The extent to which these two 'hardwired' disorders might then compensate each other, as for example in the Parrondo effect or stochastic resonance, is an interesting question. Such a compensation effect might be engineered, for example, by altering the rules–of–the–game concerning inter–agent communication on the existing network. Three further possible sources of stochasticity are (iii) tie–breaks in the scores of strategies, (iv) a stochastic rule in order for

each agent to pick which strategy to use from the available S strategies, as in the Thermal Minority Game, (v) stochasticity in the global resource level $L[t]$ (e.g. bar seating capacity) due to changing external conditions. To a greater or lesser extent, these five stochastic elements will tend to break up any deterministic cycles arising in the game. We refer to Ref. [13] for a discussion of the dynamics of the *Minority Game* viewed from the perspective of a stochastically–perturbed deterministic system.

Bibliography

[1] J.L. Casti, *Would–be Worlds* (Wiley, New York, 1997).

[2] N.F. Johnson, P. Jefferies, P.M. Hui, *Financial Market Complexity* (Oxford University Press, 2003).

[3] B. Arthur, Amer. Econ. Rev. **84**, 406 (1994); Science **284**, 107 (1999).

[4] N.F. Johnson, S. Jarvis, R. Jonson, P. Cheung, Y. Kwong and P.M. Hui, Physica A **258**, 230 (1998).

[5] D. Challet and Y.C. Zhang, Physica A **246**, 407 (1997).

[6] See http://www.unifr.ch/econophysics/minority and E. Moro e-print cond-mat/0402651 (2004) for the full MG-related literature.

[7] See N.F. Johnson and P.M. Hui, e-print cond-mat/0306516 (2003) for more details.

[8] S. Gourley, S.C. Choe, P.M. Hui and N.F. Johnson, Europhys. Lett., **67** (6), pp. 867-873, (2004); e-print cond-mat/0401526 (2004).

[9] N.F. Johnson, P.M. Hui, Dafang Zheng, and M. Hart, J. Phys. A: Math. Gen. **32**, L427 (1999).

[10] A. Cavagna, J.P. Garrahan, I. Giardina and D. Sherrington, Phys. Rev. Lett. **83**, 4429 (1999).

[11] M.L. Hart, P. Jefferies, N.F. Johnson and P.M. Hui, Phys. Rev. E **63**, 017102 (2001).

[12] P. Jefferies, M. Hart, N.F. Johnson, and P.M. Hui, J. Phys. A: Math. Gen. **33**, L409 (2000).

[13] P. Jefferies, M.L. Hart and N.F. Johnson, Phys. Rev. E **65**, 016105 (2002).

Chapter 3

Effects of Local Connectivity in Multi–Agent Complex Systems

3.1 Introduction

There is much current interest in networks within the physics community [1, 2, 3, 4]. Coincidentally, as presented in Chapter 2, there is also great interest in studying populations of adaptive objects ("agents") competing for a global resource [5, 6, 7, 8, 9, 10, 11, 12, 13, 14, 15, 16]. Most network research assumes the nodes are inert, focusing instead on the structural and statistical properties of the connections. By contrast, multi-agent research has focused on adaptive decision-taking agents in the absence of network connections. However, very little has been said about the combination of the two, and hence the *functionality* of such a network, despite its practical importance in many real–world settings [17, 18, 19].

In this chapter, we show that network connections between agents may turn out to be beneficial or detrimental depending on the level of inter–nodal competition. An accurate analytic theory can only be derived if one incorporates both the strong correlations within the internal strategy space of the nodes and the global non–ergodicity. Standard assumptions related to ergodicity, self–averaging and history–independence, therefore fail in this system.

3.2 B–A–R system with a physical network (i.e. B–A–R–N)

Our *B–A–R–N* (Binary Agent Resource Network) system is a networked version of the *B–A–R* system introduced in Chapter 2, which is a simplified binary version of Arthur's *El Farol Bar Problem* concerning bar attendance [5, 6, 7, 8, 9, 10, 11, 12, 13, 14, 15, 16]. Each agent decides its actions in light of i) *global information* which takes the form of the history of the m most recent global outcomes as in the *B–A–R* system, but now has additional ii) *local information* information obtained via network connections. Such connections may be physically tangible (e.g., an electrical connection such as a wire or Internet link) or physically intangible (e.g. information–based as in a wireless communications channel). At each timestep, each agent compares the score of its own best–scoring strategy (or strategies) with the highest–scoring strategy (or strategies) among the agents to whom it is connected. The agent adopts the action of whichever strategy is highest–scoring overall, using a coin–toss to break any ties. For simplicity, we here assume a random network, where the connection between any two agents (i.e. nodes) exists with a probability p. We emphasize that *any* of the above model assumptions can easily be generalized: the numerical results are reasonably robust. All other rules are the same as in the *B–A–R* system.

3.3 Numerical Results for B–A–R–N

Figure 3.1 shows the mean success rate per agent, averaged over many numerical realizations of the underlying connections and strategy distributions (left axis: solid curve) and the success rate distribution within the population for a typical run (right axis: histograms) as a function of the inter–connectivity p, in a modest–resource population illustrated by $L = \frac{N-1}{2}$ (i.e. more losers than winners). We focus on

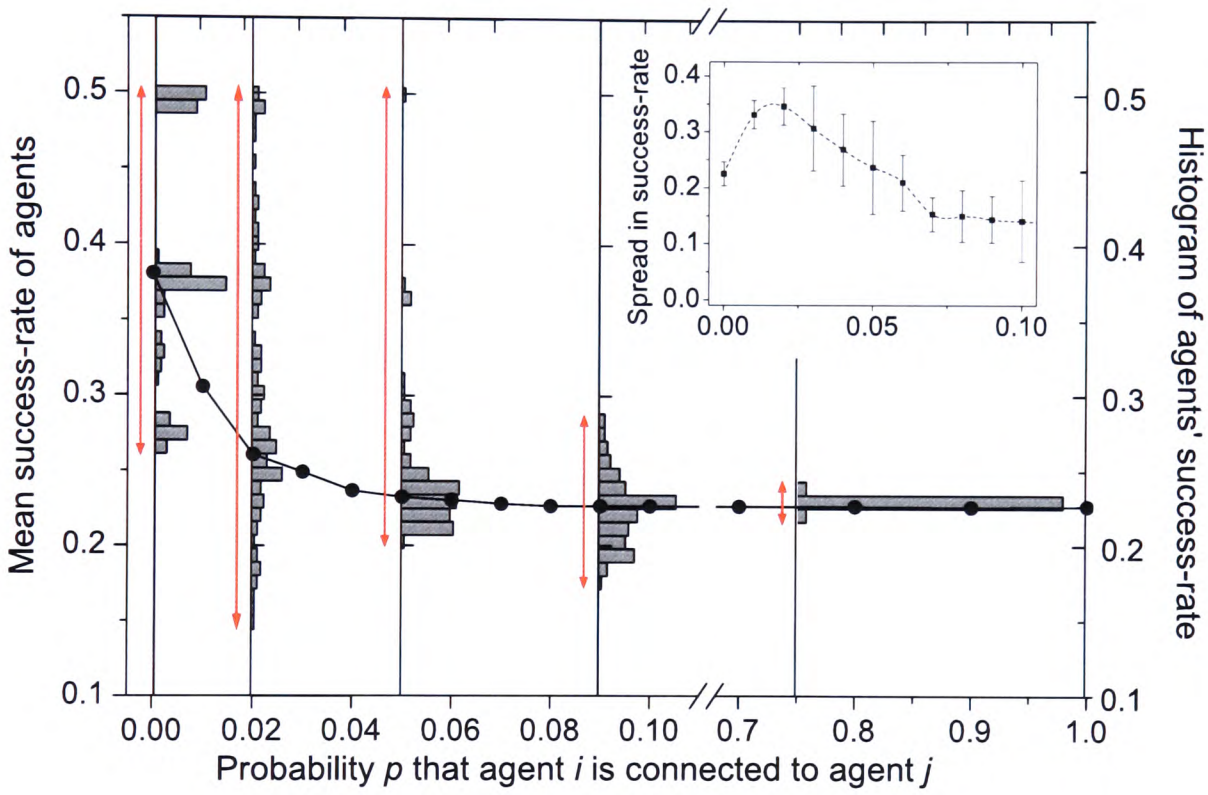

Figure 3.1: Modest resources. Solid line (left axis) shows numerically–obtained mean success rate per agent (node) as a function of the probability p that agent i is connected to agent j. Right axis: typical histograms of agents' success rate in a typical run of 105 timesteps. $N = 101$, $S = 2$, $m = 1$ and $L = 50$. Inset: spread in success rate as a function of p. Error bars obtained from 20 separate runs.

the small m or "crowded" regime [8, 9, 10, 11, 12, 13, 14, 15, 16] since there are relatively few strategies compared to the number of agents and hence many agents will simultaneously be competing to win with the same strategy. The mean success rate decreases rapidly as p increases (left axis: solid curve) before saturating at $p = p_{\rm sat} \sim 0.1$. As m increases, $p_{\rm sat}$ increases. The success rate distribution for a typical run (right axis: histogram) at p = 0 exhibits a definite "class structure" in terms of success. Dramatic changes then arise as p increases. The spread in the success rate – shown explicitly in the inset and by vertical arrows in Fig. 3.1 – indicates a rapid increase in the population's heterogeneity in the range $0 \leq p \leq 0.02$. The success rate distribution becomes almost continuous, washing out the $p = 0$ class structure. Above $p \sim 0.02$, there is a rapid drop in the proportion of highly successful agents. Further increasing p leads to a decrease of the spread in success rates. High levels of inter–connectivity therefore provide increased fairness (i.e. small spread in success rate) but decreased efficiency (i.e. small mean success rate).

3.4 Crowd–Anticrowd formalism incorporating a physical network

Figure 3.2 compares our analytical results using the *Crowd–Anticrowd* theory [14, 15, 16] to the numerical results for the mean success rate per agent. As explained in more detail in Chapter 2, the mean success rate per agent can be obtained from the standard deviation of the number of agents making a given choice (e.g. +1), by averaging this quantity over the attractors of the system (i.e. averaging over the Eulerian trail [21] or subsets of it). The mean success rate can hence be expressed [14, 15, 16] in terms of the mean number, or crowd, of agents using the K-th highest–scoring strategy (i.e. $n_K^{\rm net}$) and the mean number, or anticrowd, of agents using strategy K which is anticorrelated to K (i.e. $n_{\bar{K}}^{\rm net}$, where $\bar{K} = 2^{m+1} + 1 - K$). Explicitly,

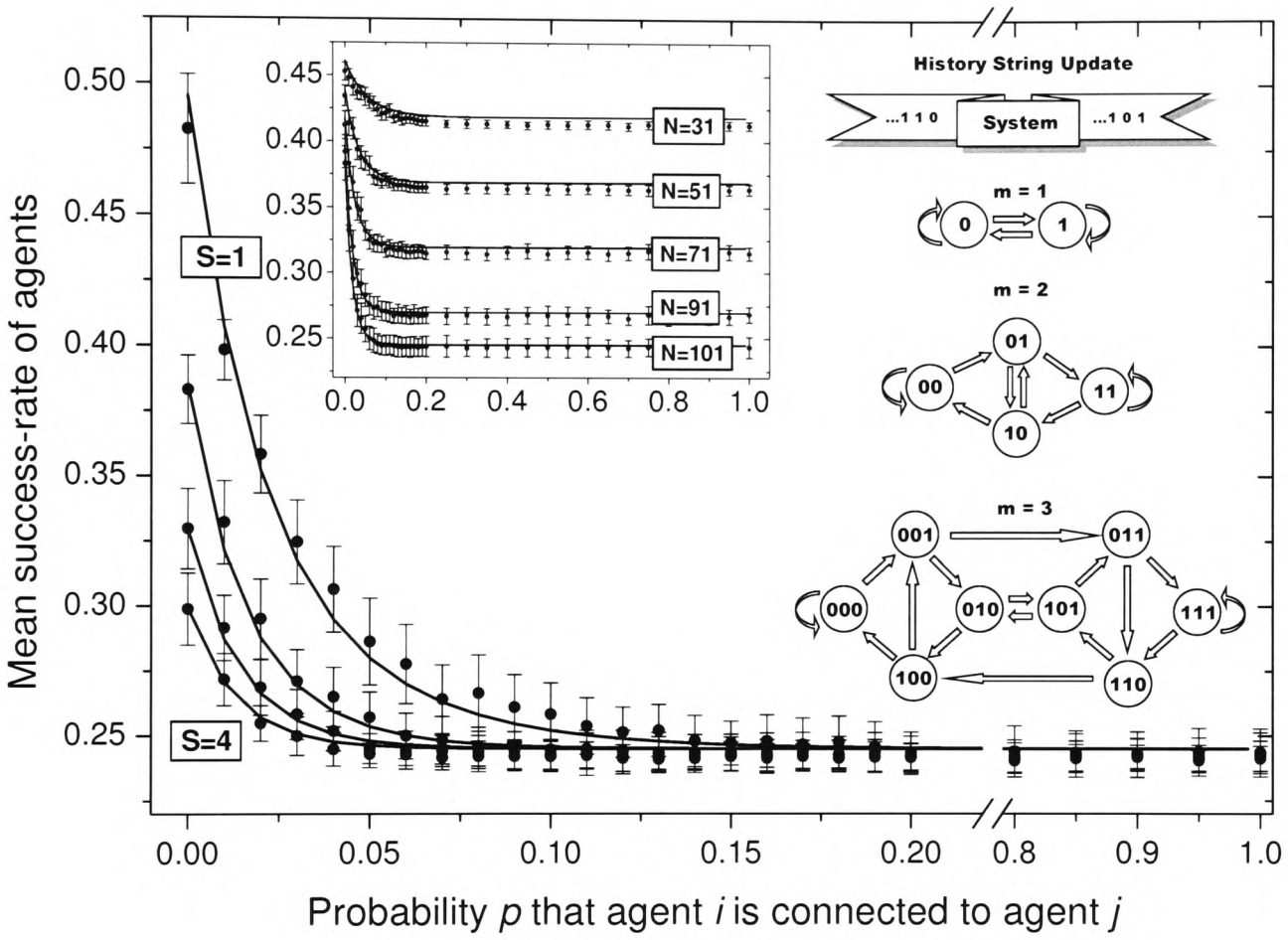

Figure 3.2: Solid lines show analytic *Crowd–Anticrowd* theory for mean success rate per agent (node) with modest resources, for $S = 1, 2, 3, 4$. Data-points are numerical results. $m = 1$, $N = 101$, $L = 50$. Inset: $S = 2$, various N values. Right: Eulerian Trails [21] (i.e. high p attractor) for $m = 1, 2, 3$.

$$n_K^{\text{net}} = n_K + n_{\rightarrow K} - n_{K\rightarrow} \ , \tag{3.1}$$

where n_K is the number of agents who would have used strategy K in the absence of the network because of the initial random strategy allocation:

$$n_K = N\left(\left[1 - \frac{K-1}{2^{m+1}}\right]^S - \left[1 - \frac{K}{2^{m+1}}\right]^S\right) \ . \tag{3.2}$$

In short, n_K is the intrinsic crowd–size due to crowding in the global strategy space. $n_{\rightarrow K}$ is a sum over all agents who use strategy K as a direct result of a network connection:

$$n_{\rightarrow K} = \Big[\sum_{J>K} n_J\Big]\Big[\Big(1-p\Big)^{\sum_{G<K} n_G}\Big]\Big[1 - \Big(1-p\Big)^{n_K}\Big] \tag{3.3}$$

Hence $n_{\rightarrow K}$ represents the increase in crowd–size due to the local connectivity. By contrast, $n_{K\rightarrow}$ is a sum over all agents who would have used K in the absence of a network, but who will now use a better strategy as a result of their network connections:

$$n_{K\rightarrow} = n_K\Big[\ 1 - \Big(1-p\Big)^{\sum_{G<K} n_G}\ \Big] \ . \tag{3.4}$$

Hence $n_{K\rightarrow}$ represents the decrease in crowd–size due to the local connectivity. The resulting analytic expressions for the mean success rate are in excellent agreement with numerical results (see Fig. 3.2).

Figure 3.3 shows the regime changes which arise as a function of the inter-connectivity p in higher–resource populations. If the global resource level L exceeds a critical amount $L_{\text{crit}} = \frac{3N}{4}$, the mean success rate per agent can exhibit a *maximum* at small but finite inter-connectivity, for the following reason. When $L > L_{\text{crit}}$ and $p = 0$, the population inhabits a "frozen" state in the sense that the global outcome is

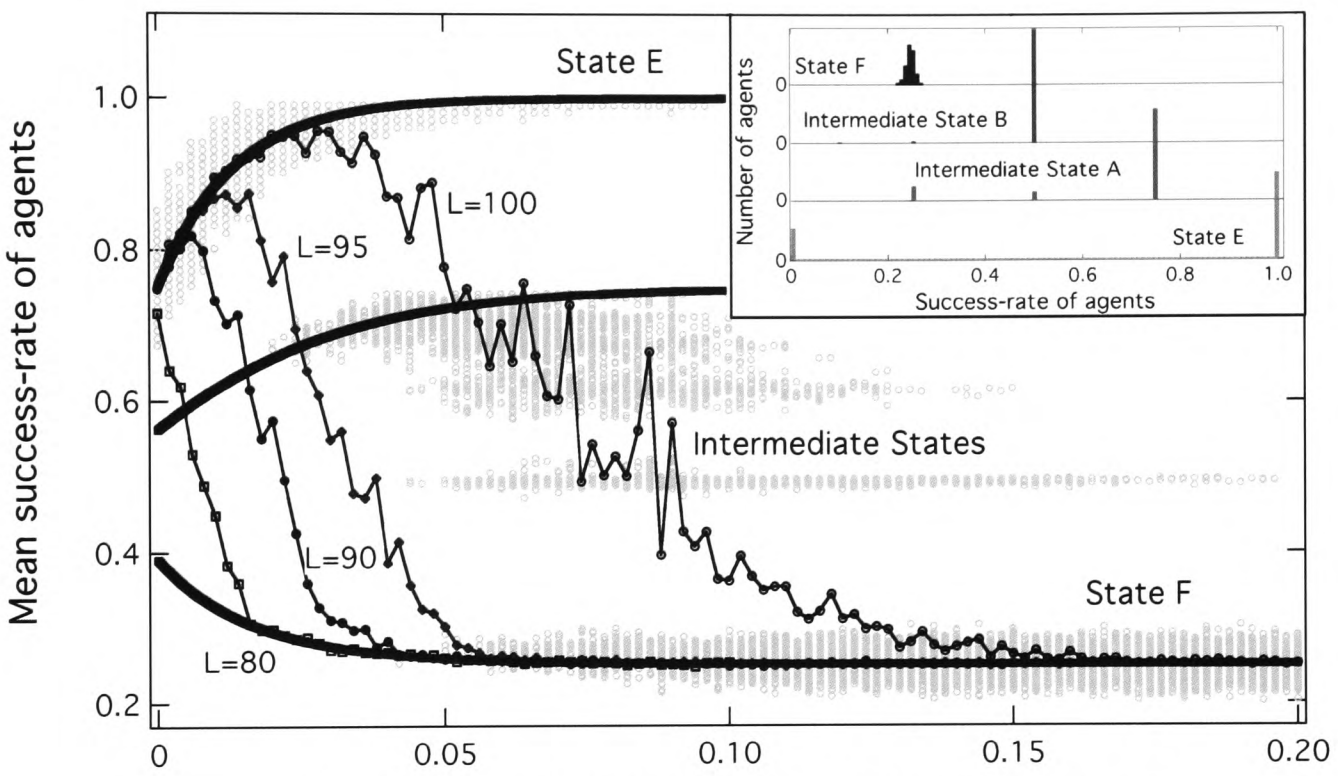

Figure 3.3: Higher resources. Thin solid lines: numerically obtained mean success rate per agent (node) as a function of p, at resource levels $L = 80, 90, 95, 100$. Results averaged over 200 runs of 105 timesteps, with $N = 101$, $S = 2$, $m = 1$. Scattered circles show mean success rate per agent for separate runs at $L = 100$ with $m = 1$, as an illustration. Thick solid lines: analytic curves (Eqns. (3.5)-(3.7)) describing the three dynamical regimes. The analytic curves obscure some of the numerical results. Inset: histograms of typical success rate distribution, for $L = 100$, $m = 1$.

persistently 1, i.e. ...111111. With $S = 2$ as in Fig. 3.3, each agent has probability $\frac{1}{4}$ of being assigned two strategies which both define action -1 following a string of m "1"s. Thus, approximately $\frac{1}{4}$ of the population always lose and $\frac{3}{4}$ of the population always win, leading to $L_{\text{crit}} = \frac{3}{4} \approx 75$. The global resource is therefore under–used at $p = 0$ by $\Delta L \approx \left(L - \frac{3N}{4}\right)$ at each timestep. Therefore, increasing p away from $p = 0$ will benefit some of the less successful agents by connecting them up to successful agents, thereby giving them access to ΔL, until a p value is reached where the connectivity is sufficient to break the outcome series of 1's. These run–averaged results can be better understood by considering run–specific results for $L = 100$ as an illustrative case (scattered circles). Specific runs appear to aggregate into groups having similar temporal dynamics and success rate distributions – these groups correspond to different dynamical states of the system. The increase in the mean success rate at low p, corresponds to the system following an *Efficient* State E which has an outcome series of 1's as discussed above. The success rate distribution (inset) for State E is characterized by groups of persistent winners and losers. As p increases further, the outcome series for high L tends to move through a set of Intermediate States which combine a low spread in success rate with a high mean (e.g. Intermediate States A and B). In Intermediate State A, the least successful agents (which in State E had zero success) now have a success rate which *exceeds* the average success rate in the high connectivity limit. In the high p limit, the outcome series tends toward the period–4 Eulerian trail [21] given by ...00110011.... The corresponding number of agents taking action $+1$ follows the pattern $\ldots N, N, \frac{N}{2}, \frac{N}{2}, N, N, \frac{N}{2}, \frac{N}{2} \ldots$. The resulting *Fair* State F corresponds to all agents having access to the best performing strategies, either by being assigned that strategy or by being connected to another agent with that strategy. The resulting system is fair but inefficient, having a small

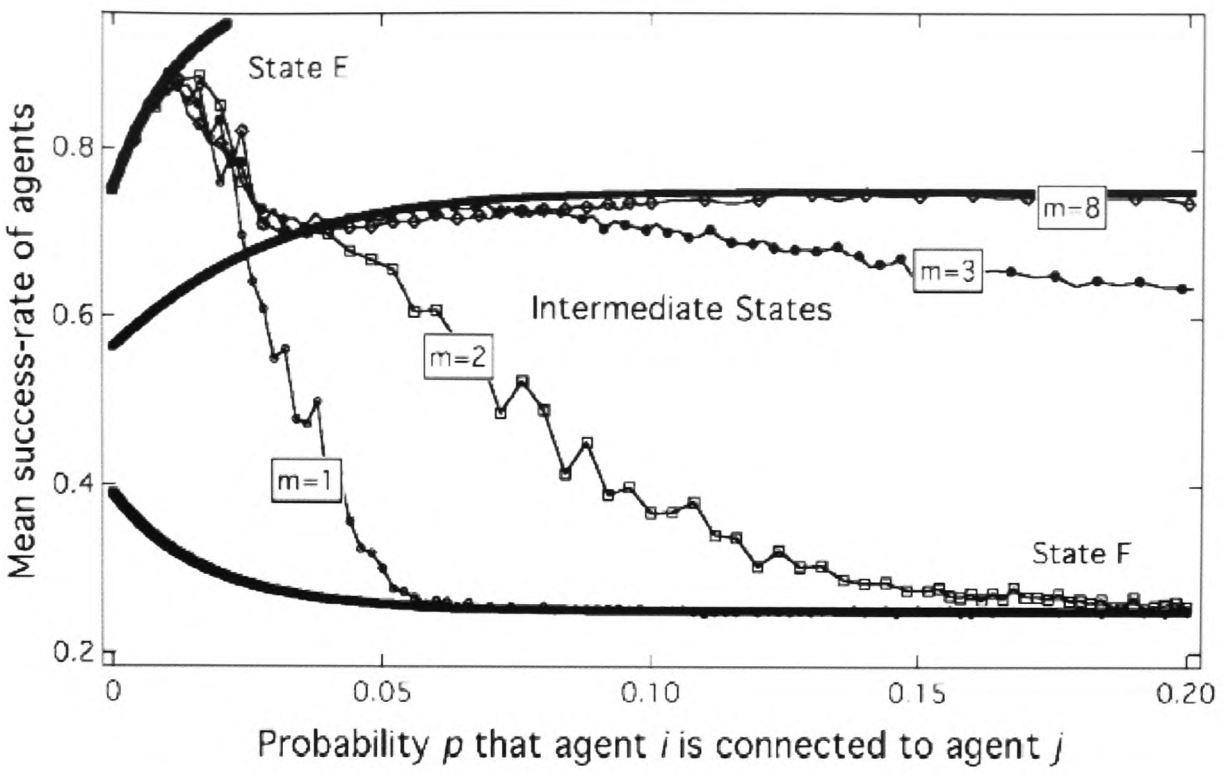

Figure 3.4: High resources. Thin solid lines: numerically obtained mean success rate per agent (node) as a function of p, at various m. Results averaged over 200 runs of 10^5 timesteps, with $N = 101$, $S = 2$, $L = 95$. Thick solid lines: analytic curves (Eqs. (3.5)-(3.7)) describing the three dynamical regimes. The analytic curves obscure some of the numerical results.

spread but also a small mean success rate ≈ 0.25.

Figure 3.4 shows how these transitions between regimes in high–resource populations (e.g. $L = 95$), vary with history bit–string length m. The Intermediate States, characterized by a reasonably high mean success rate and a reasonably small spread (see Fig. 3.3 inset), have an increasingly dominant effect on the system's behaviour as m increases. For a particular value of m, increasing p moves the system toward cycles of increasing period and hence the fractions of 1's and 0's in the output series become more equal. The resulting State F, which represents an increasingly noisy version of the Eulerian trail as m increases, is fair but inefficient (see Fig. 3.3 inset).

We have derived analytic expressions, within the *Crowd–Anticrowd* formalism including non–ergodicity, which describe well the three regimes (thick solid lines in

Figs. 3.3 and 3.4). The upper analytic branch at low p, describing the efficient State E, is given by

$$\frac{3}{4} + \frac{1}{4}\left[1 - (1-p)^{\frac{3N}{4}}\right] . \tag{3.5}$$

The middle analytic branch at intermediate p, describing the Intermediate States, is given by

$$\frac{3}{4} - \frac{9}{32}(1-p)^{\frac{7N}{16}} - \frac{1}{32}(1-p)^{\frac{15N}{16}} + \frac{1}{8}(1-p)^{\frac{3N}{4}} . \tag{3.6}$$

The lower analytic branch at high p, describing the fair State F, is given by

$$\frac{1}{4} + \frac{9}{128}(1-p)^{\frac{7N}{16}} + \frac{1}{128}(1-p)^{\frac{15N}{16}} + \frac{1}{16}(1-p)^{\frac{3N}{4}} . \tag{3.7}$$

The outcome series of 1's at low p which yield State E can persist up to $p_{\text{crit}} \sim 1 - \left(1 - \frac{4\Delta L}{N}\right)^{\frac{4}{3N}}$. For $L = 80, 90, 95$ and 100, this yields $p_{\text{crit}} \sim 0.002, 0.011, 0.019$ and 0.042, respectively, which are also all in excellent agreement with the numerical results.

3.5 Summary

This chapter reported rich dynamical effects arising within a network comprising heterogeneous, adaptive nodes (i.e. agents). One might question the generality of our results. Such questions were also levied at early studies of other non–linear dynamical systems – however, we now know that there are beautiful examples of universality associated with chaos, phase transitions and other self–organized phenomena [22, 23]. Our belief is that by developing a quantitative understanding of fairly generic models such as ours, one may eventually uncover such universality in a wider class of network–based complex systems.

Bibliography

[1] Callaway D. S., Newman M. E. J., Strogatz S. H. and Watts D. J., Phys. Rev. Lett., **85**, 5468 (2000).

[2] Albert R. and Barabasi A. L., Phys. Rev. Lett., **85**, 5234 (2000).

[3] Newman M. E. J., Moore C. and Watts D. J., Phys. Rev. Lett., **84**, 3201 (2000).

[4] Albert R. and Barabasi A. L., Rev. Mod. Phys., **74**, 47 (2002).

[5] Arthur W. B., Science, **284**, 107 (1999).

[6] Anghel M., Toroczkai Z., Bassler K. E. and Kroniss G., Phys. Rev. Lett., **92**, 058701 (2004).

[7] Caridi I. and Ceva H., cond-mat/0401372 (2004).

[8] Challet D., Marsili M. and Zecchina R., Phys. Rev. Lett., **84**, 1824 (2000).

[9] Cavagna A., Garrahan J. P., Giardina I. and Sherrington D., Phys. Rev. Lett., **83**, 4429 (1999).

[10] Savit R., Manuca R. and Riolo R., Phys. Rev. Lett., **82**, 2203 (1999).

[11] Johnson N. F., Hui P. M., Jonson R. and Lo T. S., Phys. Rev. Lett., **82**, 3360 (1999).

[12] Soulier A. and Halpin-Healy T., Phys. Rev. Lett., **90**, 258103 (2003).

[13] Hod S. and Nakar E., Phys. Rev. Lett., **88**, 238702 (2002).

[14] Johnson N. F. and Hui P. M., cond-mat/0306516;

[15] Hart M., Jefferies P., Johnson N. F. and Hui P. M., Physica A, **298**, 537 (2001);

[16] Johnson N. F., Jefferies P. and Hui P. M., *Financial Market Complexity* (Oxford University Press, Oxford) 2003

[17] Hogg T., Nanotechnology, **10**, 300 (1999);

[18] Sole R. V. and Goodwin B., *Signs of Life* (Basic Books, New York) 2000, 1999, p. 300.

[19] Barabasi A. L. and Oltvai Z. N., Nature (Genetics), **5**, 101 (2004).

[20] Challet D. and Johnson N. F., Phys. Rev. Lett., **89**, 028701 (2002)

[21] The Eulerian Trail corresponds to a particular cycle around the de Bruijn graph in which every possible transition between global information states is visited once. The de Bruijn graph represents the 2^m possible global information states.

[22] Strogatz S. H., *Nonlinear Dynamics and Chaos* (Addison-Wesley, Reading Mass.) 1995.

[23] Kadanoff L. P., *Statistical Physics* (World Scientific, Singapore) (2000).

Chapter 4

Error–driven Global Transition in a Network–based Multi–Agent Complex System

4.1 Introduction

Chapter 3 provided one of the only known studies of the effect of a network in a competitive multi–agent population, such as the *Minority Game* (MG) or *El Farol Bar Problem* (EFBP) [3, 4, 5, 6, 7]. To date, all studies have assumed that any information shared between agents is always perfectly accurate. However, real–world complex systems do not operate at such levels of perfection. Furthermore, informational networks might be used by agents to spy and mislead rather than to benefit others. This raises the following question: What is the effect of networks within a competitive population such as the MG, where the information transmitted is corrupted?

In this chapter we show analytically and numerically that erroneous data transmission generates an abrupt global transition within a competitive, networked population playing the *Minority Game* (again as a reminder, the *Minority Game* is a special case of the B–A–R system with resource $L = \frac{N-1}{2}$). This phase–like transition is driven by a temporal symmetry–breaking in the global outcome series. We then show how the *Crowd–Anticrowd* formalism, which accounts for the many-body (i.e. many-agent)

correlations inherent in the system, provides a quantitative yet physically intuitive explanation of this phase transition.

4.2 B–A–R–N model with erroneous information

We start with the same model set–up as the B–A–R–N model introduced in Chapter 3. In this chapter we restrict our results and analysis to the *Minority Game*. Agents use the connections they have, if any, to gather information from other agents. For simplicity we assume a random network between agents, fixed at the beginning of the game. The connection between any two agents exists with a probability p, hence each agent is on average connected to $p(N-1)$ others. At a given timestep t, and with a given global history $\mu(t)$, each agent takes the action predicted by the highest–scoring strategy among his own *and* those of the agents to which he is connected, exactly as in the *B–A–R–N* system.

We now introduce the parameter q, which is the probability that an *error* arises in the information the agent gathers from his cluster. Alternatively, q can be viewed as the weight an agent places on the information gathered from his cluster. For example, if the action of the best strategy in his cluster is $+1$, the agent records this as a -1 with probability q (and vice versa for a best action -1). The information transmission has been corrupted with probability q. Any agent with a higher-scoring strategy than those of his neighbours at a given timestep, is unaffected by this error – the only source of stochasticity which might affect him is the standard coin-toss used to break any ties between his own strategies [8, 9, 10]. In contrast to the agents' "on-site" stochastic strategy selection arising in the "Thermal Minority Game" (TMG) [11, 12, 13], the stochasticity associated with q in our game depends on the agents' connectivity.

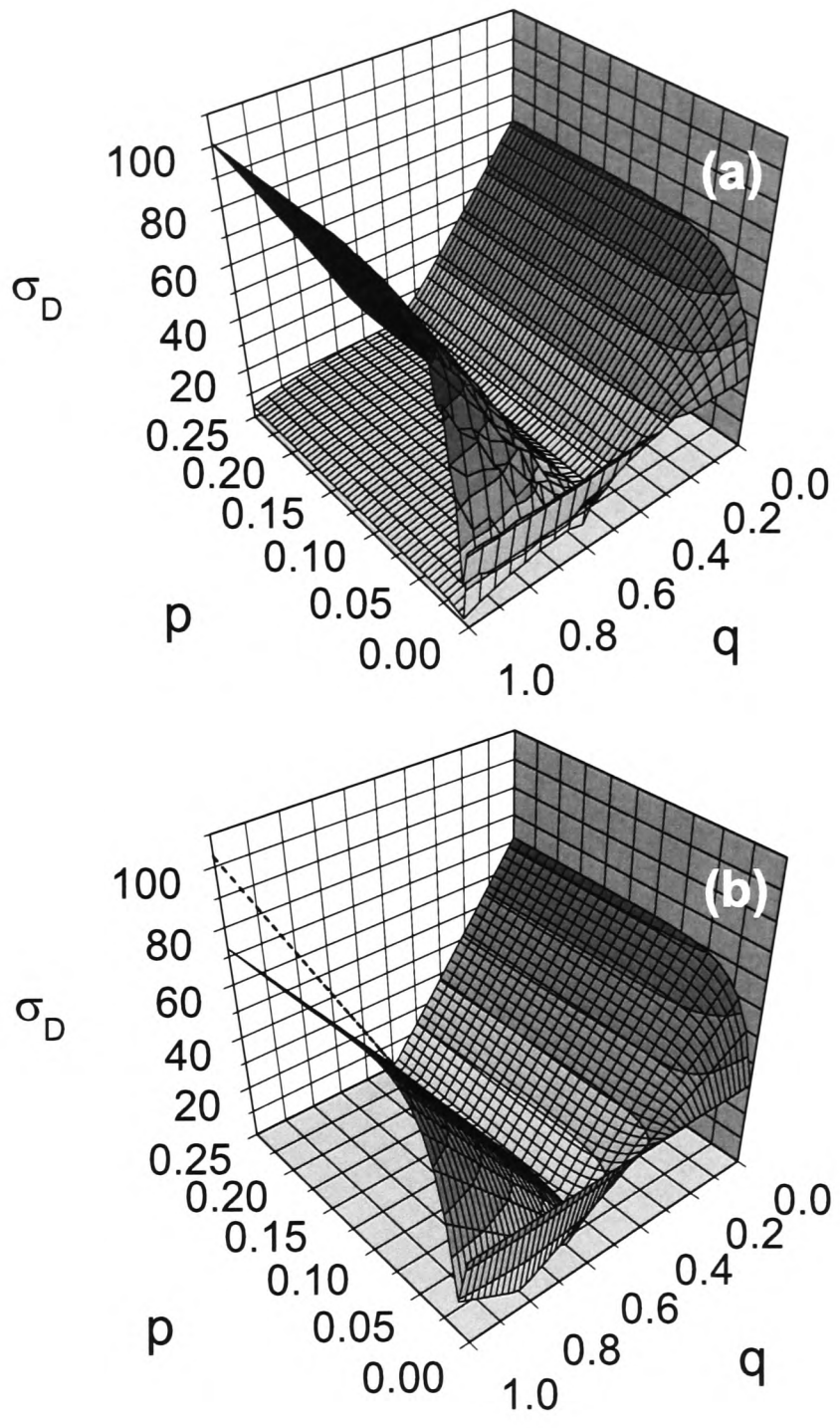

Figure 4.1: Fluctuation in excess demand, σ_D, as a function of the error probability q and the network connectivity p. (a) Numerical results averaged over 300 runs, each with 10^5 iterations. (b) Analytic *Crowd–Anticrowd* theory. At high q, the two branches in (a) correspond to different dynamical attractor states, while the single branch in (b) represents an effective average (see text). The dotted line in (b) at $p = 0.25$, illustrates the modified analytical results for the upper branch if one assumes some knowledge of this branch's global output series. Parameters: $m = 1$, $S = 2$, and $N = 101$.

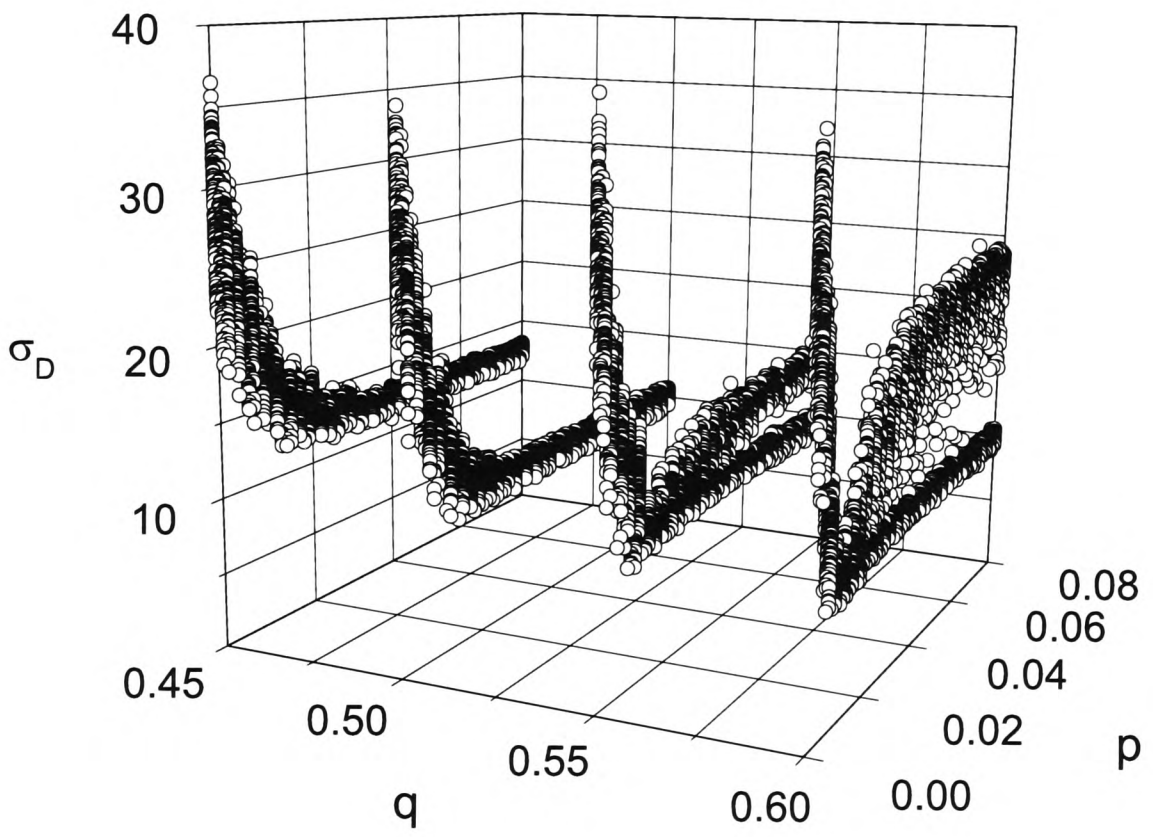

Figure 4.2: Numerical results for individual runs, showing the fluctuation in excess demand, σ_D, around $q = 0.5$. Parameters as in Fig. 4.1.

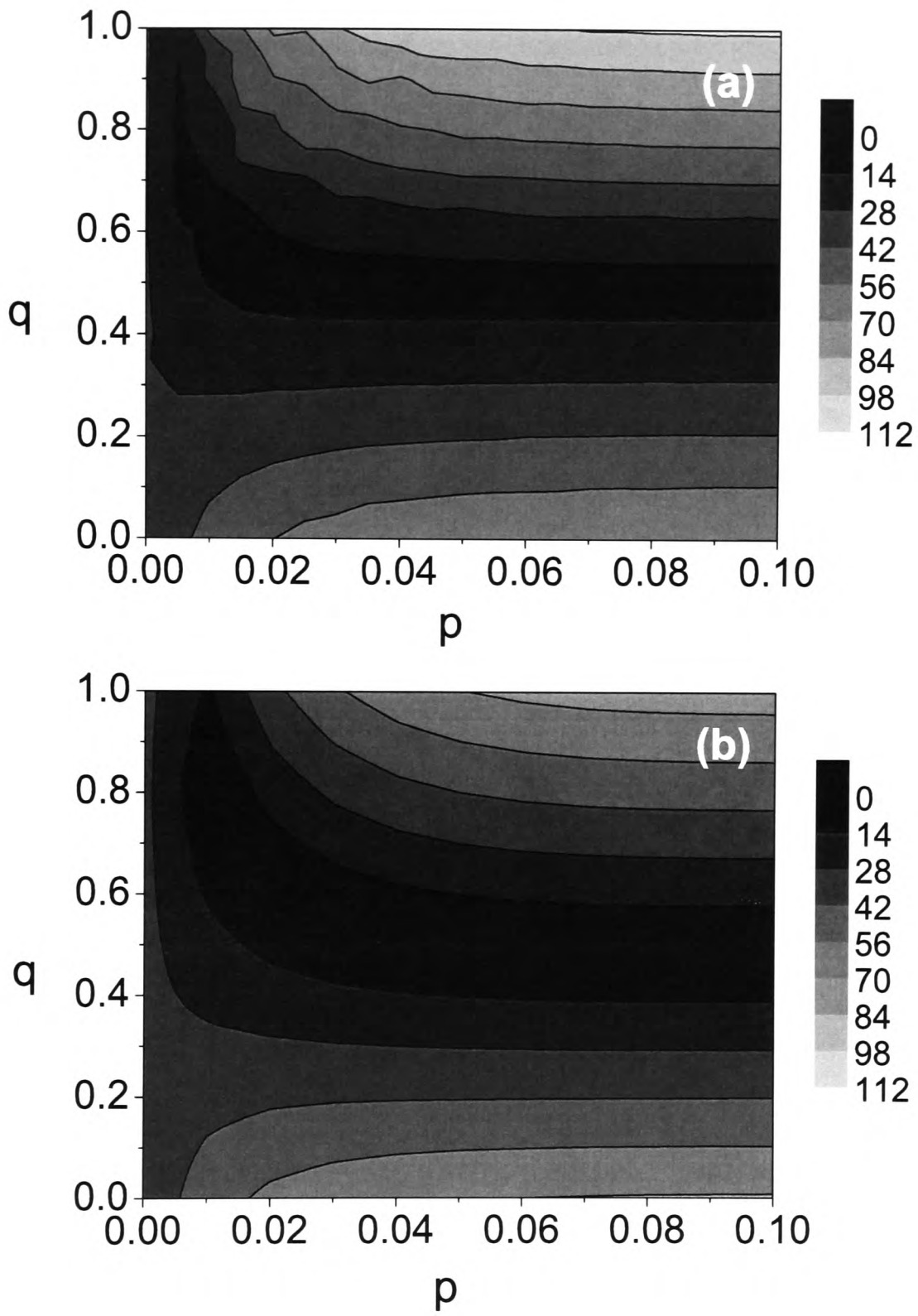

Figure 4.3: Contour map version of Fig. 4.1. Contours correspond to a constant value of σ_D as a function of the error-probability q and the network connectivity p. (a) Numerical results. (b) Analytic *Crowd–Anticrowd* theory. For clarity, only the upper branch of the numerical results is shown for the high-q phase.

4.3 Crowd–Anticrowd formalism of B–A–R–N with erroneous information

We now investigate the effects of this *microscopic* connection-driven data error on the system's *macroscopic* dynamics. We shall build an analytic theory based on the *Crowd–Anticrowd* theory [8, 9, 10] which incorporates the many-agent (many-body) correlations arising in the system's strategy space as a result of the dynamics in the history space. To a very good approximation, we can replace the Full Strategy Space by a Reduced Strategy Space (RSS) [14, 15, 16, 17, 18] which provides a minimal basis set of strategies for the system [8, 9, 10]. The appropriate choice for the RSS depends on the relative frequency of visits to the 2^m histories. With all histories visited equally often, the RSS comprises a total of $2P = 2 \cdot 2^m$ strategies [14, 15, 16, 17, 18]. We will examine how the interplay between p and q affects the fluctuations in the excess demand $D(t)$. As emphasized in previous MG works, small fluctuations in $D(t)$ are signatures of an efficient self-organization within the population [14, 15, 16, 17, 18, 8, 9, 10, 11, 12, 3, 4, 5, 6]. The excess demand $D(t)$ at timestep t is given by

$$D(t) = n_{+1}(t) - n_{-1}(t) = \sum_{K=1}^{K=2P} a_K n_K(t) \ , \tag{4.1}$$

where $n_{+1}(t)$ $[n_{-1}(t)]$ is the number of agents taking action $+1$ (-1); $a_K = \pm 1$ is the action predicted by strategy K in response to history $\mu(t)$ and $n_K(t)$ is the number of agents using strategy K at time t. K labels the K'th highest scoring strategy while $\overline{K} = 2P + 1 - K$ labels the anti-correlated strategy. In the non-networked MG at low m, $D(t)$ exhibits large, crowd-driven fluctuations while $\mu(t)$ follows a quasi-deterministic Eulerian trail in which all histories $\{\mu(t)\}$ are visited equally [19]. Hence, the time-averages $\langle n_{-1}(t) \rangle = \langle n_{+1}(t) \rangle$ yielding $\langle D(t) \rangle = 0$ which is the optimal

value for $D(t)$. We continue this focus on small m here, since we are interested in the effect of q on these crowd–driven fluctuations. We will assume that the combined effect of averaging over t for a given Ψ (where Ψ is a given realization of the initial strategy allocation matrix [8, 9, 10]), *and* averaging over Ψ, will have the same effect as averaging over all histories. This is true for the non–networked MG, and produces a mean $D(t)$ of zero. Hence the fluctuation (i.e. standard deviation) of the excess demand, σ_D, is given by:

$$\sigma_D^2 = \left\langle \sum_{K=1}^{P} \left(n_K(t) - n_{\overline{K}}(t)\right)^2 \right\rangle_{t,\Psi} \approx \sum_{K=1}^{P} \left(n_K^{\text{mean}} - n_{\overline{K}}^{\text{mean}}\right)^2 \ . \tag{4.2}$$

We have used the orthogonality properties of the vectors with elements a_K where $K = 1, 2, \ldots, 2P$ [8, 9, 10]. Since $n_K(t)$ will generally fluctuate around some mean value n_K^{mean}, we have also written $n_K(t) = n_K^{\text{mean}} + \epsilon_K(t)$ and assumed that the fluctuation terms $\{\epsilon_K(t)\}$ are uncorrelated stochastic processes. In Eqn. (4.2),

$$n_K^{\text{mean}} = n_K + n_{\rightarrow K}^q - n_{K\rightarrow}^q - n_K^q \tag{4.3}$$

and similarly for $n_{\overline{K}}^{\text{mean}}$, where:

(1) n_K is the mean number of agents whose own best strategy is actually the K'th highest scoring strategy in the game [8, 9, 10]:

$$n_K = N\Big[\Big(1 - \frac{K-1}{2^{m+1}}\Big)^S - \Big(1 - \frac{K}{2^{m+1}}\Big)^S\Big] \ . \tag{4.4}$$

(2) $n_{\rightarrow K}^q$ is the mean number of agents who only possess strategies worse (i.e. lower scoring) than K, but who will use strategy K due to connections they have to one or more agents who each possess strategy K but no better

$$n_{\rightarrow K}^q = \Big(1 - q\Big) \cdot n_{\rightarrow K} + q \cdot n_{\rightarrow \overline{K}} \ , \tag{4.5}$$

where

$$n_{\rightarrow K} = \Big[\sum_{J>K} n_J\Big]\Big[\Big(1-p\Big)^{\sum_{G<K} n_G}\Big]\Big[1-\Big(1-p\Big)^{n_K}\Big] \tag{4.6}$$

with $n_{\rightarrow \overline{K}}$ being obtained from Eqn. (4.6) by setting $K \rightarrow \overline{K} = 2P + 1 - K$.

(3) $n^q_{K\rightarrow}$ is the mean number of agents who possess strategy K, but who will nevertheless use a strategy better than K due to connections:

$$n^q_{K\rightarrow} = \Big(1-q\Big)\cdot n_{K\rightarrow} + q\cdot n_{\overline{K}\rightarrow}\ , \tag{4.7}$$

where

$$n_{K\rightarrow} = n_K\Big[\ 1-\Big(1-p\Big)^{\sum_{G<K} n_G}\ \Big] \tag{4.8}$$

and similarly for $n_{\overline{K}\rightarrow}$.

(4) n^q_K accounts for the situation in which an agent is connected to other agents with the same highest scoring strategy K as him. q therefore gives the probability that this agent will take the opposite action to strategy K

$$n^q_K = q\cdot n_K\Big[1-\Big(1-p\Big)^{n_K}\Big] - q\cdot n_{\overline{K}}\Big[1-\Big(1-p\Big)^{n_{\overline{K}}}\Big]\ . \tag{4.9}$$

4.4 Comparison to numerical results

Figure 4.1 compares the numerical and analytical results for σ_D, which is the standard deviation in excess demand. The agreement is remarkable given the complexity of σ_D as a function of p and q. As the "noise" level q increases, the system undergoes a change in regime at a critical connectivity p defined by the critical boundary $C_{\text{crit}}(q,p)$. Moving across $C_{\text{crit}}(q,p)$, the symmetry in the global outcome string is spontaneously

broken in a manner reminiscent of a phase transition. Specifically, the global outcome series changes from the low-q phase where it resembles the period-4 Eulerian trail [19] ... 00110011 ..., to a high-q phase where it comprises *two* distinct branches [see Fig. 4.1(a)]. Figure 4.2 shows individual runs near the critical noise threshold. The higher branch corresponds to a period-2 global outcome series ... 1010 ... which is *antiferromagnetic* if we denote 0 (1) as a *spatial* spin up (down) as opposed to a *temporal* outcome. The lower branch corresponds to the period-1 series of frozen outcomes ... 0000 ... or ... 1111 ..., i.e. *ferromagnetic.* In this high-q phase, the system will choose one of these two global outcome branches spontaneously, as a result of the type and number of links each agent has. This symmetry–breaking of the global outcome series along the channel of minimum fluctuation in Fig. 4.1, $C_{\rm crit}(q,p)$, originates in the internal coupling between the history dynamics, the strategy space and the individual agent networks. Because of the initial strategy allocation and connections, many agents will have an in–built bias towards one of the two possible actions and hence act in a deterministic or decided way at a given timestep. However, there exist a few undecided agents who need to toss an unbiased coin to decide between the equally balanced signals they gather from their local network. It is the fluctuations of these few undecided agents who then push the system onto a particular branch.

4.4.1 Corrections to theory

We now discuss two technical details. First, there are many ties in strategy scores at very small m, and hence many tie–break coin tosses. This means that the fluctuation terms $\{\epsilon_K(t)\}$ can no longer be ignored. The $m = 1$ surface in Fig. 4.1(b) was therefore produced by averaging over the $2 \cdot 2^m = 4$ timesteps in the Eulerian trail [19]. In other words, the double average in Eqn. (4.2) was evaluated over the $2 \cdot 2^m = 4$ timesteps in the Eulerian trail. When a tie–break between the strategies $K = 1$

and $K = 2$ arises at one of the four timesteps, one replaces $n_{K=1}^{\text{mean}}$ and $n_{K=2}^{\text{mean}}$ by $\frac{1}{2}(n_{K=1}^{\text{mean}} + n_{K=2}^{\text{mean}})$ at that timestep, as one does for tie–breaks between any other K and K'. In this way, the average over the Eulerian trail is easily evaluated analytically. As m increases, there are more timesteps over which one must average (i.e. $2P = 2 \cdot 2^m$ timesteps). However, since ties also become less frequent as m increases, one can simply ignore them without significant loss of accuracy (see Ref. [8, 9, 10] in which good agreement is obtained for the non-networked MG for a wide range of m values without considering ties). Second, the theory has assumed the non-networked MG result that the dynamics follow the Eulerian trail. Only one branch therefore emerges in Fig. 4.1(b) at high q, appearing like some effective average over the global output series for all branches in Fig. 4.1(a). If instead one uses knowledge of the actual global output series for these separate branches (i.e. antiferromagnetic or ferromagnetic), then results even closer to Fig. 4.1(a) can be obtained. This is illustrated at one particular p by the dotted line in Fig. 4.1(b).

Figure 4.3 provides a contour plot of σ_D around the minimum. The black contour, centred around the critical curve $C_{\text{crit}}(q, p)$, effectively separates the two different regimes of behaviour. The low σ_D values around $C_{\text{crit}}(q, p)$ can be easily understood using the physical picture provided by the *Crowd–Anticrowd* theory: the stochasticity induced by q (i.e. noise) breaks up the size of the crowds using a given strategy K, while simultaneously increasing the size of the anticrowds using the opposite strategy $\overline{K}$. It is remarkable that a linear increase in the "noise" q gives rise to such a non-linear variation in σ_D. As noted above, the theory neglects a full treatment of the dynamical fluctuations around n_K^{mean}. Hence, the theory overestimates the crowd–anticrowd cancellation arising in Eqn. (4.2) and thus slightly underestimates σ_D in the neighbourhood of $C_{\text{crit}}(q, p)$ [compare Figs. 4.3(a) and 4.3(b)]. As p in-

creases, $C_{\text{crit}}(q,p)$ becomes less dependent on the connectivity p since more and more agents join the same network cluster. For $p \gtrsim 0.05$ the system passes the percolation threshold and hence is dominated by a giant, common cluster.

4.5 Summary

We have discussed the dynamical behaviour of a network–based, competitive multi–agent system in which corrupted information gets shared between connected agents. In particular, we focused on the regime of small memory, i.e. the case of small m, in order to see whether the Eulerian trail quasi–attractor (which emerges at $q = 0$, $p = 0$) would survive the effects of inter–agent connections and data–corruption (i.e. non–zero p and q). As expected at ($q = 0$, $p = 0$), σ_D is smaller for large m than for small m because the typical crowd (anticrowd) sizes decrease (increase) as m increases. The regime $(q = 0, p \neq 0)$ is discussed in Ref. [7] for general m, while the regime $(q \neq 0, p \neq 0)$ will be similar to the present results for sufficiently large p. In all cases discussed, a theoretical analysis based on the *Crowd–Anticrowd* formalism was presented, and excellent agreement was demonstrated with the numerical simulations.

Bibliography

[1] D. S. Callaway, M. E. J. Newman, S. H. Strogatz, and D. J. Watts, Phys. Rev. Lett. **85**, 5468 (2000).

[2] R. Albert and A.L. Barabasi, Phys. Rev. Lett. **85**, 5234 (2000).

[3] M. Anghel, Z. Toroczkai, K.E. Bassler, G. Korniss, Phys. Rev. Lett. **92**, 058701 (2004).

[4] I. Caridi, H. Ceva, cond-mat/0401372 (2004).

[5] M. Sysi-Aho, A. Chakraborti, and K. Kaski, Physica A **322**, 701 (2003).

[6] D. Challet, M. Marsili and G. Ottino, preprint cond-mat/0306445 (2003).

[7] S. Gourley, S.C. Choe, N.F. Johnson and P.M. Hui, Europhys. Lett. **67**(6), pp. 867-873, (2004); e-print cond-mat/0401527.

[8] N.F. Johnson and P.M. Hui, preprint cond-mat/0306516 (2003).

[9] N.F. Johnson, S.C. Choe, S. Gourley, T. Jarrett, P.M. Hui, *Advances in Solid State Physics*, **44**, 427-438 (Springer Verlag, Germany, 2004).

[10] M. Hart, P. Jefferies, N. F. Johnson, P. M. Hui, Physica A **298**, 537 (2001).

[11] A. Cavagna, J. P. Garrahan, I. Giardina, and D. Sherrington, Phys. Rev. Lett. **83**, 4429 (1999).

[12] M. Hart, P. Jefferies, N. F. Johnson, P. M. Hui, Phys. Rev. E **63**, 017102 (2000).

[13] Defining $q = (1/2)[1-\tanh(1/T)]$ [11, 12], one could choose to convert the parameter q into a 'physical' temperature T which creates disorder in the information carried by the 'bonds' (as opposed to the 'sites' in the TMG [11, 12]). However, since T must be positive to be physical, this transformation would restrict q to the range $0 \leq q \leq 1/2$, thereby discarding the interesting high q behaviour.

[14] D. Challet, Y. C. Zhang, Physica A **246**, 407 (1997).

[15] D. Challet, M. Marsili, and R. Zecchina, Phys. Rev. Lett. **84**, 1824 (2000).

[16] R. Savit, R. Manuca, and R. Riolo, Phys. Rev. Lett. **82**, 2203 (1999).

[17] N. F. Johnson, P. M. Hui, R. Jonson, and T. S. Lo, Phys. Rev. Lett. **82**, 3360 (1999).

[18] S. Hod and E. Nakar, Phys. Rev. Lett. **88**, 238702 (2002).

[19] The Eulerian Trail corresponds to a particular cycle around the global information states, of duration $2P = 2 \cdot 2^m$ timesteps, in which every possible transition between global information states is visited once. For $m = 1$ it is given by $\ldots 00110011 \ldots$. See P. Jefferies, M.L. Hart and N.F. Johnson, Phys. Rev. E **65**, 016105 (2002).

Part II

Cancer:
A Real–World Network–Based Complex System

Chapter 5

A Brief Overview of Existing Avascular Cancer Models

5.1 Introduction

The World Health Organization (WHO) estimates cancer to be one of the leading causes of death, with 7.6 million people out of 58 million deaths worldwide attributed to cancer in 2005. Perhaps more disturbingly they state that "... many of these deaths can be avoided. Over 40% of all cancers can be prevented. Others can be detected early, treated and cured." [1]

Persistent and dedicated effort by the research community, especially in the wake of new techniques and accompanying technological advances, has led to a huge surge of discoveries, a wealth of data and most importantly a deeper understanding of cancer. However, the modelling community has only relatively recently entered the fight against cancer. As Gatenby and Maini accurately voice, "...clinical oncologists and tumour biologists lack a comprehensive theoretical framework for understanding, organizing and applying these data, and further highlight the necessity to develop models that provide real insights into critical parameters that control system dynamics." [2]

5.2 Cancer properties

The inevasible proliferation of cancer arises through one or more mutations in a cell, bestowing it with selective growth advantages. However, tumorigenesis – the formation of new tumours – requires successive genetic mutations to be acquired by the clonal cancer cells to garner abilities including self-sufficiency in growth signals, insensitivity to growth–inhibitory signals, evasion of programmed cell death (apoptosis), limitless replicative potential, sustained angiogenesis, and tissue invasion and metastasis [3, 4].

These somatic mutations occur in all dividing cells and may result from faulty DNA replication or exposure to exogenous or endogenous mutagens. It is thought that there exist 'cancer genes' which are susceptible to cancerous mutation, and are generally classified into three categories: gatekeepers, caretakers and landscapers [5]. Gatekeepers comprise oncogenes and tumour suppressor genes which directly regulate growth and differentiation pathways of the cell. Caretakers maintain the genomic integrity of the cell. Hence, any mutation to these genes can lead to genetic instability and indirectly to changes in other genes controlling the cell. Finally, mutation to landscapers could initiate disadvantageous environments contributing indirectly to neoplastic transformation of cells [3, 5, 6]. Alternatively, cancer genomes can be categorised into two more broad biological classes of somatic mutation. 'Driver' mutations are directly involved in cancer development and are therefore positively selected. On the other hand, 'passenger' mutations are not subject to selection, but are present in the progenitor cell responsible for cancerous expansion. They do not confer growth advantages [7]. Alarmingly, Greenman *et al.* [7] and Sjöblom *et al.* [8] recently reported a far higher number of somatic mutations than previously identified. Greenman *et al.* report 1000 somatic mutations of which most are thought to be

'passenger' mutations. However, the authors present evidence for 'driver' mutations contributing to the development of the cancer studied in approximately 120 genes [7].

In addition to clonal selection causing cancers to evolve, it is widely accepted that cancers highly dependent on the competition for space and nutrients [4, 9, 10]. Tumour cells generate many of their own growth signals, and monitor their external environment. On the basis of sensed signals, cells decide whether to proliferate, to be quiescent, or to enter into a post–mitotic state. The oxygen and nutrients supplied by the vasculature are crucial for cell function and survival. Folkman [11] and Carlsson *et al.* [12] observed that tumour cells at a distance of more than about 100μm from capillaries are transferred into the state of necrosis due to the lack of oxygen and nutrient's supply. In avascular tumours, such as in *in vitro* tumour spheroid experiments, it was shown that tumours grow to a critical size and stop, as they are incapable of angiogenesis. The size is determined by the balance between cell proliferation and the cell death inside the spheroid [13, 14]. In order to progress to a larger size, neoplasias must develop angiogenic ability [11]. The onset of angiogenesis leads to the vascular phase of cancer growth. As the tumour progresses further, sooner or later during the development of most types of human cancer, primary tumour masses spawn pioneer cells that move out, invade adjacent tissues, and thence travel to distant sites where they may succeed in founding new colonies. The capability for invasion and metastasis enables cancer cells to escape the primary tumour mass and colonize new terrain in the body where, at least initially, nutrients and space are not limiting. This is the last and most lethal phase of cancer growth [4, 10].

Nevertheless, despite the clonal complexities involved, most cancers have a well defined structure. Due to the high nutrient dependence outlined above, tumours typically consist of three regions, as shown in Fig. 5.1. The innermost region is a

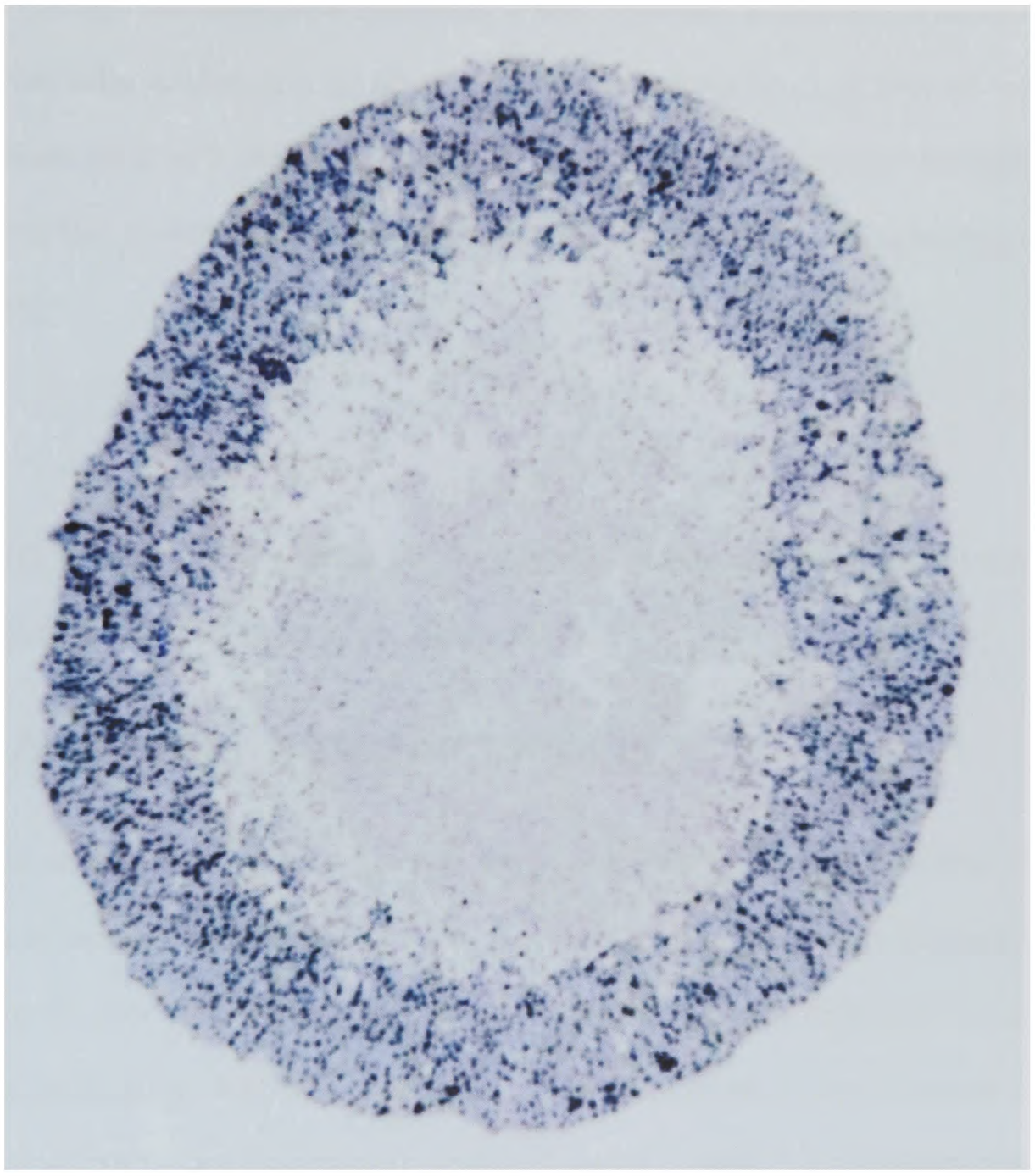

Figure 5.1: Layers of a tumour spheroid. Central section of spheroid of 1415μm diameter after 18 days in culture demonstrating proliferating ring of cells surrounding an extensive necrotic centre. A quiescent layer between the two layers is also visible. (Image reproduced from Sutherland *et al.* [15]. Permission from author pending.)

necrotic core where the low or no nutrient levels cannot support cell survival and hence lead to cell death (apoptosis). The necrotic core is followed by an inactive or quiescent region, where the intermediate nutrient level environment prompts tumour cells to conserve energy and stay in a quiescent state. Finally, a nutrient rich environment unleashes a fully active cancer characterized by a proliferating ring of cancer cells [15]. Further to a well defined pattern, extensive experimental results subsequently have shown the growth of cancer could be accurately fitted by a Gompertzian relation [16, 17, 18]:

$$V(t) = \left[\frac{V_0}{K}\right]^{\exp(-rt)} K \tag{5.1}$$

where $V(t)$ is the tumour volume at time t, V_0 is the initial size of the tumour, K is the equilibrium size, and r is a positive constant.

5.3 Avascular tumour models

The literature on tumour modelling is vast, and a comprehensive review of the full spectrum of models exploring avascular, vascular, angiogenic and metastatic tumours, in addition to models exploring drug treatment and delivery response, is outside the scope of this chapter. Instead, the aim is to give a brief overview of recent models of tumours that exhibit no new tumour–induced vessel growth (i.e. angiogenesis). These tumours present the simplest system to model and understand the principles driving tumour growth, whilst sharing many of the phenomena exhibited by vascularizing tumours. More precisely, this overview includes models of avascular tumours, and models which assume an already fully vascularized system, yet no tumour–induced neoangiogenesis such as by Patel *et al.* [73] and the model presented in Chapter 6. Avascular tumours are easily and cheaply grown *in vitro*, such as in tumour

spheroid assays [19, 20], amounting to a vast reproducible data set, far exceeding the less controllable and parametrically numerous environment of *in vivo* experiments. Similarly, including the already fully vascularized tumours in the same category is not an unreasonable assumption. It has been observed, for example in non–small–cell lung carcinoma [21] and in rat C6 gliomas [22], that sustained avascular tumour growth is possible through means of native microvessel network cooption [22] and vasculogenic mimicry [23]. Hence, any model of pre–neoangiogenic, or avascular, tumours provides an advantageous environment for development, as well as a solid foundation for more complicated, and possibly biologically more accurate, extensions.

Most models can be broadly placed into one of two categories, with a new generation of hybrid models gaining popularity. The first set of models are discrete cell models, usually of length scale order of an individual cell. The cell–cell and cell–environment interactions are mimicked by the rules implemented most popularly in cellular automata, although other computer simulation based models using lattice Boltzmann methods, Potts model, stochastic Markov chain equations and agent–based models exist also. The second category of models consist of continuum models. These are mathematical formulations relating the various components and interactions of the system, whilst using some space averaging, hence typically consisting of a set of coupled differential equations or partial differential equations. They explore multicellular patterns emerging from the dynamic evolution of continuum population density functions and their interactions with the environment.

As previously mentioned, the literature is vast, and hence this overview has been limited to the most prominent and influential discrete tumour models, with only a brief introduction to continuum models. Good reviews on continuum cancer models exist, and we refer the reader to Refs. [24, 25, 26] for these more detailed and

comprehensive reviews.

5.4 Continuum models

Mathematical models of tumour growth typically consider the interactions between the continuum cell populations (i.e., partial differential equations of cell population densities) governed by mass conservation principles and the reaction–diffusion equations of growth influencing chemical species such as nutrients, growth promoting factors and cytotoxic drugs. More specifically, the models aim to describe and relate the intricacies of tumour cell cycles and dynamics with the production, diffusion and absorption of various chemical species, hoping to shed light on the growth behaviour of the tumour as a whole.

Early mathematical models focussed on understanding nutrient–limited tumour growth [27, 28, 29, 30, 31, 32]. These tumour models are simplistic, assuming a constant density, single tumour cell type population. Hence, the reaction–difusion equations governing the chemical species profiles inside the tumour, are coupled to the differential equations describing the tumour's volumetric growth rate, which is a function of the cell proliferation rate. Despite the simplicity, these models are very successful in capturing the qualitative growth pattern of *in vitro* spheroids. The cultured tumour spheroids consist of three distinct layers: a nutrient–lacking central necrotic core, an intermediate nutrient–poor layer of quiescent cells, and a highly active, nutrient–rich proliferating ring of cancer cells as depicted in Fig. 5.1 [19, 33, 36].

Later mathematical tumour models were driven by more and more realistic features present in tumours *in vivo*. These properties, including for example, blood vasculature, multiple nutrients [49], tissue composition, extracellular matrix (ECM),

micro–environmental influences and immune system responses, add to the heterogeneous nature of real tumours, compared to the relatively homogeneous, controlled *in vitro* spheroid environments.

Initially, details of cell movement driven by pressure gradients were considered [37, 38]. With the formation of a necrotic core, the centre of the tumour becomes less dense, causing movement of highly active cells from the proliferating ring towards the centre of the tumour. Such pressure driven movement necessitates the consideration of the tumour's mechanical properties, employing Darcy's law and other constitutive equations to relate tumour cell velocity to pressure. These models also introduced cell–cell adhesion [38] and surface tension [37] to ensure compactness of the tumour. More and more complex models of cell movement have since been proposed, ranging from convective [39, 43], to diffusive [40, 41] to chemotactic [42] driven movement, where some of the authors considering diffusive cell movement model the invasion of tumours into the neighbouring tissue using travelling wave solutions [40, 41, 42].

Many of the most recent mathematical continuum models are sophisticated multi–phase models [45, 46, 47, 48], considering how the mechanical interactions between tumour cells influence tumour growth. In particular, most models assume a fluid–like flow of tumour tissue through the porous–like extracellular matrix medium, whilst employing some bulk constitutive relation between stress and strain, such as Darcy's law or simplified Navier–Stokes equations, averaged over many cells. Importantly, work done by Helmlinger *et al.* [44] provides experimental support that mechanical effects influence on tumour growth. They found that tumour spheroids grown in gels with varying stiffness resulted in different sized spheroids. Specifically, increasing gel stiffness resulted in smaller tumour spheroids.

Continuum models have been important in advancing the understanding of tumour

growth phenomena. Furthermore, they provide a vital framework in which to test hypothesis and make predictions. Perhaps most illustrating is the work by Gatenby *et al.* [34] in which the authors predict that the anaerobic metabolism of cancer cells gives rise to an acidic environment, creating an interstitial gap at the tumour–host interface. This was subsequently observed experimentally.

5.5 Discrete models

A popular technique for discrete modelling are cellular automata (CA) [50]. They have been used extensively to model and analyze a wide range of complex systems, and perhaps most notably, biological systems [50, 51]. The application of cellular automata to model many aspects of tumour growth, albeit in a much more "agent"–like manner than original cellular automata, have been very fruitful.

Typically, in this modelling technique for tumours, each unit of a cellular automaton corresponds to a single cell of the tumour. The practical advantage lies in the flexibility and ability to model the heterogeneity inherent in tumours, such as vasculature structure and differences in cell behaviour due to cell type. Each automaton unit can easily represent any type of cell (e.g., normal cell, endothelial cell, and cancer cells of varying mutation advance) or simply empty space. Each type of cell is usually assumed to have some pre–defined characteristic behaviour intended to mimic the real biological behaviour of the particular cell type. These characteristics are generally in the form of rules and conditions. Hence, the cell–cycle process can be represented by different simplified cytokinetic models specific for each cell type. Most simply one could define a look up table of cell state, depending on the conditions of the local micro–environment such as nutrients and other chemical factors. Hence, these dictate the action and abilities of cells, such as proliferation and invasion, and the

state of the cell such as active, quiescent or dying. Similar approximating rules are usually defined that govern the movement to, and interaction with, its surrounding, as well as the cell–cell interactions. Although laws governing the accurate mechanical interactions could be modelled, the shear number of cells would make this impractical due to computational limitations and extreme expense. Cell movement is typically probabilistic determined by factors including availability of space, pressure gradients, nutrient concentration gradients, and other weights due to chemotactic gradients. The final modelling aspect is the representation of space. Most cellular automaton models discretize space into a fixed regular square lattice, as this is the most simple and fast computationally. However, others have opted to use Voronoi tessellation [52, 53, 64, 65, 66] to divide space into cells to allow for greater flexibility.

5.5.1 Cellular automaton models

5.5.1.1 Early models

One of the earliest discrete tumour growth models is by Düchting and Vogelsaenger [54, 55, 56]. Their model system considers an homogeneous tissue segment of about 1mm^3 in volume, or equivalently approximately $10^4 - 10^5$ cells. Each site of their cellular automaton corresponds to a single cell or vacant space. Normal and cancer cells are modelled using block diagrams developed to describe the cell–cycle process, where the phase duration of the cell–cycles are taken from experimental data. Nutrient diffusion is not incorporated directly. Rather, it is assumed that normal cells have a finite life span, whilst only being able to proliferate if space permits. For cancer cells, on the other hand, it is assumed that if a proliferating cancer cell is more than 100μm away from a capillary, it will switch into a G_0 resting state of the cell–cyle, before becoming necrotic after some transit time. However, if new capillaries form within the required distance, the cancer cell can come out of its quiescent state.

Hence, the model system contains a static capillary network with idealized structure. As the authors point out, influences of metastasis, side effects, immunologic reactions and drug resistance are neglected. Furthermore, environmental variables, mechanical confinement and toxic metabolites are also omitted. Despite the minimalist approach, several virtual treatments are performed on the model tumour including surgery (removal of half of tissue segment), radiation therapy (all cells irreversibly damaged with 50% probability) and chemotherapy (destruction of all proliferating tumour cells).

Another early minimal model is by Qi *et al.* [57]. The authors combine the proliferation of cancer cells with several reaction processes to mimic the cell–mediated immune response. In particular, they describe the reactions between cancer cells, dead cancer cells, effector (cytotoxic) cells and the complexes produced by the cytotoxic process. Most of the reaction probabilities are gathered from experiments. To incorporate mechanical pressure inside the tumour, the proliferation of cancer cells, or more specifically, the direction of placement of the resulting daughter cell, is determined by a critical cancer density, below which cancer cells can only move to a neighbouring site towards the centre. Above the critical density cancer cells are allowed to move to any neighbouring site randomly. The authors proceed to compare the simulation growth curves to experimental data from spontaneous carcinoma C3H and spontaneous KHT in mice. A Gompertzian growth relation is assumed for the experimental growth, and when plotted with the experimentally collected parameter values, show good agreement with the model results.

Smolle *et al.* also propose a simple cellular automaton model [58, 59, 60, 61] for tumour growth and invasion. The authors investigate the resulting morphological tumour patterns as a function of cell division, cell death, and cell migration. Invasive patterns generated from the simulations are compared statistically with experimental

results in order to detect real invasive pattern. In addition to invasion, the influence of paracrine (stroma) and autocrine (tumour) stimulation on the various preset cell behaviour is explored. These additional stimuli are assumed to be local factors whose concentration is calculated by counting the number of source sites within a "distance of influence".

5.5.1.2 Recent models

Scalerandi *et al.* developed a model which focuses on the effects of nutrient availability and subsequent consumption by the cells on the morphology and growth rates of cancer growth [62]. A set of rules are defined governing the cell–cell interactions and the competition for nutrients. More interestingly, the authors formulate a set of iteration equations, for the number of cancer cells in each site, and the diffusion of cancer cells between sites of their square lattice, whilst also introducing iteration equations for the nutrient supply and nutrient consumption by the cells in each site. The work was later extended by Delsanto *et al.* to explore "phase transitions" of the tumour evolution from regression, to latency, to metastasis and finally to unlimited growth [63] as a function of nutrient supply and the acquisition of these nutrients by the cancer cells. They show that small variations in the parameter space can lead to these distinct phases, and briefly simulate possible therapeutical strategies aimed to reduce a growing tumour to dormancy.

Kansal *et al.* move away from the rigidity of a regular lattice and instead use as an underlying lattice the Delaunay triangulation, which is the dual lattice of the Voronoi tessellation [64, 65, 66]. This choice of lattice is isotropic in space and uses an adaptive grid, allowing greater resolution at small tumour sizes and growth to larger sizes than usually possible using a regular lattice. In particular, the density of a site of the lattice is allowed to vary continuously with radial position, with lattice

sites nearer the centre typically consisting of 10^3 cells, whereas the outermost lattice cells make up about 10^6 cells. Hence, there is higher resolution closer to the centre. The state and action of a cell, which is taken to be dependent on nutrient supply and mechanical effects, is not directly modelled, but rather are functions of the distance from the tumour surface. A rim of certain thickness from the tumour edge has a high enough nutrient concentration to maintain active proliferation. Hence, cell division can only take place if within a certain distance, which scales as $R_t^{\frac{2}{3}}$, where R_t is the tumour radius. An additional criterion mimicking mechanical pressure is imposed on proliferation, where the probability of proliferation is reduced with increasing radial distance. Similarly, cells a certain distance from the boundary become necrotic. The authors produce three–dimensional structures with different clonal tumour sub–populations, and compare the simulation results to untreated glioblastoma multiforme (GBM) tumours and showed good agreement in radii, cell number, layers fractions and volumetric doubling time.

Anderson *et al.* [68] take a different approach to the previous models, by deriving a discrete model from a discretized form of the partial differential equations developed in their continuum model of tumour invasion [69]. By using a standard finite–difference method, they discretize the coupled partial differential equations governing the interactions of the tumour cells, extracellular matrix (ECM) and matrix degrading enzymes (MDE), in addition to generating the movement probabilities of each cell in response to its interactions with the matrix macromolecules in its micro–environment. Although the system is a 200×200 size grid, the number of cells is limited to 3000 for computational reasons. Interestingly, the authors find that the discrete simulations differ from the continuum model, in that cells in the discrete model are able to migrate farther than predicted in the continuous model, with aid

from the ECM structure and potentially disastrous implications for metastasis.

5.5.2 Agent–based model

Mansury *et al.* introduce an agent–based model, in which cells search globally and locally, able to "learn" and process the gathered information to determine the energy expenditure needed, and hence the next migratory behavioural step. This concept is inspired by cell–surface receptors which enable tumour cells to sense chemical gradients and trigger changes responsible for directed motion along these gradients [70, 71, 72]. First, a cell performs a global search, which is assumed to be solely represented by mechanical confinement due to environmental (mechanical) resistance to migration. Once this global search is performed, the cell does a more precise local search, processing complete information on its local micro–environment including nutrient level, toxicity, and mechanical confinement. The authors explore the search precision and find that if cells have dominant global search, the result is a small number of large tumour clusters with rapid expansion, but shorter lifespan. On the other hand, cells with dominant local search results in many small clusters with longer lifespan but much slower expansion velocity. The authors then further investigate the notion of a structure–function relationship between fractal dimensions of the tumour surface and average velocity of the tumour's spatial expansion. They show that migratory cell behaviour is largely responsible for the emergence of branching patterns with higher fractal dimensions, whereas cell proliferation is becoming increasingly active at lower fracticality associated with lesser deterioration of mechanical confinement.

5.5.3 Hybrid models

Hybrid models aim to combine the discrete composition of cells with the continuous nature of concentration levels of nutrients and other chemical species. These models

typically employ cellular automaton rules for the behaviour and interaction of cells, whist numerically solving nutrient diffusion equations for the lattice.

A simple model by Deutsch *et al.* aims to verify the growth behaviour of tumour spheroids by considering diffusible signals emitted by necrotic cancer cells, to create a gradient for active cells from the proliferating ring to migrate inwards. They verify the well established layer structure of spheroid tumours shown in Fig. 5.1 as well the initial growth spurt, followed by a significant decrease in growth rate [74].

Sander *et al.* look at *in vitro* brain tumours where the invasive cells are thought to exhibit very little proliferation, but nevertheless produce complex growth patterns on the tumour's surface with tenuous branches formed by invading cells [67]. Similar to the modelling approach by Anderson *et al.* [68], the authors of this paper start by formulating a continuum model, and subsequently present a complementary discrete model. In both models, the motion of cancer cells is determined by two processes. First, heterotype chemotaxis caused by nutrient concentrations. Second, homotype chemotaxis is introduced where cancer cells secrete paracrine to attract each other. As an indirect consequence of the latter, invading cells may cause tissue damage creating pathways for other cells to follow in. This was observed experimentally by one of the authors. The nutrient concentration, assumed to be glucose and a continuous variable, is taken to be distributed by simple diffusion without replenishment, and is calculated numerically on the lattice for the discrete model. Using estimates for the model parameter values from experimental data, the authors conclude that it takes strong chemotaxis to generate an invasive zone. However, within the estimated parameter value range they fail to reproduce the branches of invasion. Much larger values need to be considered in order to produce the branches, indicating that chemical triggers other than glucose might be involved.

Patel *et al.* study the qualitative relationship between both micro–environmental acidification by active tumour cells and native tissue vascularity on the growth of and invasion efficacy of pre–neoangiogenic tumours [73]. In particular, this hybrid model serves as an early growth complement to work done by Gatenby *et al.* [34], in which a continuum model of acid–mediated tumour invasion predicts a tumour–host interstitial gap. However, the continuous model was only feasibly useful for tumour sizes of approximately > 0.1cm in diameter. Similar to other hybrid models, the authors describe the cellular interactions using a cellular automaton incorporating normal cells, tumour cells, necrotic and empty space. The hydrogen ion (cause for acidification due to tumour anaerobic metabolism) and glucose (nutrient) fields obey partial differential equations. Furthermore, the model includes a random microvascular network from which metabolic substrate is delivered and metabolites removed. The discrete, early tumour growth simulations confirm the result from the continuum model [34], that a hypocellular gap at the tumour–host interface is formed. Further, the automaton model reproduced many of the known characteristic tumour morphologies, due to specific tumour hydrogen ion and vascularity combinations. Interestingly, for every hydrogen ion production rate there exists a range of optimal microvessel densities leading to favourable pH for cancer cells to survive. In addition, a sharp transition from tumour confinement to invasiveness is observed when hydrogen ion production reaches a critical value.

Alarcón *et al.* consider the effects of blood flow on heterogeneity of the environment and consequently on tumour growth behaviour [75]. In particular, changes to the oxygen distribution via a native vascular network are investigated. This initially uniform network is influenced by blood and haematocrit flow. Vascular structural adaptation occurs in response to mechanical or hemodynamic stimuli, as well as

metabolic demands of the surrounding tissue. In addition, complex rheology and red blood cell circulation are also considered. Following oxygen distribution, the vascular structure is assumed to be fixed, and the discrete cellular dynamics are investigated. The authors show that if oxygen is distributed uniformly through the vasculature, the tumour grows as a compact mass, expanding radially outwards, forming a relatively isotropic growth. By contrast, when oxygen is distributed heterogeneously through the vasculature, the tumour's growth is localized in regions of high oxygen concentration. Furthermore, the tumour reaches a finite size since the limited nutrient supply can only sustain a finite population, whilst the other nutrient deficient regions die.

5.6 Summary

The different approaches to cancer modelling are not exclusive, but rather complementary to each other. They reveal and provide information about, as well as being able to utilize information from, cancer growth at different length scales.

Discrete models offer three main advantages over continuum approaches. First, advances in imaging techniques have enabled the ability to track spatial and temporal movements of individual cells. However, despite these astounding leaps in technology, conventional clinical imaging techniques can only detect tumours larger than a critical size of a few millimetres in diameter. Therefore, it is essential to consider the discrete nature of the cell-system to better understand the early stages of tumour growth. Due to the relatively small number of cells involved in early growth, a continuum model would be inappropriate, especially as early growth is highly dependent on the path history of each individual cell. Second, cancer cell heterogeneity and the local cell-cell interactions could lead to non-trivial collective behaviour resulting in large-scale multicellular patterns. Hence, being able to understand the cancer cell

systems at different length scales is imperative. Third, in tumours where the system is inherently discrete, it is important to be able to model it as such, not just in space, but also in time. Space is highly heterogeneous due to nutrient levels and tissue consistency for example, implying that there should be competition amongst cells to be in a preferred location. Furthermore, discretizing time allows the model to be 'fast–forwarded' without needing to analytically/numerically solve the underlying equations such as in continuum models.

Both discrete and continuum models suffer from various drawbacks. First, any theoretical approach requires parameterization. These values must be collected experimentally. Such data is often not available, but more problematically, differs from experiment to experiment. Hence, combining values gathered from various experiments might not be suitable, requiring exhaustive verification of model results for robustness spanning the model parameter space. This emphasizes the importance of a minimal model, capable of exhibiting the properties of real tumours, whilst being computationally inexpensive. Second, any translation of real system set–up to a theoretical model is a highly non-trivial task. One must find and choose the parameters of importance, whilst minimizing the number of such in order to avoid the problem of parameterization. Meanwhile, stripping the real system excessively could lead to oversimplification, possibly rendering the model intractable. However, the process of finding a minimal model with the key components, with easy parameterization, whilst reproducing the experimental results, is by itself part of the research and model development.

This chapter gave a brief overview of the vast number of models that have been proposed to date, setting a benchmark for new models. With these and the advantages for choosing a discrete model in mind, we present a simple, multi–scale model of

tumour growth in chapter 7.

Bibliography

[1] http://www.who.int/cancer/en/

[2] Gatenby, R.A., Maini, P.K. Cancer summed up. *Nature* **421**, p. 321 (2003).

[3] Michor, F., Iwasa, Y., Nowak, M.A. Dynamics of cancer progression. *Nature Rev. Cancer* **4**, pp. 197–205 (2004).

[4] Hanahan, D., Weinberg, R.A. The hallmarks of cancer. *Cell* **100**, pp. 57–70 (2000).

[5] Kinzler, K.W., Vogelstein, B. Gatekeepers and caretakers. *Nature* **386**, pp. 761–763 (1997).

[6] Sieber, O.M., Heinimann, K., Tomlinson, I.P. Genomic instability - the engine of tumorigenesis? *Nature Rev. Cancer* **3**, pp. 701–708 (2003).

[7] Greenman, C., *et al.* Patterns of somatic mutation in human cancer genomes. *Nature* **446**, pp. 153–158 (2007).

[8] Sjöblom, T., *et al.* The consensus coding sequences of human breast and colorectal cancers. *Science* **314**, pp. 268–274 (2006).

[9] Nowell, P.C. The clonal evolution of tumor cell populations. *Science* **194**, pp. 23-28 (1976).

[10] Anderson, A.R.A., Weaver, A.M., Cummings, P.T., Quaranta, V. Tumour morphology and phenotypic evolution driven by selective pressure from the microenvironment. *Cell* **127**, pp. 905-915 (2006).

[11] Folkman, J. Tumour angiogenesis: therapeutic implications. *N. Engl. J. Med.* **285**, pp. 1182–1186 (1971).

[12] Carlsson, J. *et al.* Formation and growth of multicellular spheroids of human origin. *Int. J. Cancer* **31**, pp. 523–533 (1983).

[13] Dorie, M. J., Kallman, R. F., Rapacchietta, D. F., van Antwerp, D., Huang, Y. R. Migration and internalization of cells and polystrene microspheres in tumor cell spheroids. *Exp. Cell Res.* **141**, pp. 201–209 (1982).

[14] Dorie, M. J., Kallman, R. F., Coyne, M. A. Effect of cytochalasin B, nocodazole and irradiation on migration and internalization of cells and microspheres in tumor cell spheroids. *Exp. Cell Res.* **166**, pp. 370–378 (1986).

[15] Sutherland, R.M., *et al.* Oxygenation and differentiation in multicellular spheroids of human colon carcinoma. *Cancer Res.* **46**, pp. 5320–5329 (1986).

[16] Laird, A. K. Dynamics of tumor growth. *Br. J. Cancer* **18**, pp. 490–502 (1964).

[17] Steel, G.G. Growth kinetics of tumors. *Clarendon Press*, Oxford (1977).

[18] Brunton, G.F., Wheldon, T.E. Prediction of the complete growth pattern of human multiple myeloma from restricted initial measurements. *Cell Tissue Kinet.* **10**, pp. 591–594 (1977)

[19] Sutherland, R.M. Cell and environment interactions in tumour microregions: the multicell spheroidal model. *Science* **240**, pp. 177–184 (1988).

[20] Mueller-Klieser, W. Multicellular spheroids: A review on cellular aggregates in cancer research, *J. Cancer Res. Clin. Oncol.* **113**, pp. 101–122 (1987).

[21] Pezzella, F. *et al.* Non–small–cell lung carcinoma tumor growth without morphological evidence of neo–angiogenesis. *Am. J. Pathol.* **151**, pp. 1417–1423 (1999).

[22] Holash, J. *et al.* Vessel cooption, regression, and growth in tumors mediated by angiopoietins and VEGF. *Science* **284**, pp. 1994–1998 (1999).

[23] Maniotis, A.J., *et al.* Vascular channel formation by human melanoma cells *in vivo* and *in vitro*: vasculogenic mimicry. *Am. J. Pathol.* **155**, pp. 739–752 (1999).

[24] Araujo, R.P., McElwain, D.L.S. A history of the study of solid tumor growth: the contribution of mathematical modelling. *Bull. Math. Biol.*, **66**, pp. 1039–1091 (2004).

[25] Byrne, H.M., Alarcón, T., Owen, M.R., Webb, S.D., Maini, P.K. Modelling aspects of cancer dynamics: a review. *Phil. Trans. R. Soc. A* **364**, pp. 1563-1578 (2006).

[26] Roose, T., Chapman, S.J., Maini, P.K. Mathematical models of avascular tumour growth. unpublished. (2006).

[27] Burton, A.C. Rate of growth of solid tumours as a problem of diffusion. *Growth* **30**, pp. 157–176 (1966).

[28] Greenspan, H. P. Models for the growth of a solid tumour by diffusion. *Stud. Appl. Math.* **52**, pp. 317-340 (1972).

[29] McElwain, D. L. S., Ponzo, P.J. A model for the growth of a solid tumor with non–uniform oxygen consumption. *Math. Biosci.* **35**, pp. 267-279 (1977).

[30] McElwain, D. L. S., Morris, L. E. Apoptosis as a volume loss mechanism in mathematical models of solid tumour growth. *Math. Biosci.* **39**, pp. 147-157 (1978).

[31] Adam, J. A. A mathematical model of tumour growth. II. Effects of geometry and spatial uniformity on stability. *Math. Biosci.* **86**, pp. 183-211 (1987).

[32] Adam, J. A., Maggelakis, S.A. Mathematical models of tumour growth. IV. Effects of a necrotic core. *Math. Biosci.* **97**, pp. 121-136 (1989).

[33] Folkman, J., Hochberg, M. Self–regulation of growth in three–dimensions. *J. Exp. Med.* **138**, pp. 745-753 (1973).

[34] Gatenby, R.A., Gawlinski, E.T. A reaction–diffusion model of cancer invasion. *Cacner Res.* **56**, pp. 5745–5753 (1996).

[35] Byrne, H. M., Chaplain, M. A. J. Necrosis and apoptosis: distinct cell loss mechanisms in a mathematical model of avascular tumour growth? *J. Theor. Med.* **1**, pp. 223-236 (1998).

[36] Groebe, K., Mueller–Klieser, W. On the relation between size of necrosis and diameter of tumour spheroids. *Int. J. Radiat. Oncol.* **34**, pp. 395-401 (1996).

[37] Greenspan, H. P. On the growth and stability of cell cultures and solid tumours. *J. Theor. Biol.* **56**, pp. 229-242 (1976).

[38] Byrne, H. M., Chaplain, M. A. J. Modelling the role of cell-cell adhesion in the growth and development of carcinomas. *Math. Comput. Modell.* **24**, pp. 1-17 (1996).

[39] Byrne, H. M., Chaplain, M. A. J. Free boundary value problems associated with the growth and development of multicellular spheroids. *European J. Appl. Math.* **8**, pp. 639–658 (1997).

[40] Sherratt, J.A. Travelling wave solution of a mathematical model for tumor encapsulation. *SIAM J. Appl. Math.* **60**, pp. 392–407 (1999).

[41] Sherratt, J.A., Chaplain, M.A.J. A new mathematical model for avascular tumour growth. *J. Math. Biol.* **43**, pp. 291–312 (2001).

[42] Marchant, B.P., Norbury, J., Sherratt, J.A. Travelling wave solutions to a haptotaxis–dominated model of malignant invasion. *Nonlinearity* **14**, pp. 1653–1671 (2001).

[43] Ward, J.P., King, J.R. Mathematical modelling of avascular tumour growth. *IMA J. Math. Appl. Med. Biol.* **14**, pp. 36–69 (1997)

[44] Helmlinger, G., Netti, P. A., Lichtenbeld, H. C., Melder, R. J., Jain, R. K. Solid stress inhibits the growth of multicellular tumour spheroids. *Nat. Biotechnol.* **15**, pp. 778-783 (1997).

[45] Chen, C. Y., Byrne, H. M., King, J. R. The influence of growth–induced stress from the surrounding medium on the development of multicell spheroids. *J. Math. Biol.* **43**, pp. 191-220 (2001).

[46] Jackson, T. L., Byrne, H. M. A mathematical model of tumour encapsulation. *Math. Biosci.* **180**, pp. 307-328 (2002).

[47] Byrne, H. M., King, J. R., McElwain, D. L. S., Preziosi, L. A two–phase model of solid tumour growth. *Appl. Math. Lett.* **16**, pp. 567-573 (2003).

[48] Roose, T., Netti, P. A., Munn, L. L., Boucher, Y., Jain, R. K. Solid stress generated by spheroid growth estimated using a linear poroelasticity model. *Microvasc. Res.* **66**, pp. 204-212 (2003).

[49] Casciari, J.J., Sotirchos, S.V., Sutherland, R.M. Mathematical modelling of microenvironment and growth in EMT6/Ro multicellular tumour spheroids. *Cell. Prolif.* **25**, pp. 1–22 (1992).

[50] Wolfram, S. Theory and Applications of Cellular Automata. *World Scientific*, Singapore (1986).

[51] Ermentrout, G.B., Edelstein-Keshet, L. Cellular automata approaches to biological modelling. *J. Theor. Biol.* **160**, pp. 97-133 (1993).

[52] Voronoi, G. Recherches sur les parallélоèdres Primitives. *J. reine angew. Math.* **134**, pp. 198–287 (1908).

[53] Du, Q., Faber, V., Gunzburger, M. Centroidal Voronoi Tessellations: Applications and Algorithms. *SIAM Review* **41**, pp. 637–676 (1999).

[54] Düchting, W., Vogelsänger, T. Aspects of modelling and simulating tumor growth and treatment. *J Cancer Res. Clin. Oncol.* **105**, pp. 1–12 (1983).

[55] Düchting, W., Vogelsänger, T. Analysis, forecasting, and control of three-dimensional tumor growth and treatment. *J. Med. Sys.* **8**, pp. 461–475 (1984).

[56] Düchting, W., Vogelsänger, T. Recent progress in modelling and simulation of three-dimensional tumor growth and treatment. *BioSystems* **18**, pp. 79–91 (1985).

[57] Qi, A.-S., Zheng, X., Du, C.-Y., An, B.-S. A cellular automaton model of cancerous growth. *J. Theor. Biol.* **161**, pp.1–12 (1993).

[58] Smolle. J., Soyer, H. P., Smolle-Juettner, F. M., Stettner, H., Kerl, H. Computer simulation of tumour cell motility and proliferation. *Path. Res. Pract.* **186**, pp. 467–472 (1990).

[59] Smolle, J. and Grimstad, I. A. Tumor-cell motility and invasion within tumours determined by applying computer simulation to histologic patterns. *Int. J. Cancer* **50**, pp. 331–335 (1992).

[60] Smolle, J., Stettner, H. Computer simulation of tumour cell invasion by a stochastic growth model. *J. Theor. Biol.* **160**, pp. 63–72 (1993).

[61] Smolle, J., Cellular automation simulation of tumour growth–equivocal relationships between simulation parameters and morphologic pattern features. *Analytical Cell Pathology* **17**, pp. 71–82 (1998).

[62] Scalerandi, M., Romano, A., Pescarmona, G.P., Delsanto, P.P, Condat, C.A. Nutrient competition as a determinant for cancer growth. *Phys. Rev. E* **59**, pp. 2206–2217 (1999).

[63] Delsanto, P.P., Romano, A., Scalerandi, M., Pescarmona, G.P. Analysis of a "phase transition from tumor growth to latency. *Phys. Rev. E* **62**, pp. 2547–2554 (2000).

[64] Kansal, A.R., Torquato, S., Harsh IV, G.R., Chiocca, E.A., Deisboeck, T.S. Simulated brain tumour growth dynamics using a three–dimensional cellular automaton. *J. Theor. Biol.* **203**, pp. 367-382 (2000).

[65] Kansal, A.R., Torquato, S., Harsh IV, G.R., Chiocca, E.A., Deisboeck, T.S. Cellular automaton of idealized brain tumour growth dynamics. *BioSystems* **55**, pp. 119–127 (2000).

[66] Kansal, A.R., Torquato, S., Chiocca, E.A., Deisboeck, T.S. Emergence of a subpopulation in a computational model of tumour growth. *J. Theor. Biol.* **207**, pp. 431–441 (2000).

[67] Sander, L.M., Deisboeck, T.S. Growth patterns of microscopic brain tumors. *Phys. Rev. E.* **66**, 051901 (2002).

[68] Anderson, A.R.A., Chaplain, M.A.J., Newman, E.L., Steele, R.J.C., Thompson, A.M. Mathematical modelling of tumour invasion and metastasis. *Computational and Mathematical Methods in Medicine* **2**, pp. 129–154 (2000).

[69] Anderson, A.R.A, Chaplain, M.A.J. Continuous and discrete mathematical models of tumout–induced angiogenesis. *Bull. Math. Biol.* **60**, pp. 857–899 (1998).

[70] Mansury, Y., Kimura, M., Lobo, J., Deisboeck, T.S. Emerging patterns in tumor systems: simulating the dynamics of multicellular clusters with an agent-based spatial agglomeration model. *J. Theor. Biol.* **219**, pp. 343–370 (2002).

[71] Mansury, Y., Deisboeck, T.S. The impact of "search precision" in an agent–based tumor model. *J. Theor. Biol.* **224**, pp. 325–337 (2003).

[72] Mansury, Y., Deisboeck T.S. Simulating 'structure–function' patterns of malignant brain tumors. *Physica A* **331**, pp. 219–232 (2004).

[73] Patel, A.A., Gawlinsky, E.T., Lemieux, S.K., Gatenby, R.A. Cellular automaton model of early tumour growth and invasion: the effects of native tissue vascularity and increased anaerobic tumour metabolism. *J. Theor. Biol.* **213**, pp. 315-331 (2001).

[74] Deutsch, A., Dormann, S. Modelling of avascular tumour growth with a hybrid cellular automaton. *In Silico Biology* **2**, pp. 1–14 (2002).

[75] Alarcón, T., Byrne, H.M., Maini, P.K. A cellular automaton model for tumour growth in inhomogeneous environment. *J. Theor. Biol.* **225**, pp. 257–274 (2003).

Chapter 6

A Tumour Model Based on an Evolving Competitive Population Coupled to an Underlying Network

6.1 Introduction

The aim of cancer tumour models is to help understand the various factors driving cancer growth. Successful ones might even provide a faster, cheaper and less-invasive means of individually tailored prognosis, together with a safer test-bed for treatments. Cancer research as a whole, is homing in on increasingly microscopic length scales, revealing complexities ranging from the recently discovered number of driver gene mutations causing cancer [1, 2], through to specific cancer cell signalling pathways [3], all enveloped in the intricate interplay between cell-cell [4] and cell-environment interactions [5, 6].

Early tumour models were often a theoretical exercise for one (or more) of the following reasons: (1) they tended to look at spatially–averaged behaviour whilst neglecting the importance of environmental heterogeneities; (2) they were computationally too expensive due to the over–ambitious levels of detail introduced and/or the shear number of cells needed to produce any meaningful long–term behaviour; (3) they often had huge numbers of parameters, thereby making the concept of a

good fit with empirical data fairly meaningless and rendering any predictive power practically non–existent. Of course, all biological models by design are simplifications and approximations based on assumptions about the actual system – however, even the most mathematically sophisticated cancer models have traditionally been seen by clinicians as being too far removed from real patient data [7].

Very recently, some new models have indeed emerged through closer collaborations between theoreticians, biologists, oncologists and clinicians. Such necessary and successful partnership has enabled modelling to move beyond the impressive, yet insufficient, ability to reproduce 'standard' properties of growing tumours such as the emergence of a necrotic core [8], dependence on nutrients [9] or active propagating wave front [10]. More importantly, this symbiotic drive has led to novel predictions emerging from the model simulations, which were subsequently clinically verified, such as the hypocellular interstitial gap at the tumour–host interface [11], blood flow impact on tumour colony migration [12] or MBE (Molecular–beam epitaxy) growth behaviour accurately showing tumour cell migration to fill gaps in the tumour surface resulting in the predicted universal fractal exponent [13].

Arguably one of the greatest shortcoming in *all* models to date, is the lack of integration between the clinical vasculature–tumour images for a given patient and the models themselves. Most models are artificially seeded with initial conditions of cancer size, shape and density, as well as environmental parameters. This is a pity since huge advances have been made in imaging techniques, enabling increasingly accurate visualization of the problem zone in a given patient, and thereby yielding information over a wide range of length–scales, and at various time–resolutions. Yet the majority of models are simply too inflexible to be able to include such extensions, modifications or re–scaling. A direct one-to-one mapping of all cells is unfeasible, whilst

modelling the global averaged behaviour fails to describe important heterogeneities in the system, even though such heterogeneities may be particularly significant in early tumour growth. These shortcomings provide the motivation for the work in the present chapter.

6.2 A new multi–scale model coupling the tumour and vasculature systems

In this chapter we present a simple multi-scale model which recognizes two of the fundamental issues in cancer modelling: First, there are empirical uncertainties in the microscopic biological details of the tumour–vasculature system, hence we choose to describe local regions on the cellular scale by a suitably coarse–grained growth equation; second, there is now a wealth of data available from patient studies about both the tumour and the underlying vasculature *in vivo*, and so we specifically design a coupled tumour–vasculature model in order to be able to incorporate, and compare to, all such available data.

Our model is summarized by Figs. 6.1 and 6.2. We coarse grain our system by imposing a grid on a clinical image as in Fig. 6.1, where the length scale of each box is chosen to correspond to (at least) the resolution limit of the image (see Fig. 6.1). Vital information on location and density of vessels and cancerous tissue can therefore be extracted and seeded into the model as initial conditions. The uncertainty in the microscopic details such as cell mutation, cell dynamics, cell-cell and cell-environment interactions [1, 3, 4, 5], is replaced by a single growth equation to describe the collective cancer cell behaviour in each box of the imposed grid. Specifically, we assume that the cancer cells are competing with each other for space and for nutrients.

This approximation is supported by the fact that despite overwhelming micro-

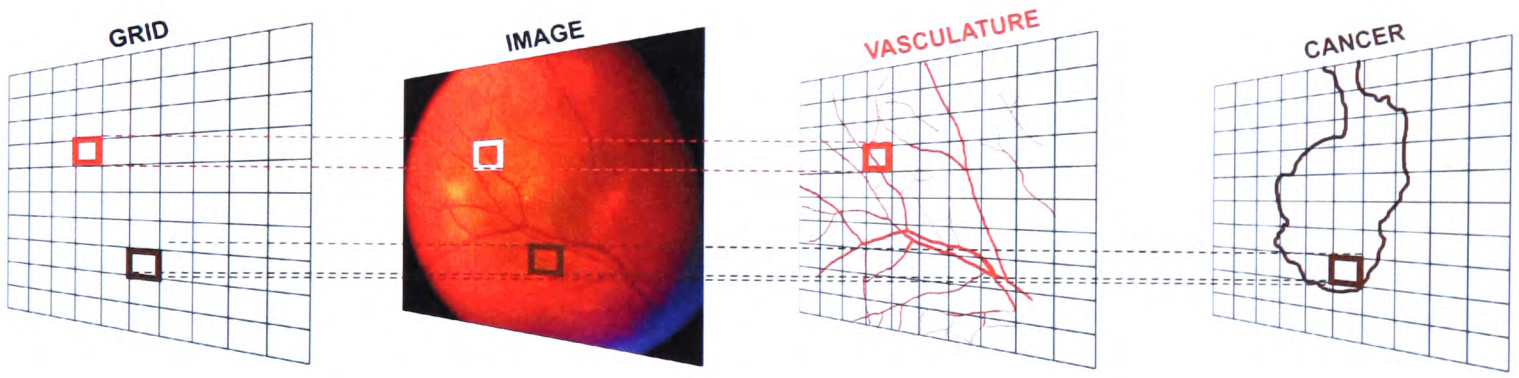

Figure 6.1: Schematic diagram of the cancer model system. The system is assumed to be coarse–grained by imposing a grid on the clinical image. The relevant data can be extracted from the image and seeded into the separate vessel and cancer layers of the model. This particular image is a fundus photo of an eye cancer (i.e. uveal melanoma) and was obtained through an ongoing collaboration with Dr. Mark Rondeau at Cornell Medical School in New York, U.S.A. Given the length–scale resolution of the uveal melanoma images used in these clinical experiments, each box of the grid is typically of approximate dimensions $100\mu\text{m} \times 100\mu\text{m}$, which corresponds to approximately 100 cells per box.

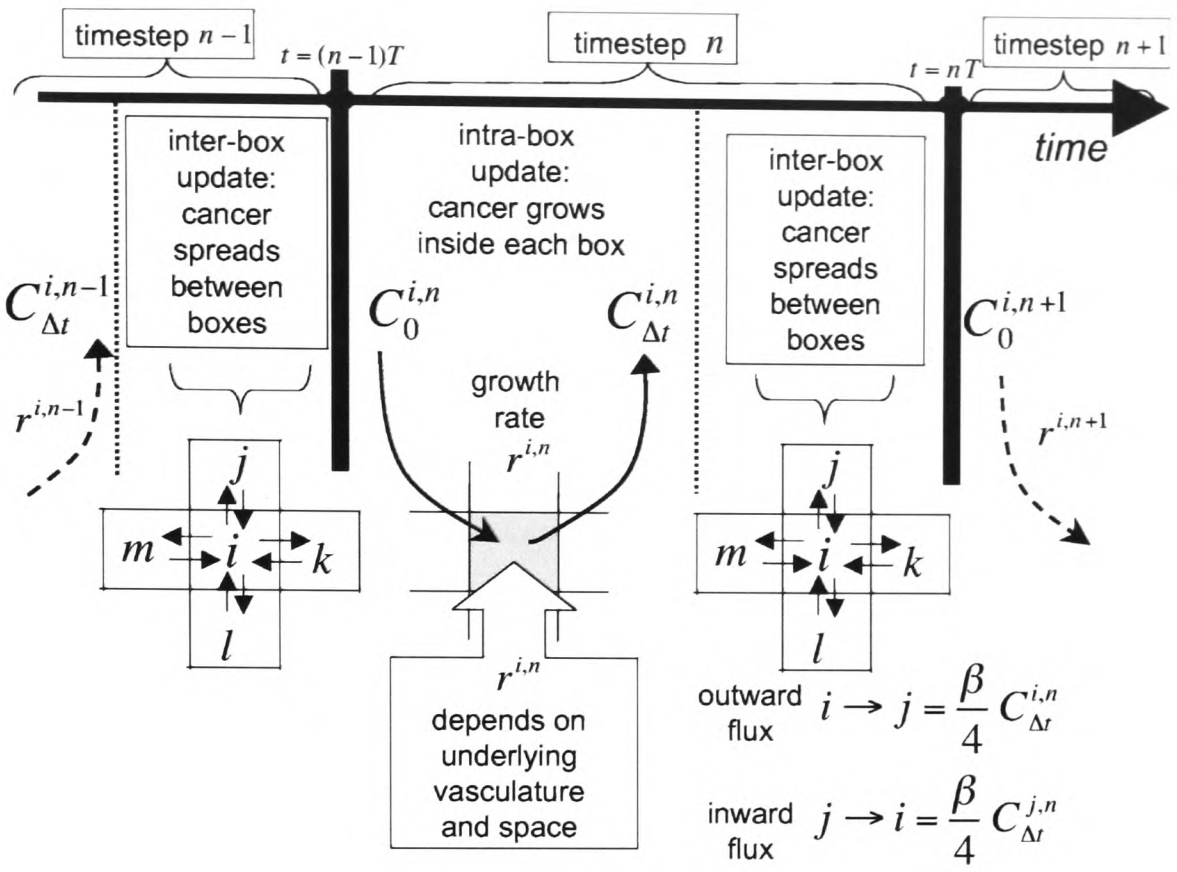

Figure 6.2: Schematic diagram of our model's temporal update within each time-step. In every time–step n each box undergoes two stages. First, intra–box cancer cell growth according to Eqn. (6.1). Second, after the growth, there is inter–box diffusion of cancer cells between neighbouring boxes resulting in a final cancer density in each box given by Eqn. (6.3). It should be noted that using the von Neumann (i.e., 4) or Moore (i.e., 8) neighbours did not significantly change the resulting shape of the tumour.

scopic complexities, the broad macroscopic behaviour of varying cancer types and quite varied *in vivo* and *in vitro* data of tumour growth curves can be accurately fitted (in a broad, averaged sense) by the logistic map or Gompertzian growth curve [14, 15, 16, 17]. We also assume a dynamical adaptation of the nutrient network depending on the cancer concentration, and vice versa.

Each box of the imposed grid may contain a mixture of normal cells and/or cancer cells and/or empty space. Time is discretized giving time–steps $n = 1, 2, 3, \ldots$ each of duration T. Within each time-step there are two updates which are performed (schematically illustrated in Fig. 6.2):

Intra-box update in which the cancer concentration changes (i.e. is updated) within each box i. This process lasts for time interval $\Delta t < T$. Due to the accurate growth description of the logistic map, the assumption is made that the growth behaviour of the cancer cell collective in each box i during timestep n is described by the self–adapting logistic map:

$$C_{\Delta t}^{i,n} = r^{i,n} C_0^{i,n} \left[1 - C_0^{i,n} \right] \tag{6.1}$$

where $C_0^{i,n}$ and $C_{\Delta t}^{i,n}$ are the cancer concentrations at the beginning and end of time interval Δt. The logistic map naturally accounts for the competition of cancer cells for space and nutrients. Specifically, limitations in space and nutrients will necessarily force adjustments to an initially exponential growth of cancer cells in each box i. Hence, the logistic map models a self–limiting process when the cancer population becomes too large and sets a maximum density in each box. The cancer growth rate at step n in each box i, is a function of the nutrient supply rate $r^{i,n}$ which is assumed to be linearly related to the vessel density present in the box. The growth rate $r^{i,n}$ during this interval is taken to be constant, but is assumed to have an update between time–steps as follows:

$$r^{i,n} = r^{i,n-1} \left[1 - \alpha C_0^{i,n} \right] \tag{6.2}$$

where $r^{i,n=0}$ is defined as the initial growth rate of cancer in aggregate cell i. Note that $r^{i,n=0}$ must not necessarily be the same for all aggregate cells i, hence the superscript i.

The vessel density and hence the nutrient supply rate is a highly dynamic variable [18]. α represents the vessel deterioration and regression over time. Specifically, cancer cells in growing tumours cause imbalances to vessel stabilizing and deterio-

rating factors, such as VEGF and angiopoietins, changing micro–environments, to make it impossible for other types of cells to exist. Furthermore, a growing tumour surrounding a vessel could exert enough pressure to squeeze the vessel shut, hence cutting off all blood supply to the region. Both effects will increase with increasing cancer density. Hence, to model these effects we have assumed the deterioration in $r^{i,n}$ to be a function of the cancer density $C^{i,n}$. It is to a first approximation taken to be a linear function of cancer density as it represents the most simple relation, but could more accurately be made a function of some non–linear cumulative cancer density average. Parameter α can be adjusted to account for changes in the intrinsic growth rate $r^{i,n}$ due to defects in cellular genetic machinery e.g. p53 gene deficient or mutated, by stimulatory growth factors such as TGFs, EGFs, angiogenic growth factors and by various cytokines. It can simultaneously reflect the effects caused by inhibitory growth factors such as TGFb, NGFs and cytokine that stimulates the immune response such as interleukins and interferons.

Inter-box update to incorporate cancer cell migration to neighbouring boxes, simple diffusion of cancer cells is assumed to take place during time $T - \Delta t$ at the end of each time–step n, where only cancer cells have mobility. Hence, the total cancer concentration in box i at time $n + 1$ is given by:

$$C_0^{i,n+1} = C_{\Delta t}^{i,n}\left[1 - \beta\right] + \frac{\beta}{8}\sum_{\{i' \neq i\}} C_{\Delta t}^{i',n} \tag{6.3}$$

where we have assumed eight nearest neighbours and an isotropic diffusion. Note that because of our choice of discretization, it follows that $C_T^{i,n} \equiv C_0^{i,n+1}$. Here, β is the ease with which cancer cells can diffuse through the extracellular matrix (ECM). Further local influences such as gradient driven chemotaxis and haptotaxis can be introduced to account for finer pattern details such as the fingering effect on the tumour surface

[19, 20]. Due to the length scale of each box typically chosen to exceed the nutrient diffusion length, there is no nutrient diffusion across box boundaries. It should be noted that we chose the self–adapting logistic map, as opposed to the continuous logistic equation, due to the fundamental discreteness of the system - the unit cell. Therefore, cancer growth (Eqn. (6.1)) and diffusion (Eqn. (6.3)) happen only when cancer concentration in box i is greater or equal to a unit cell. Furthermore, in order to ensure the results were not an artifact of the specific update rules implemented, different forms of update rules were exhaustively tested, and were found to be fairly unaffected by such changes. This was to be expected as the key element is that this model captures the interplay between the dynamic cancer growth behaviour and the vascular adaptation.

6.3 Discussion of results from the model

In this chapter we present results in 2D, although the model can easily be extended to 3D. Other than reasons for a more simple visualization and analysis, the main reason for choosing 2D is because we primarily focus on developing this model in conjunction images of uveal melanomas provided by Dr. Mark Rondeau from the Cornell Medical School. Uveal melanomas typically grow in the choroid of the eye, which is close to a 2D environment.

The general characteristics of a growing tumour are well known, and are reproduced by our model. The naturally emerging necrotic core is caused by the cancer induced deterioration of vasculature, as shown in Fig. 6.3(a). The initial build up of cancer cells in the centre of the tumour causes the vessels in the centre of the tumour to collapse first, leading to the formation of a necrotic core from the centre out. Cell cycles were not necessary to produce this emerging feature, as cell response to nutrient

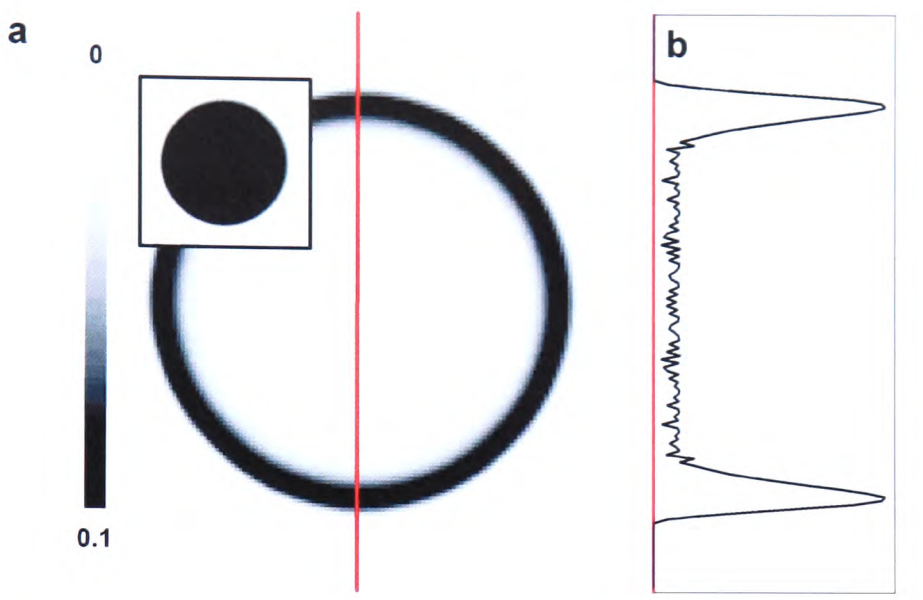

Figure 6.3: Model results verification. A typical cancer growth will show (a) a necrotic core and a highly active proliferating ring which is (b) a travelling wave. The inset in (a) demonstrates the importance of vessel vs. cancer interplay. No cell cycles are assumed. The competition implicit in the logistic map was sufficient for this property to emerge. (c) Shows the fit of the model curves to growth data gathered in tumour–bearing nude mice with A2780 cell lines (data taken from paper by Simeoni *et al.* [17]). A given cell line and controlled environment implies constant α and β terms. However, even controlled nude mice will have varying vasculature. The model curves all have fixed $\alpha = 0.0$ and $\beta = 0.55$ with varying $r = 1.3, 1.4$ and 1.55.

deficiency is implicit in the competition of the logistic map which is governed by the changing vasculature. If the effects of increasing cancer density on the vasculature are taken to be miniscule, by setting α to be small, very little vessel degradation occurs leaving the tumour core necrosis free, as shown in the inset of Fig. 6.3(a). Another vital property is a highly active proliferating ring taking the familiar shape of a propagating wave (Fig. 6.3(b)). The thickness of the ring remains fairly constant for a given environment, but changes with variations in the environment. Furthermore, a heterogeneous vasculature can lead to a non–uniform tumour shape, emphasizing the importance of heterogeneity and the interplay with the underlying vasculature (see Fig. 6.4).

Figure 6.4 illustrates how information from an image can be extracted and seeded into the model. Figure 6.4(a) is a fundus photo of the eye showing uveal melanoma growth. The visible vasculature is extracted, as shown in Fig. 6.4(b) and seeded into the model. As the initial location of tumour growth was unknown, a single box of the model was seeded with $C^{i,n=0} = 0.5$ in a vessel rich environment, as this probably represents the most likely origin of the tumour. The seed location is depicted by a brown dot within the dotted yellow circle in Fig. 6.4(b). Figures 6.4(c) and 6.4(d) compare the approximate shape of the real tumour and that of the model. The approximate growth pattern similarity, and especially the added accelerated growth along vessels, is encouraging. However, it should be noted that this comparison serves for illustration purposes only. The discrepancy is due to either unknown/incomplete information, or factors that have not yet been incorporated into the model. First and foremost, the extracted vessels (Fig. 6.4(b)) are in a layer above the tumour and do not feed the tumour directly. The vessels that directly feed the tumour are different in size and structure to the ones shown. However, the larger vessels of the overlying

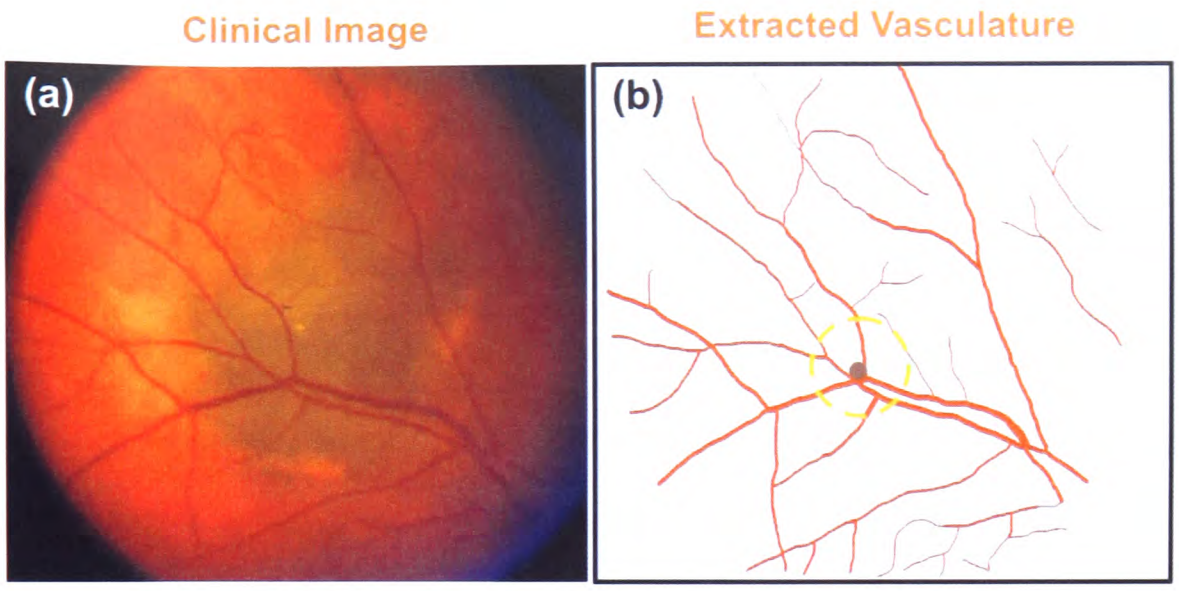

Figure 6.4: Growth pattern comparison of model vs. real. (a) is a fundus photo of the eye, clearly showing a tumour growth (image courtesy of Dr. Mark Rondeau of Cornell Medical School). (b) shows the vasculature extracted from the image in (a), and the brown dot within the dotted yellow circle represents the tumour seed for the model. (c) and (d) compare the real tumour growth outline with a sample growth of the model using the vasculature and tumour seed shown in (b). Reasons for difference are outlined in the text.

retina may influence the shape of the underlying tumour as they are "structural elements" that may limit local expansion of retina by the underlying tumour. In addition, part of the visible tumour growth (for example, the seeming growth along the vessels) may well be an artifact due to uneven illumination. Nevertheless, for illustration purposes it is assumed that the vasculature feeding the tumour directly and the vasculature depicted are approximately similar. Furthermore, a good idea of how the real and model parameter spaces relate is not yet known. The model in its current implementation does not include angiogenesis, nor is (are) the exact location(s) of the original cancer seed(s) in the real image known.

We proceeded to compare the model growth curves to data gathered from tumour–bearing nude mice with A2780 cell lines by Simeoni *et al.* [17]. The fit is shown in Fig. 6.3(c), where a basic rescaling of axes demonstrates a remarkable fit of the model growth curves to real growth data. For the model parameter values, it was assumed that α and β remained constant for the various curves, since all experiments were performed in controlled nude mice using the same cell lines. Instead, the differences in growth curves are due to differing $r^{i,n=0}$ values. In other words, despite the tissue composition of the nude mice and the cancer cell proliferation rate (i.e., β) being almost constant for all data curves, the model curves suggest that the vasculature and the nutrient supply rate (i.e., $r^{i,n=0}$) may not have been.

6.4 Predicted tumour re–growth following different treatment types

Having established the accurate growth behaviour of the model we explore simplified virtual treatment methods, and the resulting re–growth behaviour of the tumour. Different treatment methods result in distinct re–growth behaviour. The first method simulates the random removal of cancer cells only, instead of affecting all types of

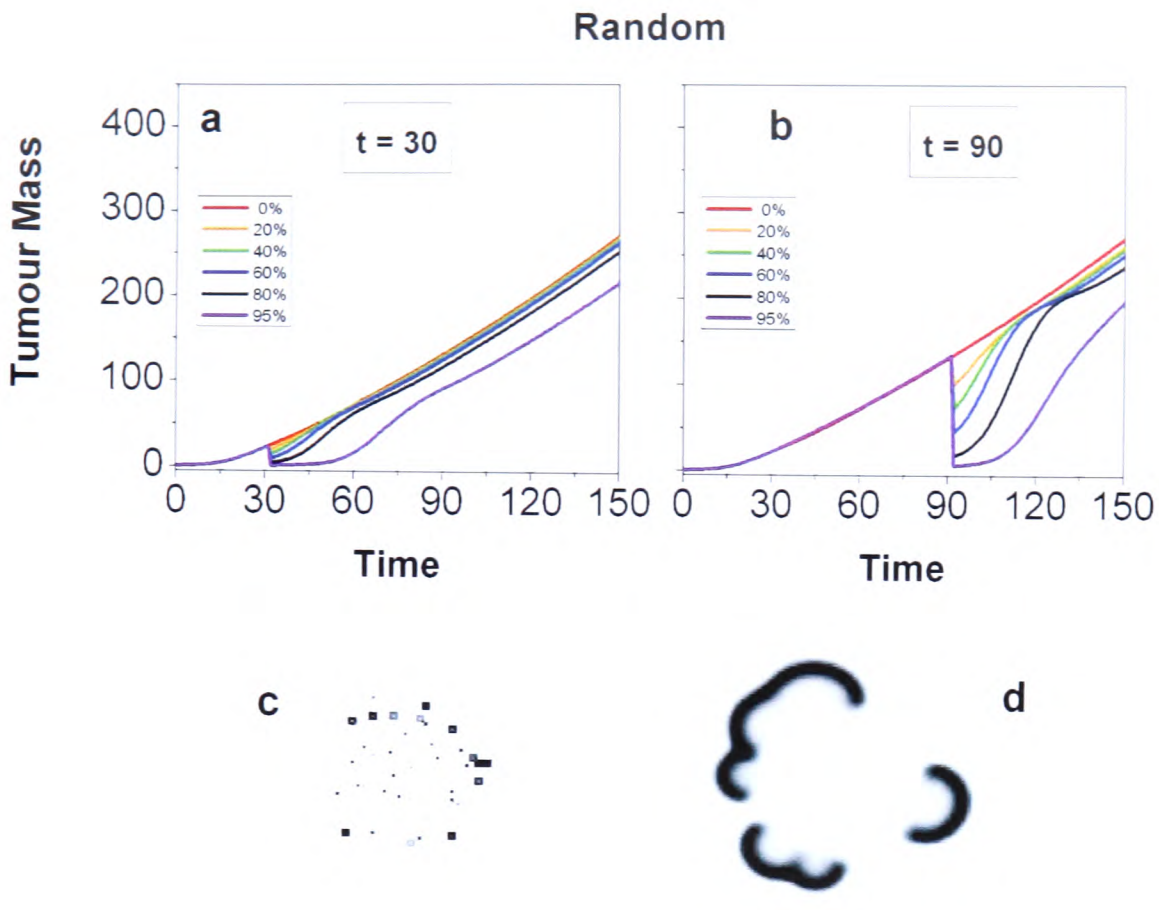

Figure 6.5: Treatment results. Cancer cells were targeted and removed by (a) randomly removing a certain percentage after $t = 30$ and (b) $t = 90$ time steps. The lines were averaged over 20 realizations. All lines show persistent re-growth which is more aggressive the higher the percentage removed. However, particularly for the high percentage lines, the re-growth pattern of the cancer can be very distinct. In some cases (c) cancer dies. In other cases (d) small clusters large enough in size survive to allow for aggressive re–growth, originating from multiple regions.

cells typical for chemotherapy. If the system is fully vascularized, it would allow engineered liposomes, for example, to reach all parts of the cancer, penetrating cancer cells exclusively, and subsequently being exploded by radio signal. Depending on the dosage administered, this results in a certain percentage of the cancer being attacked and removed randomly. A homogeneously vascularized environment was used, but the removal could be weighted towards vessel density in case of a heterogeneous vasculature. The growth curves highlight the persistence of cancer re–growth regardless of dosage and time of treatment (Fig. 6.5(a) and 6.5(b)). The curves are averaged over 20 realizations, due to the random nature of the removal. For high percentage removal in particular, individual realizations can lead to unsuspected re–growth patterns. Some cancers stop growing, as shown in Fig. 6.5(c). Yet, the majority of cases exhibit some re–growth of the tumour, because the random removal leaves behind small cancer clusters big enough to survive, allowing for aggressive re–growth. Interestingly, this can result in one, or often, more islands of re-growth, as illustrated in Fig. 6.5(d). Even in this homogeneous environment it is the small heterogeneties that lead to significant and highly non–trivial re–growth behaviour, emphasizing the importance of the nutrient supply, and in particular the interplay between vasculature structure and cancer growth.

The second technique resembles a one–off treatment where cancer is removed systematically in layers. In advanced tumours the vasculature is concentrated around the proliferating ring, with an almost completely empty core [18]. Hence, an immune response, or any chemical delivered through the vasculature, would amount to a bombardment from the outside in, resulting in a breakdown of the cancer in layers. The results show that if enough layers are removed at an early stage the cancer stops growing, as shown by the purple line Fig. 6.5(e). This is to be expected

since the proliferating ring is removed and an unpopulated necrotic core remains. More interestingly, further to the re–growth behaviour similar to random removal, a systematic attack shows a short period of continued tumour regression immediately after the treatment (see Figs. 6.5(e) and 6.5(f)). Although this has not been observed experimentally, we suspect verification, if measurements of growth rates are taken immediately after treatment. Similar to the random removal, continued regression was observed regardless of the advanced stage of tumour growth prior to treatment.

Such diverse behaviour poses questions of multiple treatments in two ways. First, a single second treatment of varying dosage; and second, multiple low dose follow up treatments in regular intervals. A single second treatment showed progressively more aggressive re–growth rates with increasing dosage (see Fig. 6.6(a)), emphasizing the importance of correct dosage, whilst finding the right balance to minimize catastrophic side–effects. On the other hand, the time between the first and second treatment had no significant affect on re–growth rates, as shown in Fig. 6.6(b). In order to avoid the aggressive behaviour of Fig. 6.6(a), multiple small dose treatments in regular intervals were explored, as shown in Fig. 6.6(c). This led to the interesting result that growth could be controlled, and the cancer kept at a constant size or perhaps slowed down significantly, depending on the time interval between treatments and the dose of each treatment. Keeping the tumour at a finite size is however risky and dependent on the lethality of the tumour type. Hence, for an advanced mutated cancer, it would be advisable to try and remove a significant portion of the cancer.

6.5 Summary

We have presented a simple model which demonstrates the importance of heterogeneity in cancer growth behaviour, whilst emphasizing the necessity that models

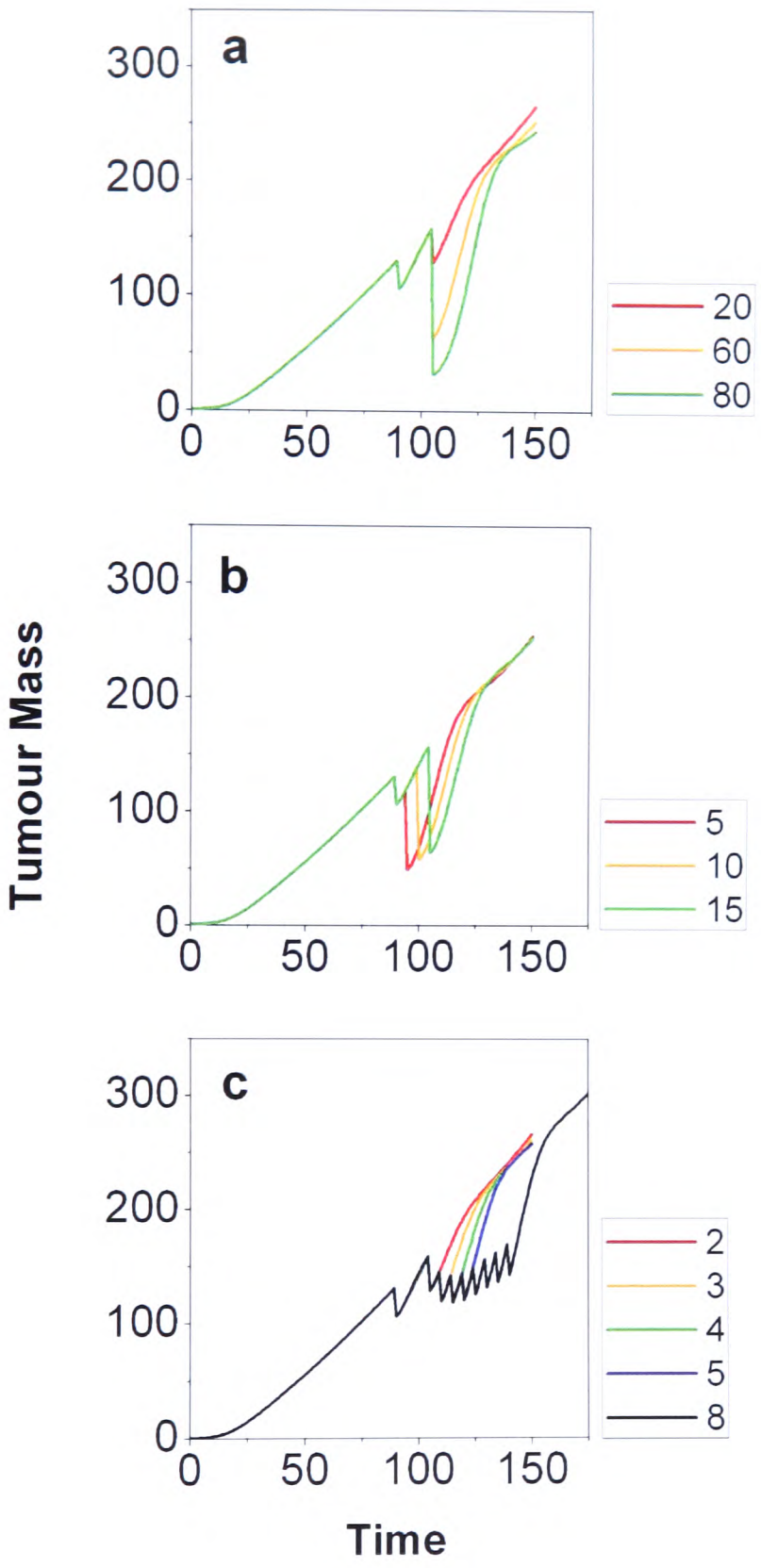

Figure 6.6: Multiple treatment results. A single treatment can be very aggressive and hence risky. We explored multiple treatments where (a) an initial removal of 20% was followed by a second treatment removing an additional percentage. Increasing the dosage of the second treatment resulted in an increased re–growth rate. (b) The time between treatments, provided the interval is not excessively long, had no impact on the re–growth rate. (c) Treated the cancer with multiple treatments at regular intervals each removing 20% of the tumour. It was possible to keep the cancer at an almost constant size.

be seeded with real images, thereby providing patient–dependent initial conditions. Such heterogeneity arises from the nutrient distribution caused by the underlying vasculature structure, a network which is dynamically evolving as a result of the intricate interplay with the growing tumour. Although the model itself is simplistic, and angiogenesis has not explicitly been explored, it could easily be (e.g. by setting α in Eqn. 6.2 to be negative). Most importantly, our model and its results raise interesting questions regarding possible modes of treatment – and more significantly, the effects of dosage and/or surgery on subsequent tumour re–growth.

Bibliography

[1] Greenman, C., et al. Patterns of somatic mutation in human cancer genomes. *Nature* **446**, pp. 153–158 (2007).

[2] Sjöblom, T., *et al.* The consensus coding sequences of human breast and colorectal cancers. *Science* **314**, pp. 268–274 (2006).

[3] Irish, J.M., Kotecha, N., Nolan, G.P. Mapping normal and cancer cell signalling networks: towards single-cell proteomics. *Nature Rev. Cancer* **6**, pp. 146–155 (2006).

[4] Sutherland, R.M. Importance of critical metabolites and cellular interactions in the biology of microregions of tumors. *Cancer* **58**, pp. 1668–1680 (1986).

[5] Postovit, L.-M., Seftor, E.A., Seftor, R.E.B., Hendrix, M.J.C. Influence of the microenvironment on melanoma cell fate determination and phenotype. *Cancer Res.* **66**, pp. 7833–7836 (2006).

[6] Eskey, C.J., Koretsky, A.P., Domach, M.M., Jain, R.K. Role of oxygen vs. glucose in energy metabolism in a mammary carcinoma perfused *ex vivo*: Direct measurement by 31P NMR. *Proc. Natl. Acad. Sci. USA* **90**, pp. 2646–2650 (1993).

[7] Gatenby, R.A., Maini, P.K. Cancer summed up. *Nature* **421**, p. 321 (2003).

[8] Deutsch, A., Dormann, S. Modelling of avascular tumour growth with a hybrid cellular automaton. *In Silico Biology* **2**, pp. 1–14 (2002).

[9] Scalerandi, M., Romano, A., Pescarmona, G.P., Delsanto, P.P., Condat, C.A. Nutrient competition as a determinant for cancer growth. *Phys. Rev. E.* **59**, pp. 2206–2217 (1999).

[10] Sherratt, J.A., Chaplain, M.A.J. A new mathematical model for vascular tumour growth. *J. Math. Biol.* **43**, pp. 291–312 (2001).

[11] Gatenby, R.A., Gawlinski, E.T. A reaction-diffusion model of cancer invasion. *Cancer Res.* **56**, pp. 5745–5753 (1996).

[12] Alarcón, T., Byrne, H.M., Maini, P.K. A cellular automaton model for tumour growth in inhomogeneous environment. *J. Theor. Biol.* **225**, pp. 257–274 (2003).

[13] Brú, A., Albertos, S., Subiza, J.L., García-Asenjo, J.L., Brú, I. The universal dynamics of tumor growth. *Biophysical Journal* **85**, pp. 2948–2961 (2003).

[14] Laird, A. K. Dynamics of tumor growth. *Br. J. Cancer* **18**, pp. 490–502 (1964).

[15] Steel, G.G. Growth kinetics of tumors. *Clarendon Press*, Oxford (1977).

[16] Brunton, G.F., Wheldon, T.E. Prediction of the complete growth pattern of human multiple myeloma from restricted initial measurements. *Cell Tissue Kinet.* **10**, pp. 591–594 (1977)

[17] Simeoni, M., *et al.* Predictive pharmacokinetic-pharmacodynamic modelling of tumor growth kinetics in xenograft models after administration of anticancer agents. *Cancer Res.* **64**, pp. 1094–1101 (2004).

[18] Holash, J., et al. Vessel cooption, regression, and growth in tumours mediated by angiopoietins and VEGF. *Science* **284**, pp. 1994–1998 (1999).

[19] Deisboeck, T.S., Berens, M.E., Kansal, A.R., Torquato, S., Stemmer-Rachamimov, A.O., Chiocca, E.A. Pattern of self-organization in tumour systems: complex growth dynamics in a novel brain tumour spheroid model. *Cell Prolif.* **34**, pp. 115–134 (2001).

[20] Anderson, A.R.A, Weaver, A.M., Cummings, P.T., Quaranta, V. Tumor morphology and phenotypic evolution driven by selective pressure from the microenvironment. *Cell* **127**, pp. 905–915 (2006).

Chapter 7

Conclusion

The theoretical research presented in this thesis has made several new contributions to the topic of complex systems. These are summarized below.

In the first part of the thesis, I investigated a multi-agent model which was designed to mimic real-world complex systems. I showed that by accounting for the strong intrinsic correlations between agents' strategies, one can accurately and analytically describe the systems dynamics. I then introduced an additional local communication (i.e. interaction) network between agents, thereby allowing them to intentionally share information. This emphasizes the functional properties of networks, as opposed to concentrating on the structural properties as is typical in the network literature. The resulting system exhibited highly non-ergodic dynamics. Next, I allowed the information exchanged between agents to be corrupted with some given probability, and found that the behaviour of just a handful of agents was enough to drive the system into a new phase – and consequently that the system exhibited a novel phase transition. In both cases, I successfully offered a quantitative analytic description of the system's fluctuations using a *Crowd–Anticrowd* formalism which was generalized to account for higher–order correlations.

The second part of the thesis turned its attention to cancer, which represents an ideal candidate network–based complex system. In particular, I introduced a

discrete, multi-scale model with particular emphasis on vasculature. The key element of this model was the dynamic interplay between the behaviour of the tumour (i.e. agents) and the vascular adaptation, again focussing on the functional properties of the network. For the purpose of comparison to empirical data and subsequent analysis, this model was designed to be far simpler than those discussed in Part I – however, I have shown that it can reproduce known clinical data with remarkable accuracy. This model takes a coarse-grained approach in order to allow for easy scalability, with the eventual goal of using real clinical images of varying resolution as the initial seed. I also showed that it predicts unexpected re-growth behaviour of the tumour in response to a range of realistic treatment scenarios.

Finally, I conclude by briefly presenting a number of avenues along which the research contained within this thesis may be extended:

- ◇ Study the effects of different network structure, such as scale–free or small world, on the population dynamics played within the *B–A–R* system. This would allow the model results to be compared to real–world systems known to possess different network structures.

- ◇ Extension and generalization of the *Crowd–Anticrowd* theory developed in chapters 2–4 to non–binary systems. This would allow a broader range of complex systems to be studied, and potentially provide a solid basis for analytical and numerical research on the interplay between functional networks and the underlying population of interacting objects.

- ◇ Application of the *Crowd–Anticrowd* theory to real–world complex systems across a wide range of disciplines. Such application would allow comparison

to real data of a system of interest, and possibly lead to a better understanding of the system in terms of prediction and control.

Part 2

Carry out in–depth investigations extending the cancer model introduced in chapter 6 to include:

- ◇ Angiogenesis and the resulting vascular structure evolution. There is an intricate interplay between the growing tumour and the vasculature which feeds it. The vasculature structure heavily influences the tumour growth behaviour, which in turn changes the vascular structure by means of vessel degradation, vessel cooption, vasculogenic mimicry and angiogenesis. Hence this is a highly feedback sensitive and dynamic system, and hence such understanding could help determine the future behaviour.

- ◇ Continue to study the effects of different perturbations or treatments on the tumour, for possible alternative ways of controlling or steering its behaviour. In particular, an investigation into how vascular structural changes might lead to novel approaches.

- ◇ Study growth of cancer on different simple motifs. If we know the properties of cancer growth on different shapes such as a y–junction, line, circle, or square, it might be possible to piece together the complete vasculature and say something about the tumour growth behaviour. Vice versa, by looking at the shape of the tumour, it might be possible to determine the likely vasculature hidden within the tumour.

- ◇ Work closely with clinicians to test our findings and further advance the model.

The access to real patient data, in addition to laboratory experiments is invaluable to a steady advancement and understanding of cancer research. We believe we have a good set–up to combine experimental data with the model.